LA-UR-24-33027

Approved for public release; distribution is unlimited.

Title:	Cloud Fusion of Big Data and Multi-Physics Models using Machine Learning for Discovery, Exploration, and Development of Hidden Geothermal Resources
Author(s):	Frash, Luke Philip Ahmmed, Bulbul Mudunuru, Maruti K Tartakovsky, Daniel
Intended for:	Report
Issued:	2024-12-09

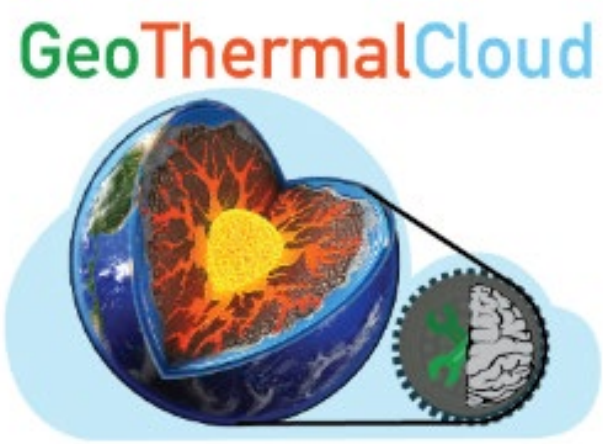

Cloud Fusion of Big Data and Multi-Physics Models using Machine Learning for Discovery, Exploration, and Development of Hidden Geothermal Resources

FOA Number:	1956-1516
FOA Title:	Machine Learning for Geothermal Energy
Award Number:	DE-EE3.1.8.1 (LANL) and 1.4.1.9 (PNNL)
Recipient:	Los Alamos National Laboratory (LANL)
PI:	Luke Frash (LANL)
Institutions:	Los Alamos National Laboratory (LANL), Pacific Northwest National Laboratory (PNNL), Stanford University (Stanford), Google Inc (Google), Chevron (Chevron), and Julia Computing (Julia)
Participants:	Bulbul Ahmmed (LANL), Maruti Mudunuru (PNNL), Velimir Vesselinov (LANL), Satish Karra (LANL), Wu Hao (LANL), Chadwick Holmes (Chevron), Spencer Manley (Chevron), Yan Pan (Chevron), Viral Shah (Julia), Mark Mims (Google), Kevin Jameson (Google), Steven Boesel (Google), Dustin Sell (Google), Daniel Tartakovsky (Stanford), Dimitrios Belivanis (Stanford), Zitong Zhou (Stanford)

Table of Contents

Executive Summary

The primary goals of this project are identifying hidden geothermal resources in the USA and designing profitable enhanced geothermal systems (EGS). Many non-obvious processes and parameters could characterize geothermal resources and could control the ultimate energy potential of geothermal fields. Diverse datasets (e.g., geology, geochemistry, geophysics, satellite, airborne geophysics) are available to help characterize geothermal resources, but this data is sparse and multi-scale. This has hindered attempts to leverage the datasets for geothermal exploration and profitable EGS design. Recent advancements in machine learning (ML) give promise to overcome these issues. Modern ML methods and tools can (1) analyze large datasets, (2) assimilate model ensembles that include a multitude of inputs and outputs, (3) process sparse datasets, (4) perform transfer learning between sites with different data quality, (5) extract hidden geothermal signatures from field and simulation data, (6) label geothermal resources and processes, (7) identify high-value data acquisition targets, and (8) guide geothermal exploration and production by selecting optimal exploration, production, and drilling strategies.

In this work, we implement ML-based geothermal exploration and an enhanced geothermal systems (EGS) design tool to achieve the above goals. Our exploration tool is GeoThermalCloud (GTC) EGS design tool is GeoDT-ML. GTC (github.com/SmartTensors/GeoThermalCloud.jl) utilizes a LANL unsupervised ML platform called SmartTensors (https://tensors.lanl.gov/) to automate data analyses and interpretations by extracting hidden signatures to identify geothermal prospects. It enables the identification of critical measurements needed to identify geothermal resource signatures. GeoDT-ML (github.com/SmartTensors/GeoThermalCloud.jl/tree/master/) adds coupling to GeoDT (https://github.com/GeoDesignTool/GeoDT.git) for stochastic EGS design optimization and performance prediction. GeoDT-ML leverages recent advances in deep learning and high-performance computing. Contributors to this effort include LANL, PNNL, Google, Stanford, and Julia Computing.

To test our new tools, we analyzed eight datasets from USA using GTC to identify prospective geothermal resources. The first data set includes 44 locations in southwest New Mexico and 18 geological, hydrogeological, geophysical, geothermal, and geochemical attributes. We defined low- and medium-temperature hydrothermal systems and discovered a new highly prospective site. The second data set analyzed 18 shallow water chemistry attributes at 14,342 locations in the Great Basin. It demarcated modestly, moderately, and highly prospective sites including key attributes for each type of prospectivity. The third data set analyzed Utah FORGE data including satellite (InSAR), geophysical (gravity, seismic), geochemical, and geothermal attributes. This enabled prospectivity analysis to identify future drilling locations using geological, geochemical, and geophysical attributes. Maps of temperature at depth and heat flow are constructed based on the available data. Prospectivity maps were generated, and drilling locations were proposed for future geothermal field exploration. The fourth data set analyzed 21 attributes at 120 locations in Tularosa Basin, New Mexico; data comes from past play fairway analyses in this region. ML analyses identified geothermal signatures associated with modestly, moderately, and highly prospective systems. We also defined dominant attributes and spatial distribution of the geothermal signatures. The fifth, sixth, seventh, and eighth datasets include Tohatchi Springs, New Mexico, Hawaii, Brady site, Nevada, and EGS Collab, respectively.

Moreover, we coupled GTC and magnetotellurics data to pinpoint drilling locations for developing geothermal projects in the Tularosa Basin, New Mexico. GTC found potential prospective locations for geothermal resources near White Sands Missile Range and McGregor Range at Fort Bliss. Magnetotellurics data determined the potential depth (~1800m) of geothermal prospects at McGregor Range based on apparent resistivity structures/layers in the subsurface. The McGregor Range consists of three resistivity layers and two resistivity structures. Magnetotellurics data also helps identify that the western portion of the McGregor Range has thick and low-resistivity earth materials. The low resistivity to the west is most likely from a fault system. The west-central part of the McGregor Range appears to hold the highest geothermal potential because of increased porosity and permeability attributed to faults.

Supporting this effort, we devised a coupling strategy between a process model and GTC to characterize hydrogeological conditions and geothermal conditions, respectively. The process model characterizes hydrogeological and geothermal conditions on highly prospective geothermal sites provided by GTC. We developed a physics-informed neural network (PINN) version of the Burns equation that can be easily coupled with GTC.

Furthermore, we performed a design optimization effort with the goal of maximizing the economic value of an EGS power plant. This study optimized flow rates and well spacing between injection and production wells using an estimated net present value in dollars (NPV). For this task, we used GeoDT to simulate Utah FORGE EGS development but with the consideration of drilling to deeper depths and drilling higher numbers of wells. This model includes natural fractures, stimulated fractures, long-term fluid circulation, heat production, power cycle analysis, and economics to combine drilling costs and power production into a common metric (i.e., NPV) as a unified and quantified target for optimization.

Next, we deployed our ML tools to estimate the permeability of geothermal reservoirs. Predicting permeability of geothermal reservoirs is a non-trivial task because of huge computational runtimes and a lack of measurements. To overcome these limitations, we used chemistry data and our convolutional neural network based ML model, based on a high-fidelity model. Next, we predicted permeability using Markov chain Monte Carlo simulation. We found that Markov chain Monte Carlo simulation predicts permeability with a high certainty if the prediction zone in the simulation area has chemical concentration data.

Finally, we analyzed the DOE funded INGENIOUS and GeoDAWN projects data. For discovering hidden geothermal systems in the Great Basin, the INGENIOUS project accumulated old data, collected new data, and released them in 2022. The dataset includes a total of 24 geological, geophysical, and geochemical attributes. Data resolution and scale significantly vary. We brought all data into the same resolution and scale by applying the inverse distance weighting interpolation technique for predicting data in unsampled locations. Subsequently, we analyzed LiDAR data of the GeoDAWN project. We received data in tiles format. The DOE's overarching goal is to use ML on LiDAR data for finding favorable geological structures (e.g., step up faults in Brady, Nevada). To serve this purpose, we need to label favorable geologic structures that correspond to LiDAR data. We developed an algorithm to label the LiDAR data with favorable geologic structures.

Overall, this project achieved its primary objectives of identifying prospective locations for geothermal energy exploration and development as well as design optimization of Enhanced Geothermal Systems (EGS). In the process, we developed data analysis and design tools that are now released open source for others to benefit from. These tools include GeoThermalCloud for unsupervised learning to discover hidden signatures of geothermal resources and GeoDT-ML for deep learning enabled EGS design optimization. Supporting this effort, is our physics-based ensemble technoeconomic assessment tool GeoDT that was used to predicting the performance of EGS in highly uncertain site conditions. Our work identifies new prospective locations for hidden geothermal resources in southern New Mexico, southern Nevada, and western Texas.

Chapter 1: GTC and GeoDT-ML and Their Usage

GTC

Introduction

The project is motivated by the challenges, risks, and costs associated with geothermal exploration and production[1]. Many processes and parameters impacting geothermal conditions are poorly understood. Diverse datasets are available to help characterize subsurface geothermal conditions (public and proprietary; satellite, airborne surveys, vegetation/water sampling, geological, geophysical, etc.). Yet, it is unclear how to properly leverage these datasets for geothermal exploration due to an incomplete understanding of how physical processes impacting subsurface geothermal conditions are represented in these observations. Recent advancements in machine learning (ML) promise to resolve these issues[1].

The tremendous challenges and risks of geothermal exploration and production bring the demand for novel ML methods and tools that can (1) analyze large field datasets, (2) assimilate model simulations (large inputs and outputs), (3) process sparse datasets, (4) perform transfer learning (between sites with different exploratory levels), (5) extract hidden geothermal signatures in the field and simulation data, (6) label geothermal resources and processes, (7) identify high-value data acquisition targets, and (8) guide geothermal exploration and production by selecting optimal exploration, production, and drilling strategies[2]. Our goals and work under Phases 1 and 2 (as proposed) of this project address all these needs.

Under Phase I&II, we have developed GTC and GeoDT-ML. GTC is an unsupervised ML-based tool to discover and extract new (unknown/hidden) geothermal signatures in existing site, synthetic, and regional datasets. Our ML analyses also identified high-value data acquisition strategies that can reduce geothermal exploration/production costs and risks. Moreover, GTC categorized geothermal data, which is applied to generate geothermal data labels (e.g., geothermal resource types). GTC allows for the treatment of both public and proprietary datasets. This is an essential feature considering the high sensitivities associated with using proprietary data. Moreover, the GTC framework includes a series of advanced pre-processing, post-processing, and visualization tools, which tremendously simplify its application for real-world problems. These tools make the ML results understandable and visible even for non-experts. Thus subject-matter expertise is not a critical requirement during the training phase of the GTC framework; however, their opinions are useful for verifying the outputs.

GeoDT-ML is an enhanced geothermal system (EGS) prospecting tool. It is an ML version of GeoDT[3–6]. GeoDT is a very fast modeling tool to run thousands of realization tweaking reservoir, drilling, and geothermal plant parameters. The main mechanism is to use GTC for geothermal resources exploration to find favorable geothermal locations and then use GeoDT-ML for exploring EGS prospectivity. Figs 1.1 and 1.2 demonstrate the schematics of GTC and GeoDT-ML, respectively.

We have used GTC on ten geothermal datasets. Eight datasets include site/real data, including a large and sparse dataset of the Great Basin, and two datasets are synthetic data. The analyses found critical information that could not be found using supervised ML or exploratory statistical analyses. Most of the data and analyses are available on GitHub as well. Obtained results can be reproduced and further expanded by adding additional data. Practitioners and researchers are welcome to utilize GTC to solve other geothermal problems. GeoDT-ML can be used to study FORGE EGS prospectivity.

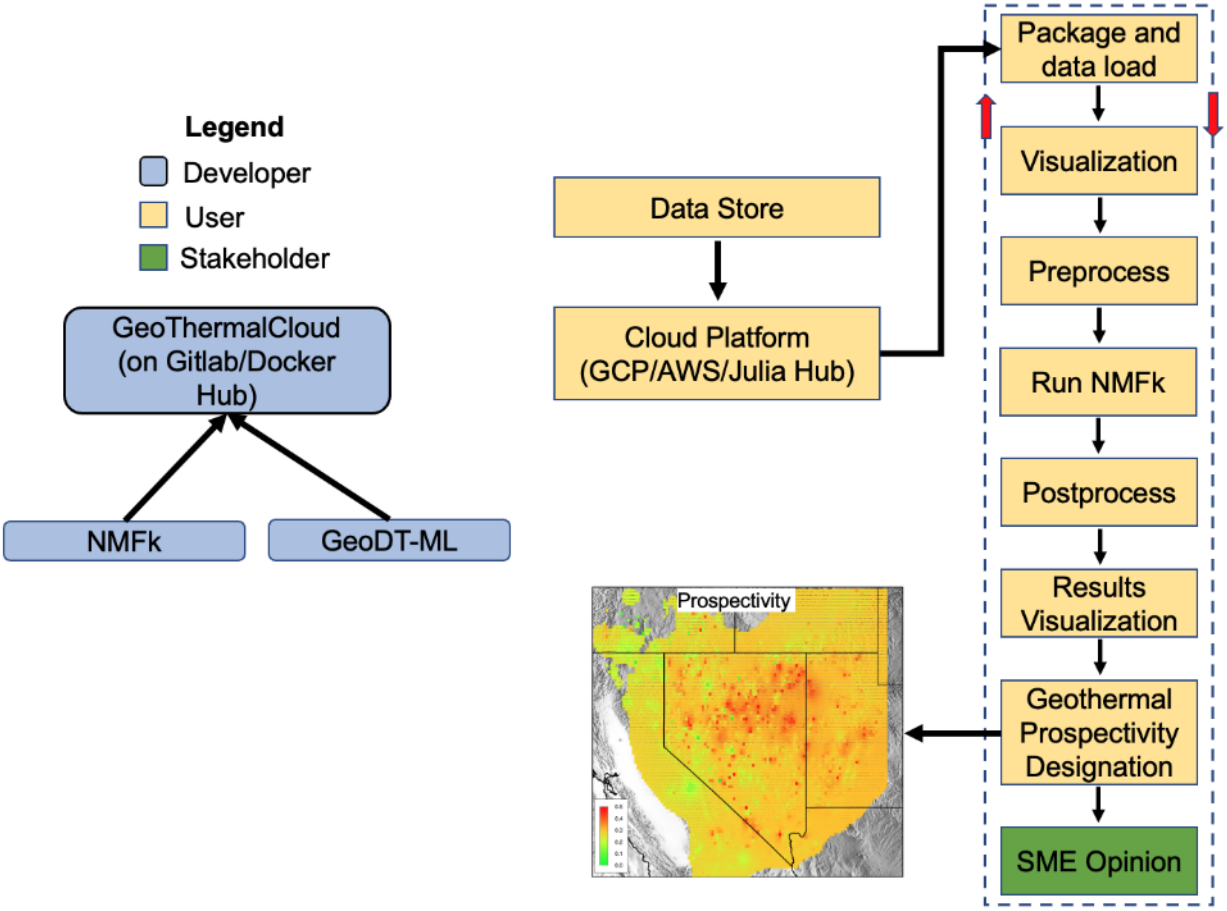

Fig. 1.1: Specific components of developers, users, and subject matter experts in the GTC platform.

Capabilities

GTC capabilities include (1) analyzing large field datasets, (2) assimilating model simulations (large inputs and outputs), (3) processing sparse datasets, (4) performing transfer learning (between sites with different exploratory levels), (5) extracting hidden geothermal signatures in the field and simulation data, (6) labeling geothermal resources and processes, (7) identifying high-value data acquisition targets, and (8) guiding geothermal exploration and production by selecting optimal exploration, production, and drilling strategies. The GTC is an open-source tool available at https://github.com/SmartTensors/GeoThermalCloud.jl (a part of our SmartTensors framework; http://tensors.lanl.gov, https://github.com/SmartTensors)[2] and its counterpart docker image is https://hub.docker.com/r/bulbulahmmed/geothermalcloud-v1.

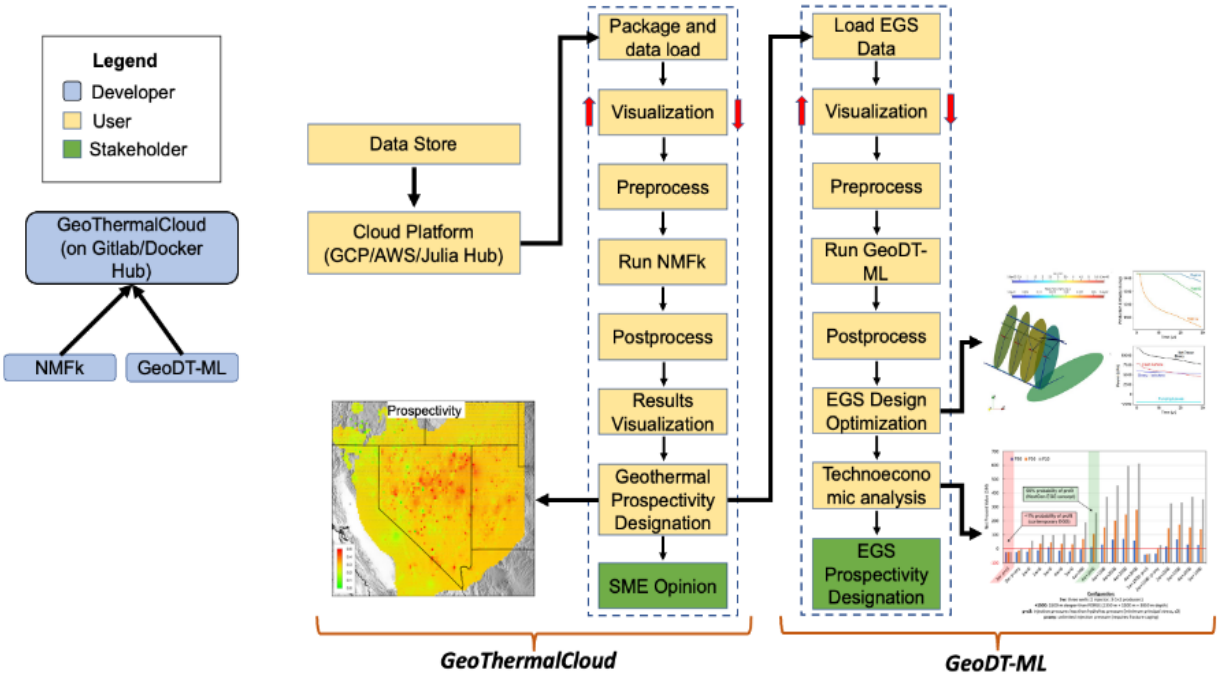

Fig. 1.2: Specific components of developers, users, and subject matter experts in the GTC and GeoDT-ML platforms.

Methods

ML methods, in general, can be subdivided into three categories: supervised, physics-informed, and unsupervised. The supervised methods require attributes and corresponding labels of the analyzed data[7]. The labeling should be done by subject-matter experts who can identify, for example, locations with high-, intermediate-, and low-temperature geothermal prospectivity or specific geologic features such as fault offsets. The supervised methods are then applied to learn geothermal prospectivity based on the available data. However, the successful training of supervised methods requires large, continuous (without data gaps), non-noisy (with small measurement errors) training datasets that are typically not available for geothermal exploration. In essence, the supervised methods cannot discover something that is not already known and provided as labels in the training dataset. The supervised methods are highly efficient in processing large datasets and finding out how the processed data can be categorized. For example, they can be trained to recognize images of cats and dogs; however, they will not recognize horses if they have not been trained already to identify them. Furthermore, the supervised ML methods are sensitive to noise in the analyzed data or the so-called "adversarial examples"[8] where small random noise, undetectable to the human eye, can fool the detection capabilities of these methods. All of these features make the application of supervised ML methods challenging for real-world science applications. Commonly used supervised methods include deep neural networks[6,9], convolutional neural networks[10], recurrent neural networks[11], and random forest[12].

Physics-informed ML (PIML) methods also learn from data like supervised methods. They also include preconceived science knowledge through equations and models representing physics laws, constitutive relationships, and processes. Physics information can be (1) directly embedded in the

ML framework[13] or (2) added as penalties in the ML loss minimization process[14]. However, the physics-informed neural networks (PINN) are problem specific and not general like the traditional supervised deep neural networks. Therefore, the construction PINN needs subject-matter expertise related to the analyzed problem. Still, PIML analyses have better efficiency, accuracy, and robustness compared to the traditional ML analyses. In contrast, the unsupervised ML techniques extract information from existing datasets without any prior labeling or subject-matter preprocessing. The unsupervised ML is applicable to discover unknown features and unmix mixed signals present in the processed data.

GTC utilizes our novel, open-source, LANL-developed, patented ML methods and computational tools. All these methods are distributed as SmartTensors. SmartTensors is a toolbox for unsupervised and physics-informed ML based on matrix/tensor factorization constrained by penalties enforcing robustness and interpretability (e.g., nonnegativity; physics and mathematical constraints; etc.). SmartTensors has already been successfully applied to analyze diverse datasets related to a wide range of problems, from COVID-19[15] to wildfires and text mining. Also, the SmartTensors framework can handle big data and has already been demonstrated to perform tens of TBs of data using DOE supercomputers.

The two most commonly used ML algorithms in SmartTensors are nonnegative matrix/tensor factorization methods coupled with customized k-means clustering (NMFk and NTFk). They perform nonnegative matrix/tensor factorization coupled with customized k-means clustering[1,16]. NMFk and NTFk are capable of identifying (i) the optimal number of hidden signatures in data, (ii) the dominant set of attributes in data that correspond to identified hidden signatures, and (iii) locations associated with each hidden signature.

All datasets are formed by directly observable quantities, while the underlying processes or data signatures usually remain unseen, hidden, or latent[16]. These hidden signatures (or features/signals) can be either impossible to measure directly or are simply unknown. For example, let us assume that a series of microphones are placed in a noisy ballroom where many people are talking. The collected data records the mixtures of voices, sounds, and noises. The latent signatures are the individual voices that cannot be recorded separately but can be extracted from the collected data. Extracting latent signatures reduces the dimensionality of the data and defines low-dimensional subspaces[17] that represent the entire dataset. After the extraction, the obtained information is post-processed by subject-matter experts to identify the physical meaning or the origin of the extracted signatures.

Similarly, our unsupervised ML techniques have been applied here to extract latent signatures and hidden (mixed) physical processes embedded in large, diverse geothermal datasets. Hidden (latent) signatures provide a low-dimensional and compressed representation of the processed dataset. They can also be viewed as basis vectors providing optimal data projection. In the case of geothermal applications, these signatures typically represent information about a series of physical processes that occur in observable and/or simulated datasets. These signatures can be multi-dimensional capturing processes occurring in spatiotemporal space and captured by a set of diverse attributes. Geothermal attributes we have processed in this report include temperature, gradients, geothermometers, conductivity, permeability, fluxes, fracture densities, in-situ stresses, etc.

To discover hidden signatures and their optimal number in large geothermal datasets, NMFk and NTFk are at the forefront among various unsupervised ML methods such as nonnegative matrix factorization (NMF)[17], principal component analysis (PCA)[18], independent component analysis (ICA)[19], singular value decomposition (SVD)[20], nonnegative tensor factorization (NTF)[21], and Gaussian process/mixture modeling[22]. In contrast, with traditional NMF[17], NMFk allows for automatic identification of the optimal number of signatures (features) present in the data[1,2,23]. The nonnegativity constraint makes the decomposed matrices easier to interpret than PCA, SVD, and ICA because the extracted signatures are additive. Moreover, NMFk and NTFk can handle huge (TBs), real, categorical, and missing data. Dealing with missing data is challenging or impossible for other supervised and unsupervised ML methods. Even more importantly, the missing data (some or all of it) can be reconstructed from available data using the obtained NMFk and NTFk results. Our ML methods also provide estimates of uncertainties associated with the estimated missing data. All of these features of our ML methods make them very suitable for geothermal ML analyses.

Detailed descriptions of our novel NMFk and NTFk algorithms are provided in our papers[1,16]. Here, we give just a high-level description of the NMFk and NTFk methodologies to support the discussion of geothermal analyses in this report. NMFk performs matrix factorization of a data matrix, $X_{m\times n}$, where the m rows represent measurement locations, and the n columns are the values of the geothermal attributes. The goal of NMFk is to find the optimal number of signatures k that describe the analyzed dataset. This is accomplished by matrix factorization, which can be represented as using:

$$X \cong W \times H \tag{1.1}$$

where $W_{m\times k}$ is an "attribute" matrix characterizing the significance of attributes and $H_{k\times n}$ a "location" matrix captures the importance of locations and their spatial association. It is important to note that all the elements of matrices W and H are unknown. The number of signatures k is also unknown. The matrix factorization in (1) provides an approximate representation of the data X. To solve for all the unknowns, NMFk performs a series of matrix factorization with random initial guesses for W and H elements and for a range of values of k; theoretically, k can range between 2 and min(m,n). For a given number of signatures k, Equation 1 is solved iteratively by minimizing the reconstruction error $O(k)$:

$$(k) = || X - W \times H||_F \tag{1.2}$$

by constraining the W and H elements to be greater or equal to zero (nonnegative), and F defines the Frobenius norm[24]. Under the NMFk algorithm, NMF is executed numerous times (typically 1,000), which generates a series of solutions for W and H matrices for a given k value. The resulting multiple H solutions are clustered into k clusters using a customized k-means clustering[1,16]. The average silhouette width $S(k)$ based on cosine norm is computed for all k clusters. This metric measures how well the random NMF solutions are clustered for a given value of k. The values of $S(k)$ theoretically can vary from -1 to 1.

These operations are repeated for a series of k values. The optimal number of signatures, k, is estimated on how the reconstruction error$O(k)$ and the average silhouette width $S(k)$ vary with the increase of k. The reconstruction error decreases as k increases. The average silhouette width behavior is more complicated; $S(k)$generally declines as k increases from 1 to -1. However, $S(k)$ values frequently spike up for specific k values, indicating that these k values are potentially optimal. In an ideal case, a given k value is considered optimal when adding another signature does not significantly improve the reconstruction of X (i.e., lower $O(k)$) and does not lower $S(k)$. In practice, a solution with $S(k)$ greater than 0.5 and the lowest $O(k)$ value can be chosen as an optimal solution. The solutions with k values less than the optimal value and S(k) values > 0.5 are acceptable; they provide underfitting representations of the data matrix X. All the solutions with k values greater than the optimal value are not acceptable; they provide overfitting representations of the data matrix X.

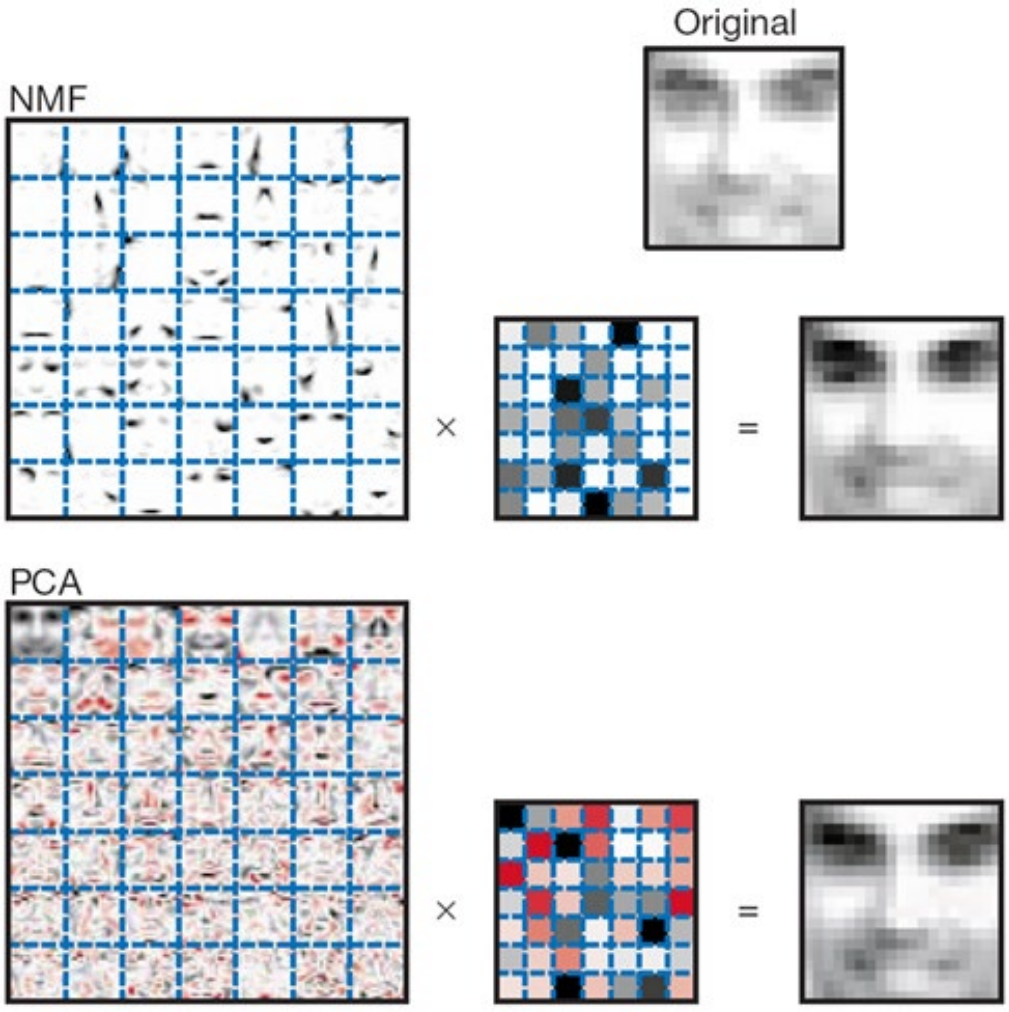

Fig. 1.3: ML of faces using NMF and PCA. Nonnegativity constraint provides additive, sparse and interpretable results where facial features such as eyes and noses are well defined[17].

We listed the benefits of NMFk over similar unsupervised ML tools above. PCA is the closest similar tool to NMFk. PCA factorizes the data matrix X into score (S) and principal component (P) matrices. The factorization can be represented as:

$$X \cong SP \tag{1.3}$$

S is a diagonal matrix. As in NMF, Equation 3 is solved iteratively by minimizing the following function

$$L = \left|\left|X - SP\right|\right|_F \tag{1.4}$$

PCA searches for linear combinations in the data by projecting each data point onto an optimal set of principal components (PCs) to obtain a low-dimensional representation of data while preserving maximum data variation. PCs are ordered by the magnitude of data variance as captured by the S diagonal elements.

Even though NMF and PCA are mathematically similar, the ML results obtained by both methods are very different. For instance, both NMF and PCA can reconstruct human faces very well (Fig. 1.3). Both methods extracted 49 basic facial features (can also be called dictionaries, basis vectors, or eigenvectors; the matrices on the left) needed to reconstruct the entire training set of ~1,000 faces (i.e., both methods performed data dimensionality reduction from ~1,000 to 49). However, the nonnegativity constraints provide additive, sparse, and interpretable results where facial features such as eyes and noses are well defined (Fig. 1.3; W matrix; top left). NMF face reconstruction is obtained by adding a series of dominant features shown as black squares in the H matrix. In contrast, the interpretation of PCA results is challenging. The first face (upper left corner of matrix P) is the average face of the training set, and the reconstruction of face X is obtained by adding and subtracting a series of facies features (in P) based on the weights (in S; red defines negative values or feature subtraction; black represents positive values or feature addition).

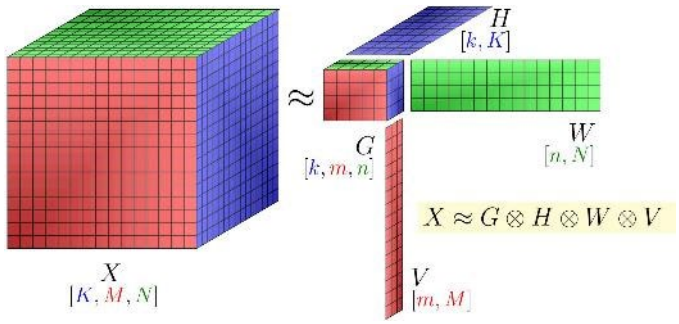

Fig. 1.4: Example factorization of a data tensor X into a smaller core tensor G and three matrix factors for each dimension. Matrix factors represent signatures in different dimensions. G defines how these signatures are mixed.

In addition to matrices, our ML methods can process multi-dimensional datasets, i.e., tensors. Most of the geothermal data are multi-dimensional. The data indices can be space coordinates and time for each spatiotemporal location, and there might be numerous observables coming from different data sources (streams). Similarly, geothermal model outputs are multi-dimensional. There is a limited number of ML methods that can process multi-dimensional datasets, and our novel nonnegative tensor factorization method coupled with k-means clustering (NTFk) is at the forefront. The factorization process converts a data tensor (labeled as *X* in Fig. 1.4) into a smaller core tensor (labeled as *G* in Fig. 1.4) and three matrix factors for each dimension (labeled as *H*, *W*, and *V* in Fig. 1.4). Matrix factors represent signatures in different dimensions. In the example presented in Fig. 1.4, *H*, *W* and *V* contain 5, 4, and 3 signatures, respectively. *G* defines how these signatures occurring in different dimensions are mixed to reproduce the original data tensor. The tensor factorization is again achieved through solving a minimization problem and the estimation of the optimal number of signatures in each dimension is performed using customized *k*-means clustering[21,25].

We performed IDW interpolation to determine attributes at unknown locations using highly variable data. IDW is efficient, intuitive, and provides relatively accurate data for a large number of points. The output value of an unknown location is attributed to the sample points located near it. Sample points, within a specified radius, have a greater "weight" associated with them making points that are closer to one another are more alike than those that are far apart[26,27]. Since the weights of the sample points are proportional to the inverse of the distance raised to a power value *p*, as the distance from an unknown point increases, the weight decreases quickly[26,27]. The formula of IDW is given by:

$$z_p = \frac{\Sigma_{i=1}^{n}\left(\frac{z_i}{d_i^p}\right)}{\Sigma_{i=1}^{n}\left(\frac{1}{d_i^p}\right)} \tag{1.5}$$

where z_p is the value of the unknown point, z_i is the value of the known point, d_i^p is the distance to the known point, and n is a fixed number of closest points.

MT is a passive geophysical technique used for measuring electrical resistivity structures in the subsurface[28–31]. Solar winds and lightning from thunderstorms cause natural variations in the earth's magnetic field that penetrate the subsurface and induce an electrical current[29]. The electromagnetic fields (EM) from an MT survey are recorded at frequencies generally ranging from 0.001 kHz to 10 kHz[32]. The low-frequency response (<1 Hz) originates from solar winds, and the high-frequency response originates from worldwide lightning strikes[29,32].

In MT data, a time series of the two components of the electric field (E_x and E_y) and three components of the magnetic field (H_x, H_y, and H_z) are measured on the earth's surface (Fig. 1.5). The ratio between the electric and magnetic field components (E/H) is called the impedance tensor

(*Z*). As a proportion of the electric and magnetic fields are used to compute the impedance tensor. The impedance tensor, *Z*, is used to determine the apparent resistivity and phase[29,32]. The following equations use the components of *Z* to calculate apparent resistivity and phase. Both apparent resistivity and phase are commonly plotted as a function of frequency for MT data analysis to decipher subsurface structures.

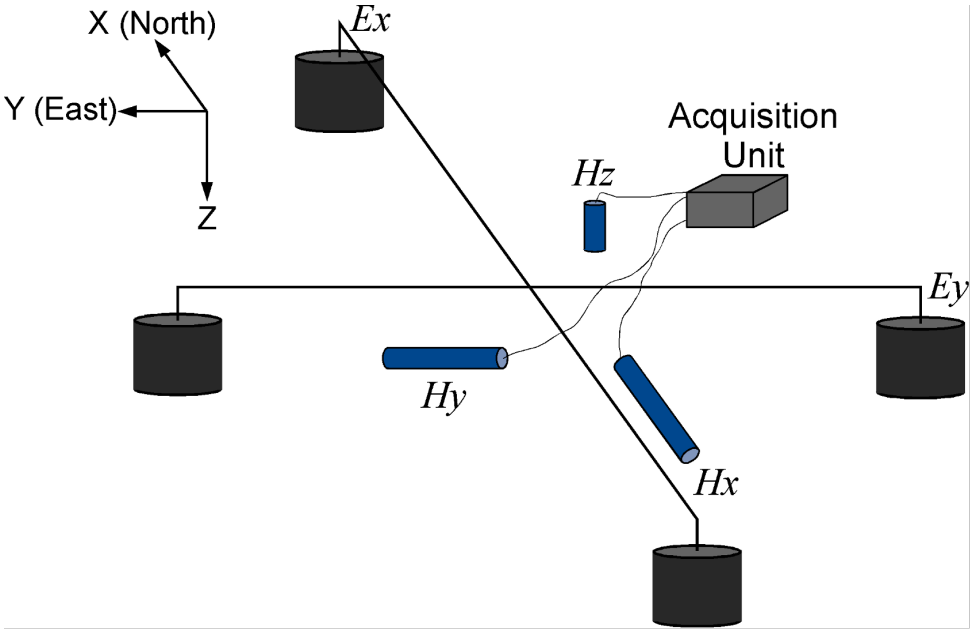

Fig. 1.5: Schematic of the arrangement and setup of electrodes and coils in the field during MT data acquisition[33].

While NMFk is effective for defining potential geothermal resources and identifying their spatial location, for small site data, regional geothermal and hydrogeologic estimates are required for developing geothermal fields. Regional conditions dictate the sustainability of geothermal fields. For instance, information on the advective heat flow will provide insight into the sustainability of the heat source to the aquifer. To capture regional hydrogeological and geothermal conditions, Burns, et al., 2015 formulated a 1D analytical solution, which evaluates geothermal and hydrogeologic controls on regional groundwater temperature distribution $T(s)$[34].

$$T(s) = [T_{LS}^{0} + \Delta T_{geothermal} + \Delta T_{viscous}] + [T_{0} - T_{LS}^{0} - \Delta T_{geothermal} - \Delta T_{viscous}]e^{f_{0}s} \quad (1.6)$$

where $T(s)$ is temperature at space s, T_{LS}^{0} is temperature at land surface at $s = 0$, T_0 is the temperature at $s = 0$ where groundwater flows into domain, $\Delta T_{geothermal}$ is the change in temperature across the vadose zone required to conduct the heat flow entering the aquifer at the basement, $\Delta T_{viscous}$ is the change in temperature across the vadose zone to conduct the viscous heat generated, and $f_0$is a function of aquifer width and volumetric flux.

Input parameters in Burns equation include land surface temperature, groundwater flux, hydraulic head, vadose thermal conductivity, depth to water, and basal heat flux. The outputs include aquifer temperature, viscous heat flux, vadose heat flux, and advective heat flux that assist in quantifying

components of heat flux that contribute to aquifer temperature. GTC includes both analytical solutions and equivalent neural network-based ML models.

Besides reconstruction error and silhouette width, we also used R^2 to determine the accuracy of prediction.

$$R^2 = 1 - \frac{\sum_{i=1}^{n}(\hat{y}_i - y_i)^2}{\sum_{i=1}^{n}\left(y_i - \underline{y}_i\right)^2} \tag{1.7}$$

where n, y_i, $\hat{y}_i$, and $\underline{y}_i$ represent the number of data points, actual data, predicted data, and mean of data, respectively.

Case Studies

ML methods embedded in the GTC have been extensively tested and validated against various datasets (Fig. 1.6)[2,35]. Outputs of these applications have been published in presentations, conference papers, and peer-reviewed papers.

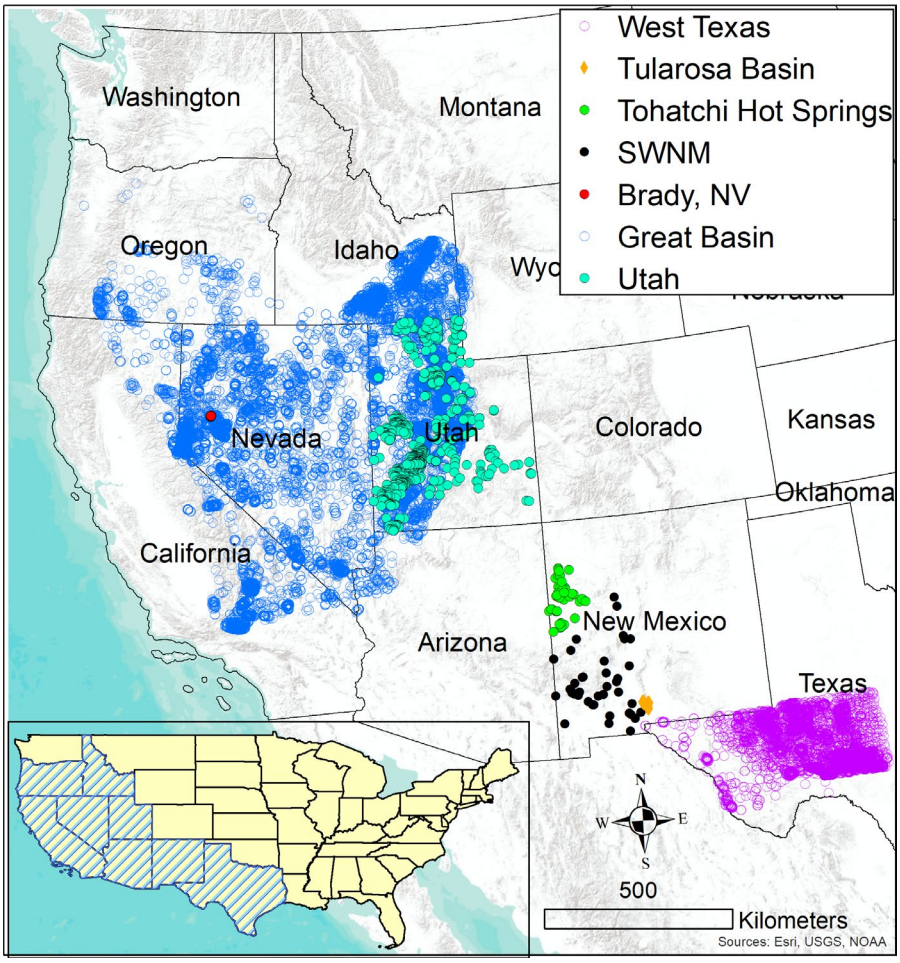

Fig. 1.6: Locations of 7 out of 9 analyzed site datasets by the GTC framework. Datasets for Hawaii and EGS Collab are not shown here.

1. **West Texas:** Westen Texas has a rich well dataset that provides the opportunity for refined resource mapping. We analyzed this region using three geothermal attributes including thermal conductivity, heat flow, geothermal gradient, and bottom hole temperatures to estimate the temperature at depth and suitability for geothermal development

2. **Great Basin**: In this dataset, we analyzed 18 shallow water chemistry attributes at 14,342 locations. This work extracted hidden geothermal signatures associated with low-, medium-, and high-temperature hydrothermal systems, their dominant characterization attributes, and spatial distribution within the study area[36]. The analyses are based on the public data available on the Nevada Bureau of Mines and Geology website.

3. **Southwest New Mexico (SWNM)**: Here, we analyzed 18 attributes at 44 locations and identified low- and medium-temperature hydrothermal systems; found dominant attributes and spatial distribution of extracted hidden hydrothermal signatures; demonstrated blind predictions of the regional physiographic provinces[1].

4. **Brady site, Nevada**: We identified key geologic factors controlling geothermal production in the Brady geothermal field[37].

5. **Tularosa Basin, New Mexico**: Analyzed 21 Play Fairway Analysis (PFA) attributes at 120 locations[38]; data comes from past PFA work in this region[39]. ML analyses identified geothermal signatures associated with low-, medium-, and high-temperature hydrothermal systems. Dominant attributes and spatial distribution of the geothermal signatures were also defined.

6. **Tohatchi Springs, New Mexico**: Explored 19 geothermal attributes at 43 locations in Tohatchi Springs, New Mexico[40]. Successfully defined geothermal signatures associated with low- and medium-temperature hydrothermal systems. Also, we found their dominant attributes and spatial distribution.

7. **Hawaii**: Analyzed four islands' data separately and jointly; ML identified low-, medium-, and high-temperature hydrothermal systems and their dominant characterization attributes[41].

8. **Utah FORGE**: Performed prospectivity analysis to identify future drilling locations using geological, geochemical, and geophysical attributes[42]. Maps of temperature at depth and heat flow are constructed based on the available data. Processed data includes satellite (InSAR), geophysical (gravity, seismic), geochemical, and geothermal attributes. Prospectivity maps were generated, and drilling locations were proposed for future geothermal field exploration.

9. **EGS Collab:** Field-laboratory data from the Sanford Underground Research Facility (SURF) was processed to extract dominant temporal patterns observed in 49 data streams; erroneous measurement attributes and periods were automatically identified; interrelated data streams were automatically identified. This work has not been published yet.

Setup and Usage

GTC can be used in three ways (i) on Julia, (ii) on Python, and (iii) on a Cloud platform (e.g. JuliaHub, Google Cloud Platform, Amazon Web Services, Azure Cloud Services through Docker). Julia's installation is explained at given below.

```
import Pkg
Pkg.add("GeoThermalCloud")
import GeoThermalCloud
GeoThermalCloud.SWNM() # performs analyses of southwest New Mexico
GeoThermalCloud.GreatBasin() # performs analyses of the Great Basin region
GeoThermalCloud.Brady() # performs analyses of the Brady site, Nevada.
```

The Python installation process is described below:

```
$ python3
import julia
julia.install()
from julia import Base
from julia import Main
Main.eval("import Pkg; Pkg.build(\"GeoThermalCloud\")")
```

Docker image can found at https://hub.docker.com/r/bulbulahmmed/geothermalcloud-v1.

Conclusions

GTC is an open-source cloud-based ML framework for geothermal exploration that can simultaneously handle both public and proprietary datasets. Also, it consists of a series of advanced pre-processing, post-processing, and visualization tools that tremendously simplify its application for real-world problems. These tools make the ML results understandable and visible even for non-experts; therefore, ML and subject-matter expertise are not critical requirements to use our ML framework. GTC utilizes a series of novel LANL-developed patented ML tools called SmartTensors (https://github.com/SmartTensors). SmartTensors has already been applied to solve a wide range of real-world problems, from COVID-19 to wildfires (http://tensors.lanl.gov), and it has won two 2021 R&D 100 awards, including a bronze award for market disruptor tools. Now, it has two components (i) GTC and (ii) GeoDT-ML.

GTC is developed to process and analyze diverse small and large datasets. Also, it can handle sparse datasets with missing values. It analyzes and finds actionable information to enable decision-makers to make sound decisions for geothermal exploration, development, and production. It finds such actionable information by finding mapping functions between all input parameters. We analyzed eight diverse site datasets and found critical information that would not be possible by visual inspection or any other statistical tools. Overall, GTC can (1) analyze large field datasets, (2) assimilate model simulations (large inputs and outputs), (3) process sparse datasets, (4) perform transfer learning (between sites with different exploratory levels), (5) extract hidden geothermal signatures in the field and simulation data, (6) label geothermal resources and

processes, (7) identify high-value data acquisition targets, and (8) guide geothermal exploration and production by selecting optimal exploration, production, and drilling strategies.

GeoDT-ML

Introduction

GeoDT-ML is an ML-based version of GeoDT, which is a fast, simplified multi-physics solver to evaluate EGS designs in uncertain geologic systems[3,4,6]. It is numerically efficient enough to model thousands of realizations in a few hours using a desktop computer. The underlying assumptions of this model are empirically based on laboratory and field data to partially account for complex coupled processes, obviating the need to run expensive numerical simulations. The intent of this model is to run it with full uncertainty, as informed by a broad spectrum of relevant prior laboratory and field measurements, and to reduce the uncertainty only when suitable information is available. When a promising EGS design is identified, it can be investigated in greater detail and at higher fidelity using other more powerful but more expensive numerical modeling codes.

The primary features of *GeoDT-ML* include (Fig. 1.7):

1. Pressure and flow rate prediction for 3D networks of intersecting wells and fractures modeled as pipes and nodes.
2. Hydraulic stimulation prediction with shear and tensile mechanisms where fracture apertures depend on effective stress.
3. Transient heat production predictions that depend on fluid enthalpy, rock conductivity, and stored energy change over time.
4. Electrical power generation using the combined single-flash Rankine and isobutane binary cycle.
5. Net present value prediction based on geothermal cost estimation tools, electricity sales, and a simple earthquake cost model.

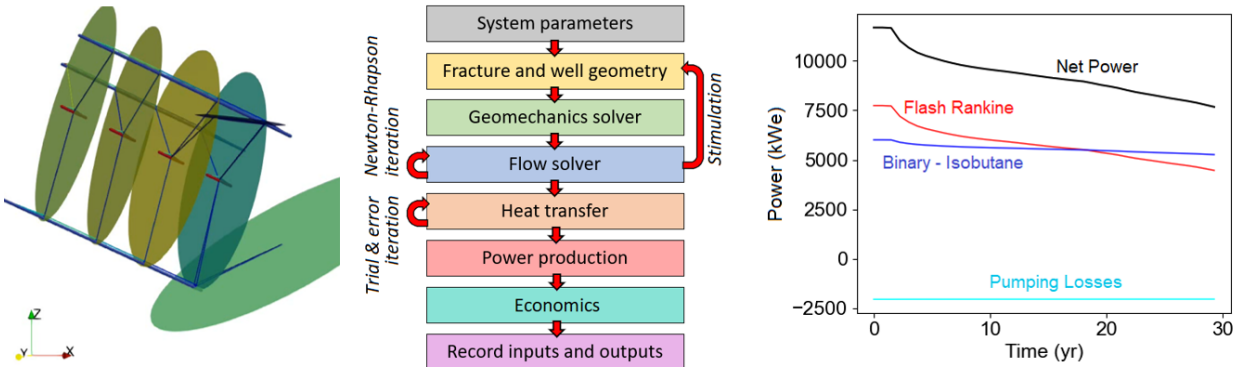

Fig. 1.7: GeoDT or GeoDT-ML stochastically predicts reservoir parameters, flow networks, hydraulic stimulation, heat production, power production, injection-induced seismicity potential,

and ultimately net present value by fast and simplified methods. Most models complete in ~15 seconds using a common desktop computer with a single processor thread.

Multiple datasets have been generated using GeoDT for EGS Collab and Utah FORGE site. One was used for the PIVOT 2022 Datathon to simulate the whole geothermal development cycle from the initial well design to the end of production. This dataset includes the Utah FORGE site characteristics and its measured uncertainties. The database includes 44,492 unique realizations, each with at least 30 years of production. Based on site characteristics, fractures are stochastically created (Fig. 1.8). Next, simulations are performed to compute power outputs for each situation (Fig. 1.9).

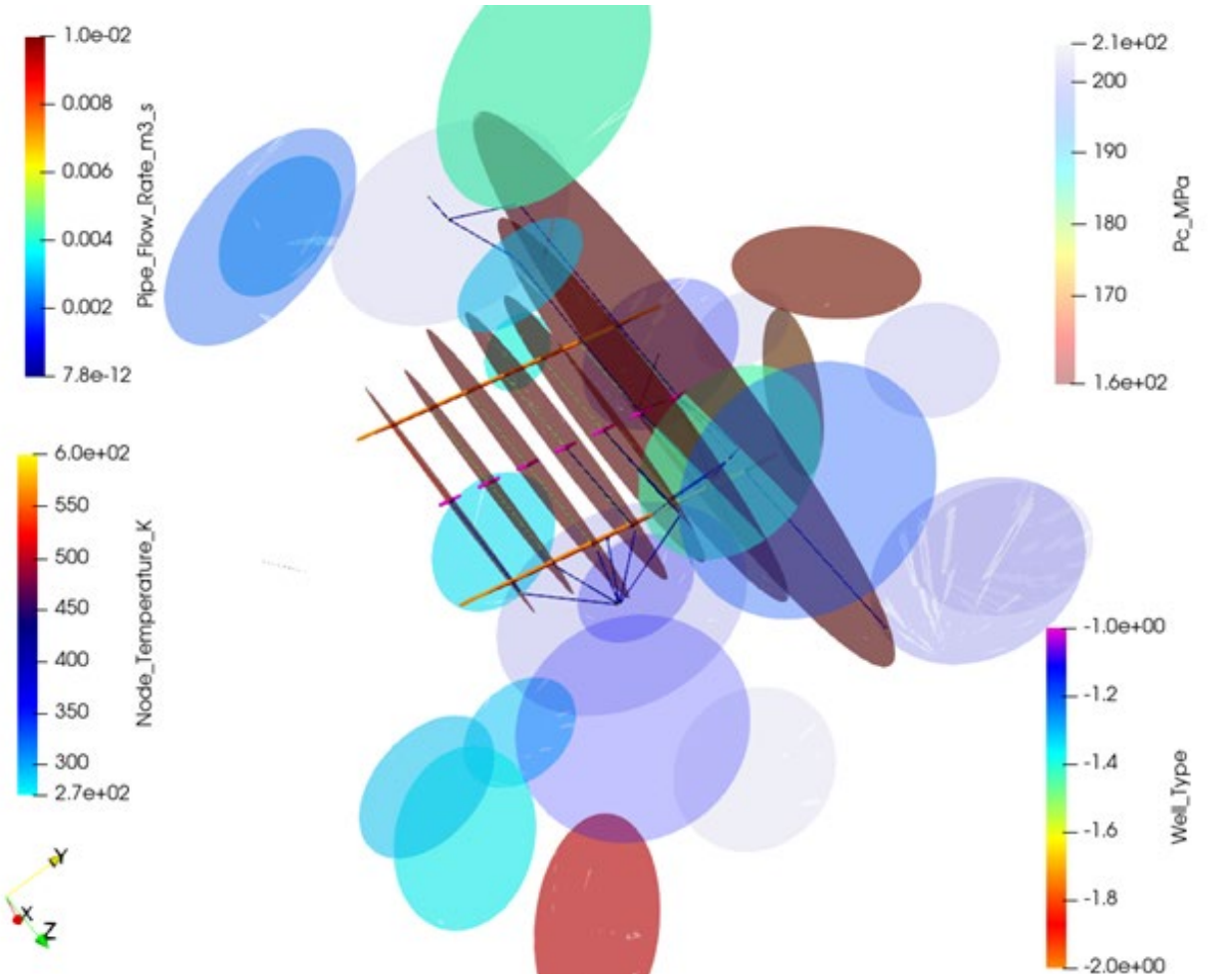

Fig. 1.8: Stochastically generated fracture and well scenario with injection into one well across seven isolated intervals and production from two bounding wells. The parallel hydraulic fractures propagated from each injection interval are shown in red, indicating that these fractures require relatively low pressure for activation (Pc).

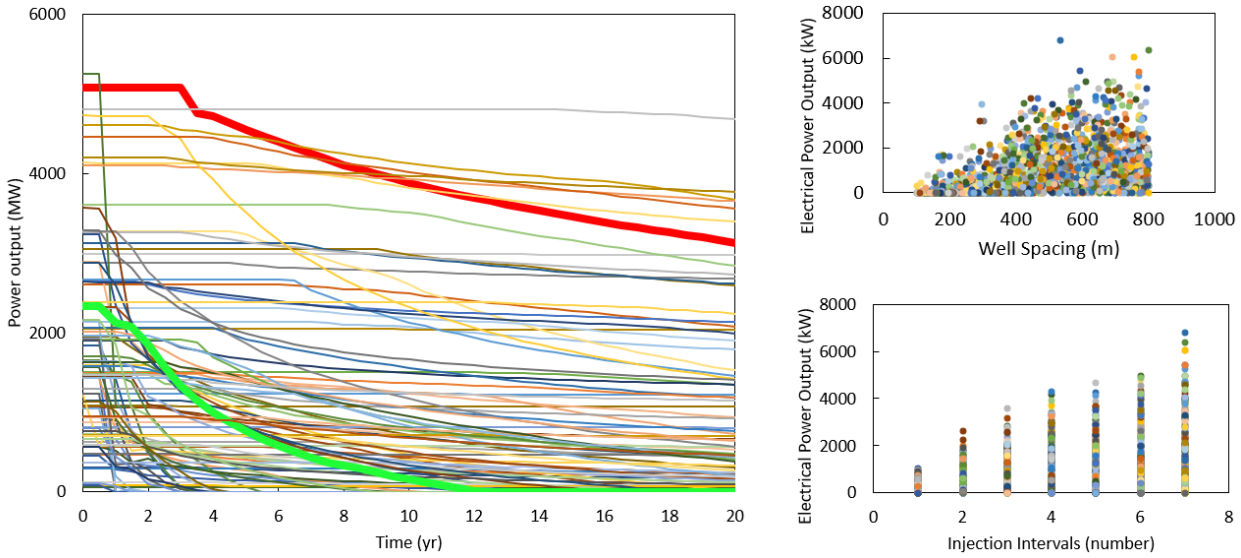

Fig. 1.9: Geothermal power production simulations based on the Utah FORGE parameters. In the time series plot, a high-performing case is highlighted in red, and a poor performer is highlighted in green. There is also a clear link between the well spacing and power output in addition to the number of injection intervals (i.e., isolated zones) and power output (plots on the right).

GeoDT-ML Workflow

In this section, we describe the workflow scripts for GTC for EGS techno-economic analysis. The Python scripts for the workflow development are available at https://github.com/SmartTensors/GeoThermalCloud.jl/tree/master/EGS/GeoDT_ML_v1/Python_Scripts. Jupyter Notebooks and Google Colab notebooks will be made available in the future at this GTC GitHub location.

Data Processing and Curation

The GeoDT code (https://github.com/GeoDesignTool/GeoDT.git**)** is used to generate the training database[3,4]. The data for DL modeling is available at https://github.com/SmartTensors/GeoThermalCloud.jl/tree/master/EGS/GeoDT_ML_v1/Data. In our study, a total of 4078 realizations are generated. The Python scripts – *get_inp_out.py* and *get_preprocessed_data.py* are used to process the raw data and curate it using various pre-processing methods such as StandardScaler, MinMaxScaler, MaxAbsScaler, RobustScaler, PowerTransformer (Yeo-Johnson), QuantileTransformer (uniform output), and QuantileTransformer[43]. The Python script – *get_train_val_test_splits.py* allows us to split the curated data into 80% training, 10% validation, and 10% testing. When the DL model identifies a promising EGS design, it can then be further investigated in greater detail. For example, we can use high-fidelity process models and simulation codes such as PFLOTRAN[44] to explore promising EGS scenarios. This current study does not include the use of high-fidelity codes, but these Python scripts can be leveraged and modified to perform such DL analysis with minimal effort.

Local and Global Sensitivity Analysis

The data worth analysis is performed using the *get_ftest_mi_npv.py* and *get_ftest_mi_npv_others.py* scripts. These Python scripts allow us to perform local and global data worth analysis. Sensitivity analysis is performed using two different approaches, F-test and mutual information[45–47]. F-test is a univariate linear regression test returning F-statistic and p-values. It provides insights on the linear dependency of a given EGS design parameter with respect to economics (e.g., undiscounted cash flow), thereby allowing us to identify potentially predictive design parameters for DL model training for undiscounted cash flow. On the other hand, mutual information provides insights on the non-linear dependency between EGS design parameters and undiscounted cash flow. The MI between an EGS design parameter and undiscounted cashflow is a non-negative value and is equal to zero if and only if two variables are independent, and higher values mean higher non-linear dependency.

DL Model Training and Hyperparameter Tuning

This curated data is given as input to deep neural networks, which are trained on multiple cores available on high-performance computing machines (HPC). This AI training at scale is performed in parallel, allowing us to train and tune various deep neural networks in minimal time. We combine Python and AI modules such as mpi4py, multiprocessing, parallel hdf5, and TensorFlow to achieve this training at scale. The performance of the trained DL models is compared using the validation loss, and a tuned model is then selected. This hyperparameter tuning is computationally intensive and requires a lot of HPC resources. Python scripts such as *get_dir_hp_dnn_*.py* and *get_dnn_results_*.py* are available to achieve this. They provide specifics on how to run on MacOSX, Linux, and HPC resources. We trained these models on an HPC resource at PNNL using 20,000 CPU cores. Fig. 1.10 shows a plot of one such DL model training and inference.

Conclusions

GeoDT-ML is an ML-based version of GeoDT, a fast, simplified multi-physics solver to evaluate EGS designs in uncertain geologic systems. It is numerically efficient enough to model thousands of realizations in a few hours using a desktop computer. It is designed to find prospective enhanced geothermal systems in hot, dry rocks. In this study, we developed and provided preliminary DL workflow scripts to estimate EGS economics from design parameters. The database for DL model training is developed using GeoDT, a multi-physics solver. Sensitivity analysis using F-test and mutual information is performed on this database to gain insights into the GeoDT parameters. The DL model training requires HPC resources as training and hyperparameter tuning is computationally expensive. To overcome this challenge, we will also provide notebooks and pre-trained ML models in GitHub for the geothermal community. Advanced hyperparameter tuning scripts using open-source software such as DeepHyper and Keras-Tuner will also be made available at https://github.com/SmartTensors/GeoThermalCloud.jl/tree/master/EGS.

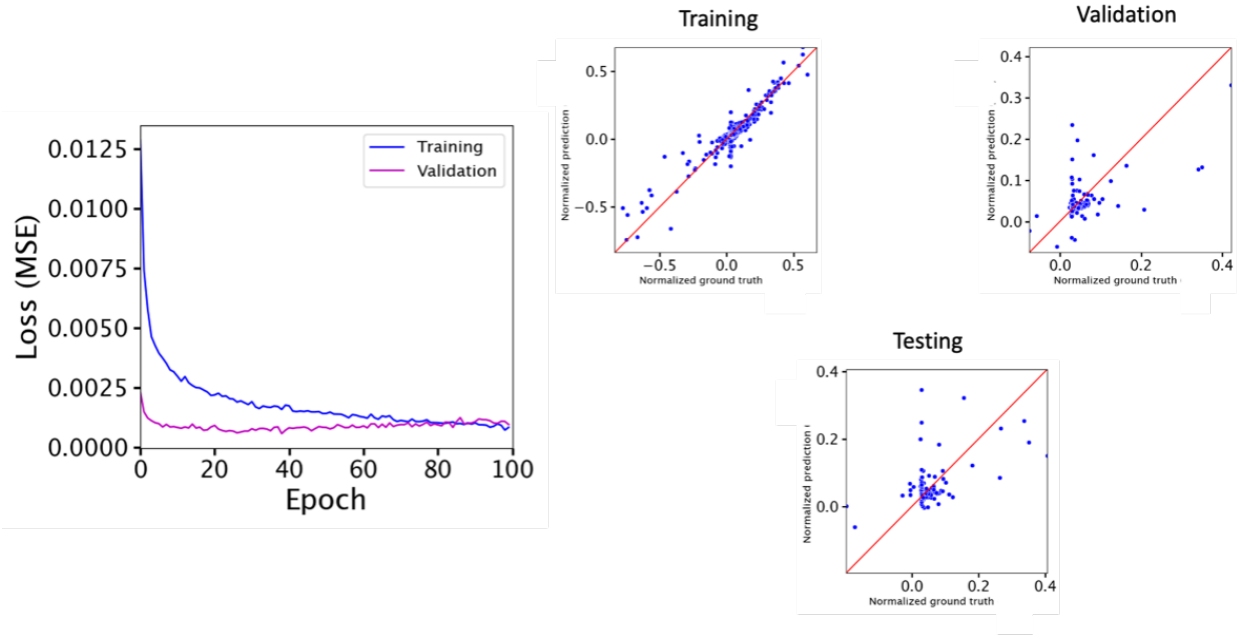

Fig. 1.10. Training loss and one-to-one plots for training, validation, and test datasets of a preliminary DL model. More than 20,000 DL models are trained on HPC resources to estimate the EGS economics. This trained deep neural network model has three hidden layers, with neurons [1000, 500, 250] in each of these layers. Leaky ReLU is used as an activation function with alpha value of 0.1. The dropout value, which allows for minimizing over-fitting during the training process, is assigned a value of 0.1. The total number of epochs for training is equal to 100. Batch size, which is the number of training samples that a DL model sees for each iteration in an epoch, is equal to 64. The resulting DNN has approximately 750K trainable weights.

Setup and Usage

The following are the steps to use the GeoDT-ML through GTC:

1. Create a virtual python environment (e.g., myenv)
    a. conda create --name myenv
    b. Install the following additional packages in the virtual environment: tensorflow, keras-tuner, mpi4py, h5py
2. Git clone https://github.com/SmartTensors/GeoThermalCloud.jl.git
3. cd to EGS/GeoDT_ML_v1/Python_Scripts
4. On terminal run – python <*file_name.py*>

These above instructions will be available through the readme markdown file on GTC. As the scripts utilize HPC resources for training ML models, a user can use their own HPC systems to run these scripts in parallel. These parallel scripts are not available through Jupyter Notebooks or Google Colab notebooks. Such instructions will be made available at GTC GitHub repository.

Publications

1. AI pinpoints renewable energy in *Albuquerque Journal*, 2020.
2. Unearthing clean energy in LANL magazine 1663.

YouTube Videos

3. GeothermalCloud: https://www.youtube.com/watch?v=ryFxdyQgCJg&list=PLpVcrIWNlP22LfyIu5MSZ7WHp7q0MNjsj&index=11
4. SmartTensors Platform: https://www.youtube.com/watch?v=ni3EgQVypbQ&list=PLpVcrIWNlP22LfyIu5MSZ7WHp7q0MNjsj&index=17.
5. NMFk optimization process: https://www.youtube.com/watch?v=6NAvJmY3Ae8&list=PLpVcrIWNlP22LfyIu5MSZ7WHp7q0MNjsj&index=36
6. Unsupervised ML workshop GSA: https://www.youtube.com/watch?v=8a6Gw29RHcM&list=PLpVcrIWNlP22LfyIu5MSZ7WHp7q0MNjsj&index=12

Demo Problems

7. SWNM: https://github.com/SmartTensors/GeoThermalCloud.jl/tree/master/SWNM/notebook
8. Brady: https://github.com/SmartTensors/GeoThermalCloud.jl/tree/master/Brady/notebook
9. Great Basin: https://github.com/SmartTensors/GeoThermalCloud.jl/tree/master/GreatBasin/notebook
10. Ingenious: https://github.com/SmartTensors/GeoThermalCloud.jl/tree/master/Ingenious/notebooks
11. Utah FORGE: https://github.com/SmartTensors/GeoThermalCloud.jl/tree/master/utah
12. GeoDT-ML: https://github.com/SmartTensors/GeoThermalCloud.jl/tree/master/EGS/GeoDT_ML_v1/Python_Scripts

Chapter 2: Location Drilling Sites with NMFk and MT data in the Tularosa Basin

Introduction

The United States Energy Information Administration projects a 50% increase in global energy consumption between 2018 and 2050[48]. Specifically, in the United States, geothermal electric power capacity has the potential to increase from 2.3 GW_e in 2019 to 60 GW_e by 2050[49,50]. Geothermal energy is generated from the decay of naturally occurring radioactive elements and stored deep in the subsurface. Even though there is essentially an inexhaustible geothermal energy supply in the subsurface, much of the heat is unevenly distributed, seldomly concentrated, and too deep to be economically exploited[51]. However, there are locations where thermal energy is accessible by drilling that are the targets for geothermal exploration.

Productive geothermal systems have three major characteristics: high heat flow, temperature, and permeability. Geothermal resources are confined to regions of high heat flow and temperature due to magmatism and/or crustal thinning[52]. Specifically, extensional settings exhibit intermediate to high heat flow that can be the target of geothermal exploration, and temperatures of 125–225°C can produce geothermal energy[52,53]. However, finding the optimal location for the development of such resources and the potential depth of drilling is challenging because of high drilling and development costs. Typically, play fairway analysis (PFA), a heavily used tool in the hydrocarbon industry, is used for finding spatial locations of geothermal resources. Next, an magnetotellurics (MT) survey or exploration drilling is performed to identify the optimal drilling depth. PFA separately computes the importance of each attribute in a geothermal dataset and estimates a composite score by combining scores for all attributes. The composite score is used for defining spatial locations of geothermal resources. Such a study has a significant human bias. Here, we propose an ML-based alternative PFA approach that simultaneously analyzes all attributes in a dataset without human intervention to find spatial locations of geothermal resources. Finally, we integrate MT data in the workflow to identify the most prospective drilling depth. Note that no such study in the literature combines ML-based PFA and MT data.

Integrating ML and geophysical techniques assesses heat flow, temperature, and permeability for geothermal exploration and development. Here, we use unsupervised ML called non-negative matrix factorization with k-means clustering (NMF*k*). This approach clusters/groups data related to heat flow, temperature, and permeability to establish groups with geothermal resource significance in both attribute and spatial domains[16,54].

NMF*k* has been successful in various geothermal applications in identifying the location of potential geothermal resources[35] and geologic factors associated with geothermal production[37]. MT is a passive geophysical technique used for measuring electrical resistivity structures in the subsurface and is commonly used to characterize geothermal resources[28–31,55]. Generally, high-potential geothermal systems are characterized by low resistivity because of the high salinity of geothermal fluids. Geothermal systems commonly include faults and fractures filled with highly conductive high-salinity fluids. In addition, clay products from mineral alteration in a geothermal system also have low electrical resistivity. The correlation between low resistivity measurements and geothermal resources makes MT surveys ideal for geothermal resource development.

This study aims to demonstrate how NMF*k* analysis identifies the most prospective locations for geothermal resource development, and MT inversion aids in the subsurface characterization of those resources. Play fairway analysis (PFA) performed by Ruby Mountain Inc. and the Energy and Geoscience Institute at the University of Utah identifies two highly prospective geothermal locations within the Tularosa Basin, New Mexico: White Sands Missile Range and the McGregor Range at Fort Bliss. Due to data limitations, heat flow, temperature, and permeability data from White Sands Missile Range is used to demonstrate the ability of NMF*k* to characterize a predetermined high-potential geothermal location further, whereas McGregor Range is used to demonstrate the ability of MT data to identify geothermal prospects in the subsurface. Finally, we demonstrate how NMF*k* and MT may be integrated to provide a 3D assessment of high-potential geothermal resources, facilitating fast and economic geothermal play development.

Geologic Background

The Tularosa Basin is located on the eastern flank of the Late Paleogene Rio Grande rift[56,57]. The Rio Grande Rift occurs as a north-trending, intermontane graben within south-central New Mexico and is bounded to the east by the Sacramento Mountains and to the west by the Organ and San Andreas Mountains (Fig. 2.1). Faults associated with the Rio Grande Rift have several thousand feet of displacement and separate the basin from the surrounding uplifted mountains[56]. Paleogene rifting induces high heat flow within southwestern New Mexico, making the southern portion of the Tularosa Basin favorable for geothermal exploration[39]. In the basin's southern part, temperatures recorded from wellbores range from 170°C to 200°C[58], and clay mineral analysis indicates temperatures as high as 225°C[59,60].

The Tularosa Basin is filled with strata of Paleozoic to Tertiary age[58,60–62] (Fig. 2.2). Bedrock consists primarily of Paleozoic carbonates, including Ordovician and Silurian dolomite, Devonian, and Mississippian interbedded chert-rich shales and limestones, and Pennsylvanian limestone with thinly bedded shales. Tertiary felsic intrusions commonly crosscut the Paleozoic bedrock, and Quaternary graben fill overlies the bedrock. It is composed of gravel, sand, silt, and clay derived from prograding alluvial fans originating from the edge of the rift valley.

Data

The dataset has 10 attributes at 120 locations (Fig. 2.3). With an observational dataset, obtaining values for 10 attributes at each location is difficult. In this study, the only attribute available at all 120 locations is temperature 2 m, and the remaining attributes had missing values for some locations. To address the missing values, we apply the nearest neighbor interpolation techniques[63] based on distance (not points) to heat flow, gravity, NaK-Giggenbach geothermometer, K-Mg geothermometer, NaK-Fourneir geothermometer, silica geothermometer, and Li^+ concentration. The distance is calculated using a variogram analysis. We also use block mean[64], kriging[65], and inverse distance weighting[26] interpolation techniques. However, the nearest neighbor method provides the best results for the dataset used in this study. R^2 score (Eq. 1.7) based on interpolated and actual values is used to evaluate four interpolation techniques. ArcMap is used to interpolate fault distance and fault density values. Specifically, the near coverage tool was used to find the distance from the location to the nearest fault, and the kernel density function was used to calculate fault density.

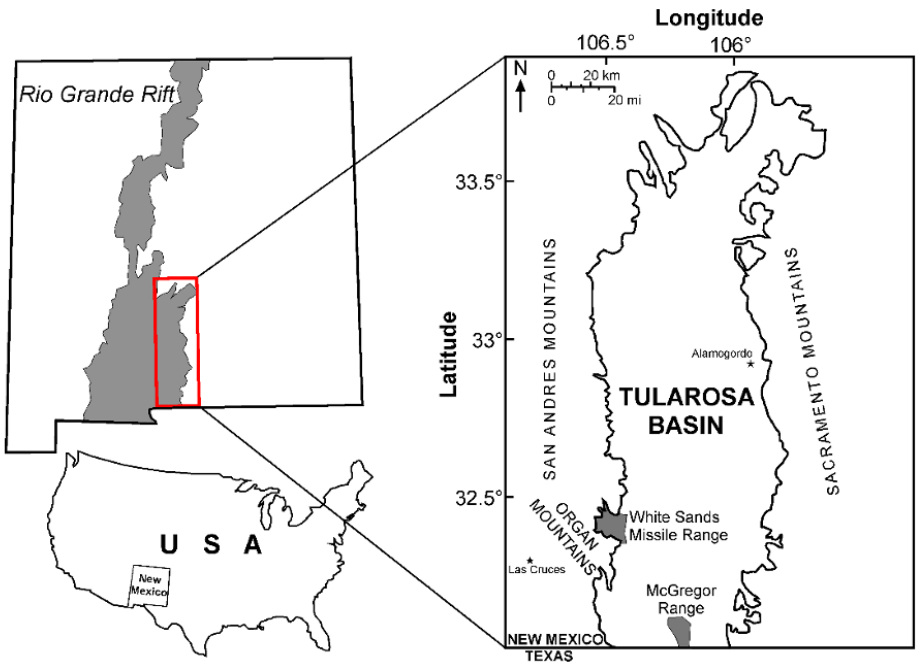

Fig. 2.1: Location of the White Sands Missile Range and McGregor Range study areas within the Tularosa Basin of southern New Mexico. The Tularosa Basin is an intermontane graben located on the eastern flank of the Rio Grande Rift.

	Stratigraphic Unit	Generalized Lithological Description
CENOZOIC	Quaternary	Alluvial basin fill
	Tertiary	Felsic sills and dikes
PALEOZOIC	Pennsylvanian	Black lime mudstones and wackestones; cherty limestones interbedded with grey shale
	Mississippian	Limestone interbedded with black shale
	Devonian	Black shale
	Silurian	Cherty dolomite
	Ordovician	Dolomite

Fig. 2.2: Generalized stratigraphic succession of the Tularosa Basin sedimentary and igneous fill.

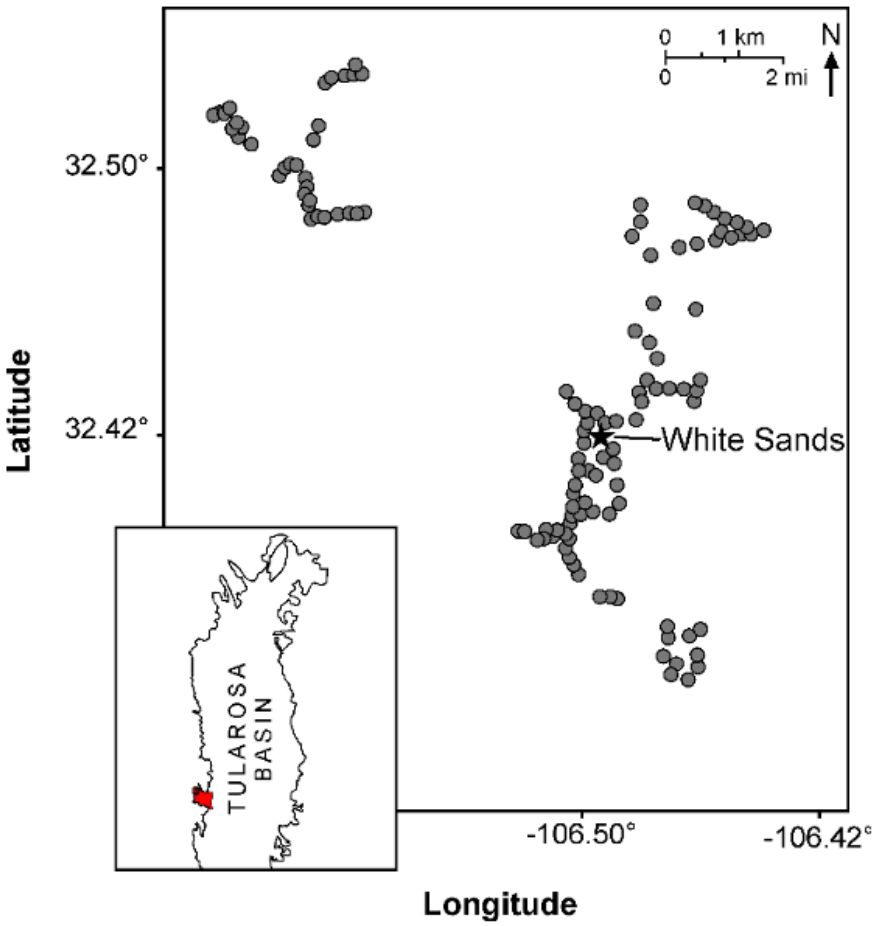

Fig. 2.3: Locations (120 total) near White Sands is selected as input data for NMFk. At each site, 11 geothermal attributes are collected and used as input into the NMFk model.

A 56-station MT survey was conducted at the McGregor Range by Quantec Geoscience, and the inversion modeling was completed by the Energy and Geoscience Institute at the University of Utah (Fig. 2.4)[39].

Results

Geothermal Characterization of NMFk Signatures

We applied NMFk to the dataset, which determines the optimal solution by evaluating reconstruction quality and average silhouette width (Fig. 2.5). Optimal solutions have low and high values. Generally, low and >0.25 are acceptable solutions[1,66]. NMF*k* is run for 2 to 10 signatures, and the k=4 solution is optimal because of its low and high values. The solution with k<4 is an underfitting data representation, whereas k>4 is an overfitting data representation.

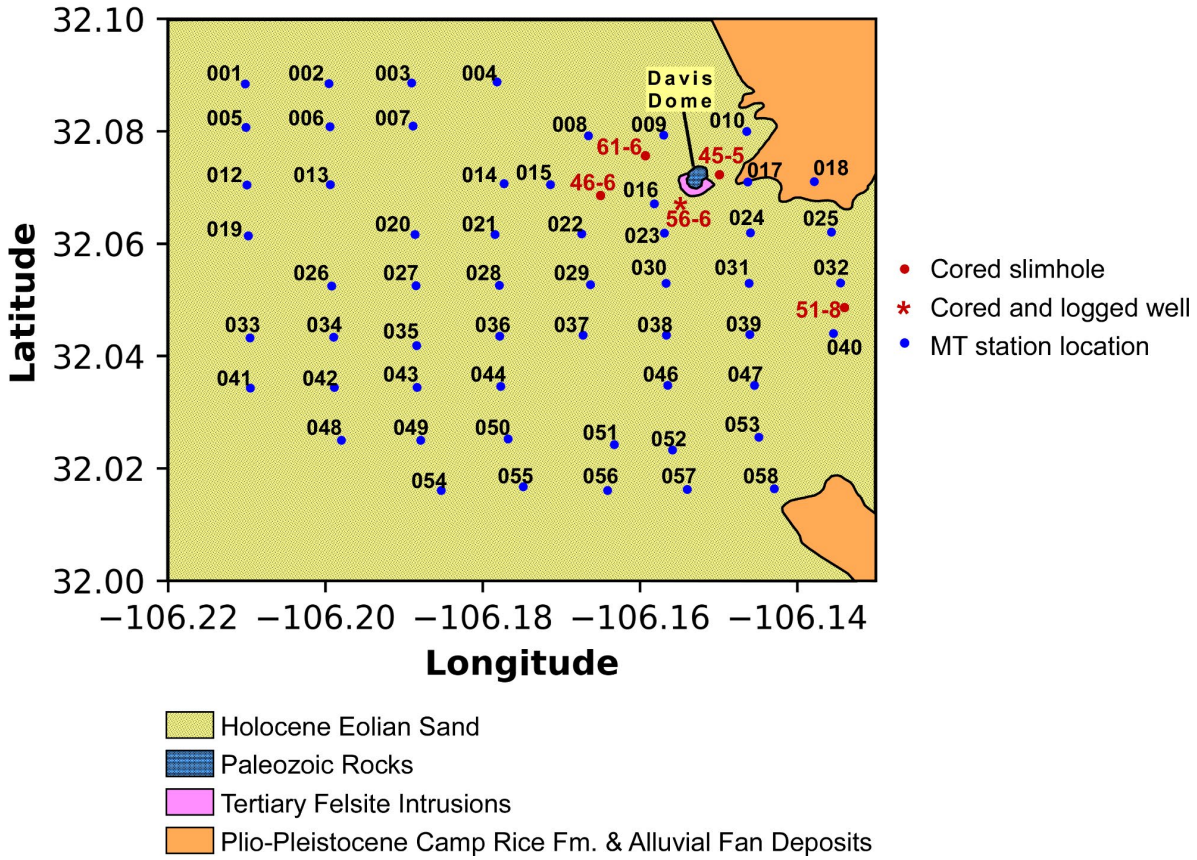

Fig. 2.4: Geologic map of the McGregor Range with MT station locations (blue) and slimhole core locations (red). Recent eolian sands largely cover McGregor, although Paleozoic and Tertiary outcrops occur in the northeast portion of the study area at Davis Dome.

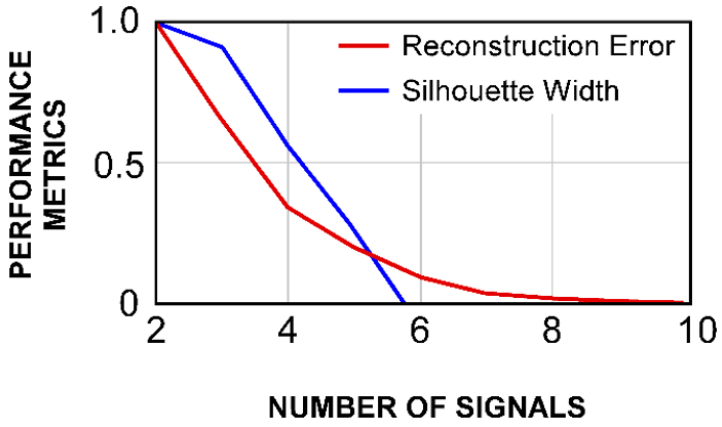

Fig. 2.5: NMFk reconstruction error (red curve) and silhouette width (blue curve) for different numbers of clusters k. The optimal k value has low reconstruction error and higher silhouette values. In this study, the optimal number of signatures is 4.

Each column of the attribute matrix, H_{nxk}, is known as a signature and captures certain characteristics in the dataset (Fig. 2.6A). The characteristics are defined by the contribution/weight of each attribute in a signature. The warm colors represent a high weight between the signatures and attributes, and the cool colors represent a relatively low weight (Fig. 2.6A). Furthermore, the warm colors correlate to high values for the geothermal attributes, and the cool colors correlate to lower values. The spatial distribution of each signature is plotted with a different color in Fig. 2.6B.

The dominant attributes of signature A are heat flow, K-Mg geothermometer, silica geothermometer, and quaternary fault density, indicating high heat flow, subsurface temperature, and permeability. Like signature A, signature B is characterized by high heat flow, temperature 2 m, and Li^+ concentration. Furthermore, the high Li^+ concentration indicates that signature B is characterized by high vertical permeability. No geothermometer had a significant contribution to signature B. Fault distance is the major attribute in signature C. This indicates locations assigned as C have lower potential vertical permeability because they are relatively far from faults that act as conduits for fluid flow. Signature C is characterized by lower heat flow and temperature relative to the other signatures. The dominant attributes for signature D are the Na-K Giggenbach geothermometer and NaK-Fourneir geothermometer indicating high subsurface temperatures. Moderate weights for quaternary fault density and Li concentrations in signature D indicate relatively high permeability. Heat flow and temperature 2 m have a relatively low contribution to signature D.

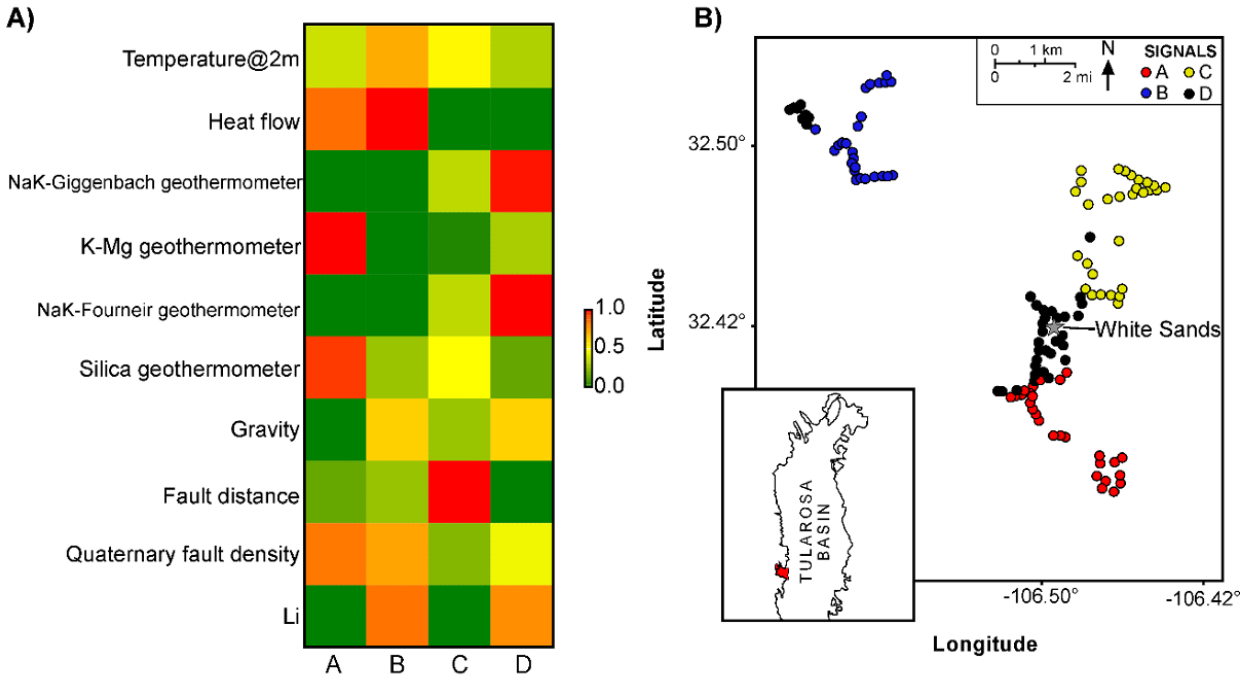

Fig. 2.6: Results from the NMFk model. A) Heatmap identifying the dominant geothermal attributes in each signature. The warmer the color the more dominant the attribute for a particular signature. B) Spatial distribution of signatures for the 120 locations at White Sands.

Apparent resistivity and phase curves display resistivity trends using the period as a proxy for depth (longer periods correspond to increased depth). Congruent MT apparent resistivity curves of Z_{xy} and Z_{yx} indicate a 1D resistivity structure, whereas separation indicates more complicated 2D or 3D resistivity structure[29]. For example, MT apparent resistivity curves for station 017 located in the northeast section of the survey show separation between the two curves at shorter periods, i.e., shallower depths (Fig. 2.7). This corresponds to geological structures related to Davis Dome, a small intra-bolson horst near station 017[60].

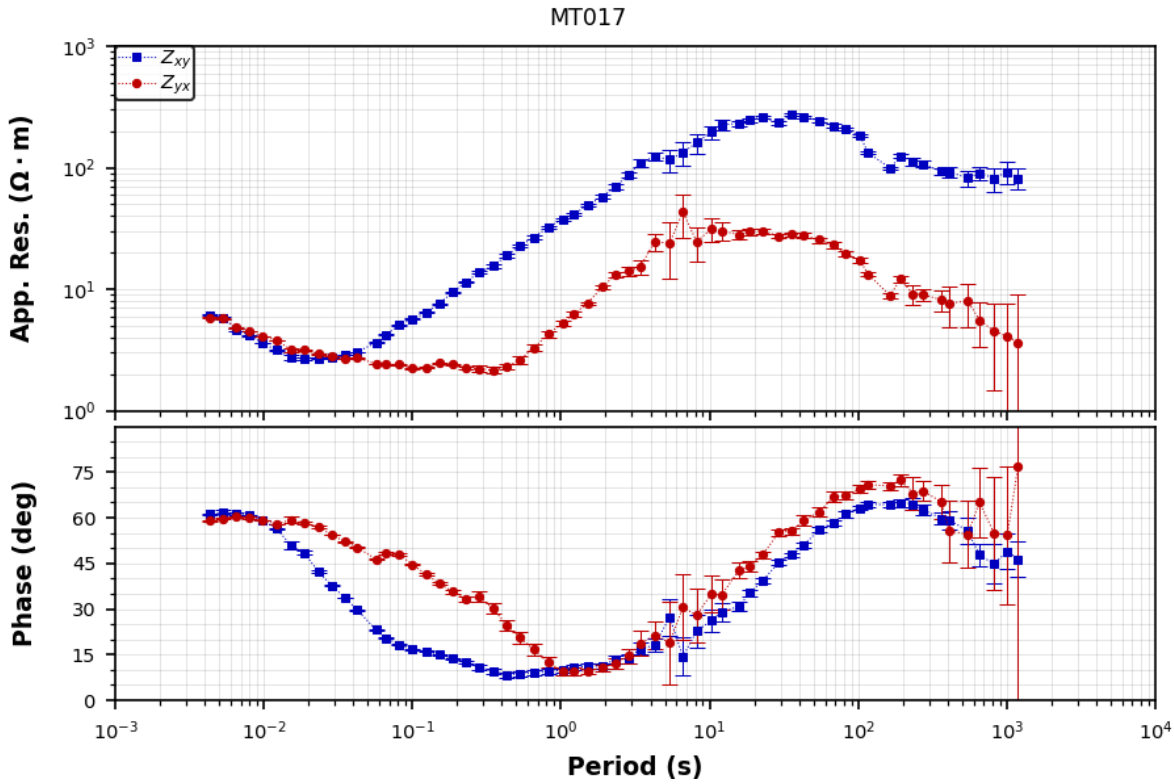

Fig. 2.7: Apparent resistivity curves for station MT017. The period is a proxy for depth, i.e., longer periods are deeper depths. Separation of, and curves at 0.05 s indicate 2D or 3D resistivity structures.

MT apparent resistivity and phase curves of Z_{xy} and Z_{yx} from all 56 MT sites are shown in Fig. 2.8. The apparent resistivity values show a cyclic trend from shorter to longer periods (shallower to deeper depths). At shallower depths, the apparent resistivity gradually decreases. Between 1 s and 100 s, the apparent resistivity increases. At deeper depths, longer than 100s, the apparent resistivity decreases. Furthermore, at longer periods, the Z_{xy} and Z_{yx} curves diverge indicating complex, 3D resistivity structure at deeper depths. The depth of the low apparent resistivity varies from east to west. For MT stations 019, 022, and 025 the troughs for apparent resistivity occur at 1 s, 0.3 s, and 0.1 s, respectively (Fig. 2.9). The longer period to the west indicates that the low resistivity unit occurs deeper in the west than in the east.

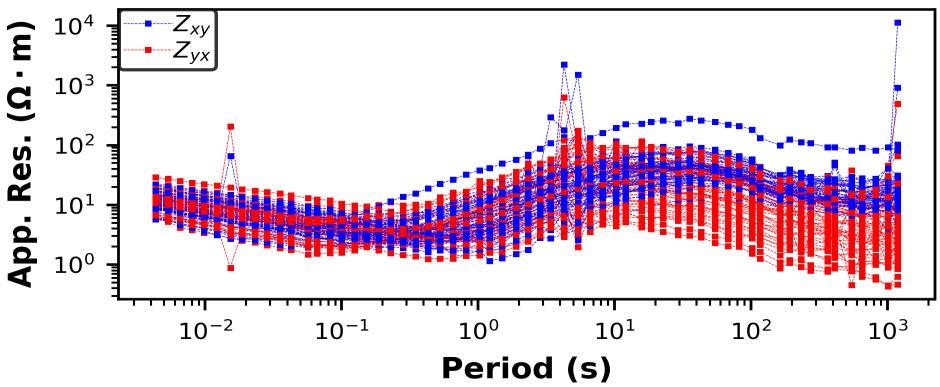

Fig. 2.8: The apparent resistivity from 56 MT stations is lower at shorter periods, increases at medium periods, and then decreases at longer periods for a low-high-low trend. Furthermore, at longer periods, the Z_{xy} and Z_{yx} curves separate indicating 2D or 3D structure at deeper depths.

The dimensionality of the resistivity structure is determined by phase tensors. One-dimensional resistivity structures indicate a natural change in resistivity with depth due to compaction[32,67]. Phase tensors are useful in identifying lateral variations (2D and 3D resistivity structures) in the underlying regional resistivity[32]. Lateral variations in resistivity result from changes in porosity due to fault- and/or fracture-related diagenesis and/or changes in lithology.

The phase tensor is commonly plotted as an ellipse with a minimum and maximum principal axis and skew angle, b (a measure of asymmetry) (Fig. 2.10A). In Fig. 2.10B, ellipses are colored based on the skew angle. Yellow colors indicate a skew angle of 0, and the red and blue colors indicate larger skew angles (± 5°). The larger the skew angle, the more asymmetric the phase tensor, indicating higher dimension resistivity structures. For 1D resistivity structures, the minimum and maximum principal axes are the same ($f_{max} = f_{min}$), resulting in the phase tensor characterized by a yellow, circular shape. The phase tensor of a 2D resistivity structure is characterized by an elliptical shape and skew angle close to zero (± 3°). For 3D resistivity structures, the phase tensor is asymmetric; hence, the phase tensor is characterized by blue or red. Furthermore, a rapid direction change in the phase tensor's principal axes between sites indicates a 3D resistivity structure[68].

In general, across the study area, the shorter periods are characterized by 1D resistivity structures and then higher dimension 2D and 3D resistivity structures with depth (Fig. 2.10B). This observation is consistent with the separation in apparent resistivity curves at longer periods (Fig. 2.7). Specifically, at 0.01s and 0.1s, the phase tensors are characterized by 1D structures, as indicated by the yellow circles. An exception to this observation is the northeastern corner of the study area, where the shape of the tensors is more elliptical, and the skew angle is higher, indicating lateral variation in the resistivity structure. This increase in dimensionality is consistent with shallow structural features and northwest-trending faults associated with Davis Dome[61]. The shape of the ellipses and the red, blue, and orange colors at periods greater than 1s indicate 2D or 3D resistivity structures. Specifically, the abrupt changes in the ellipse's shape at 10s suggest possible faulting. Caution must be taken when interpreting phase tensors at longer periods as they are more affected by attenuation.

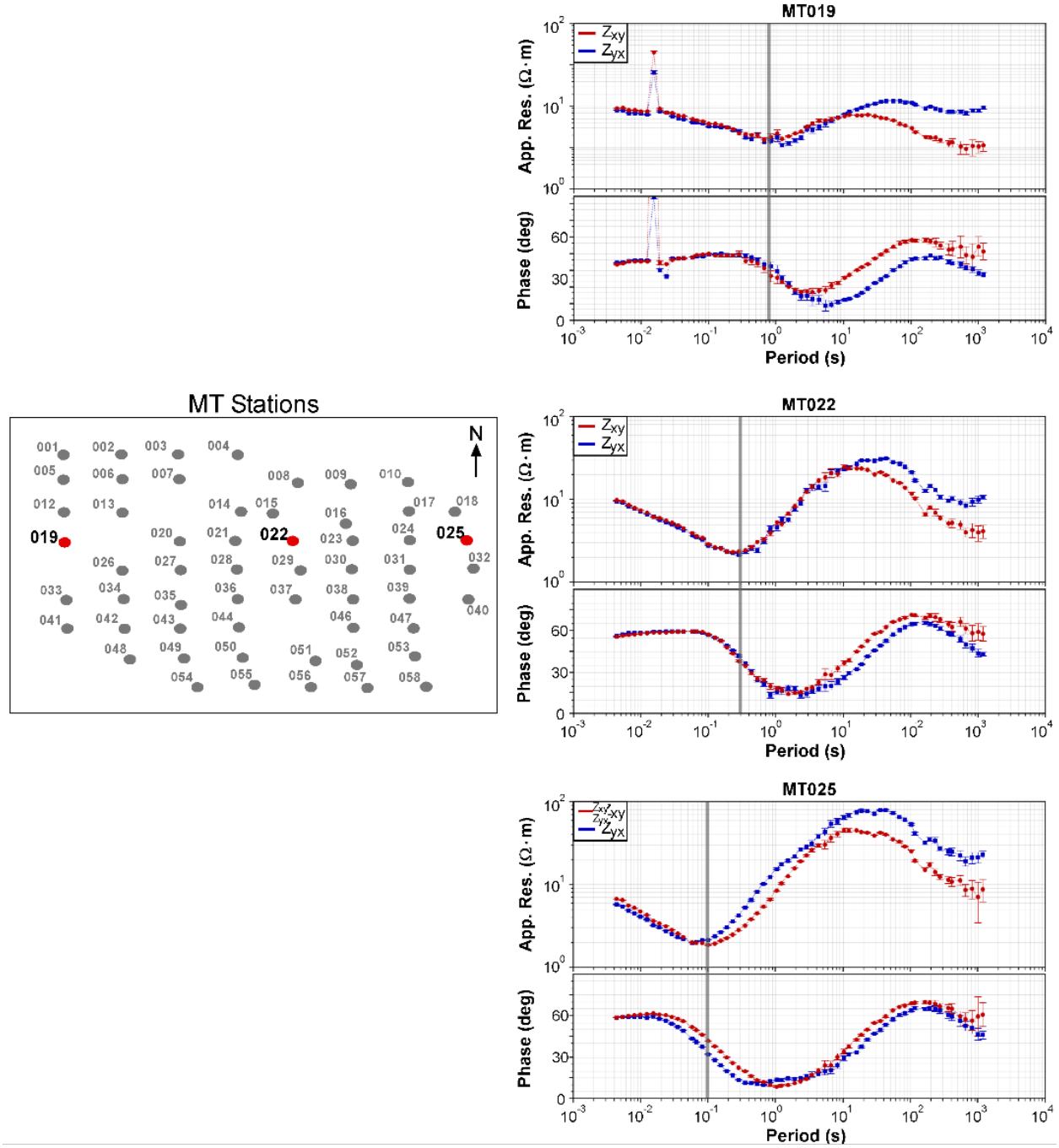

Fig. 2.9: Apparent resistivity curves for MT stations 019, 022, and 025. The curves show a change in the low resistivity unit depth from west to east. The low apparent resistivity trough of the Z_{xy} and Z_{yx} curves for MT019 occurs at 1s. The trough of the Z_{xy} and Z_{yx} curves for MT022 occurs at 0.3 s. The trough of the Z_{xy} and Z_{yx} curves for MT025 occurs at 0.1 s.

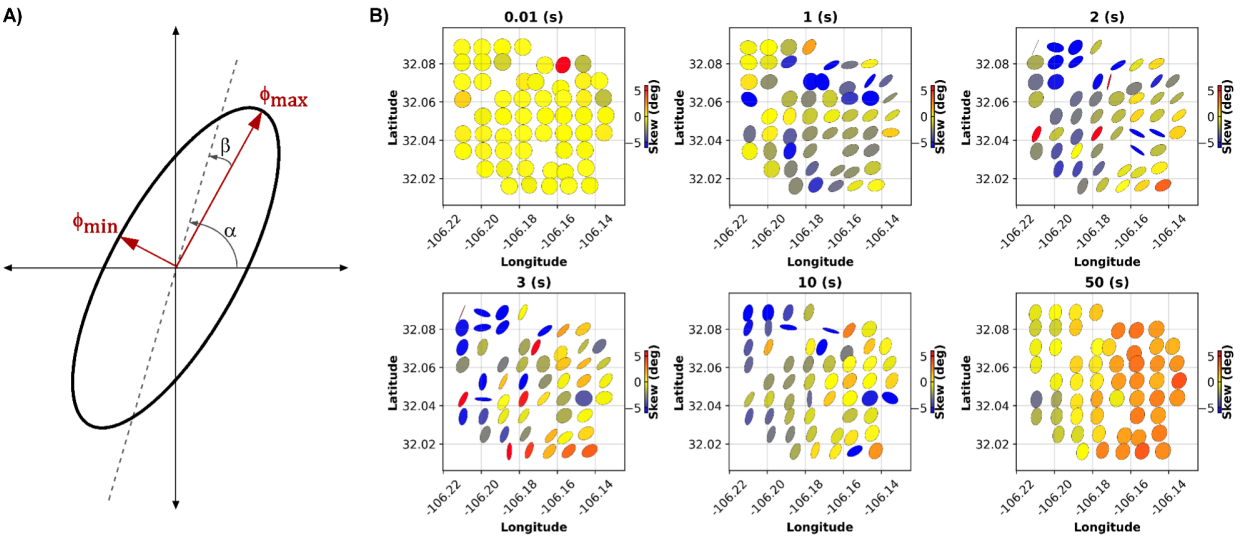

Fig. 2.10: A) Graphical representation of the phase tensor. B) Phase tensor maps at 0.1, 0.01, 1, 10, 50 and 100s indicate the spatial distribution of resistivity structures with depth.

Discussion

Geothermal Resource Potential

Temperature, heat flow, and permeability are the main geothermal attributes driving geothermal success[52]. The locations associated with signature A have high geothermal resource potential because of the characteristically high heat flow, high K-Mg and silica geothermometers, and medium to high quaternary fault density. Therefore, signature A has a high likelihood of possessing higher temperature, heat flow, and permeability compared to the other signatures. The locations associated with signature D have moderate geothermal potential because of the combination of high NaK-Giggenbach and NaK-Fourneir geothermometer values and low temperature at 2 m and heat flow. The locations associated with signature B have moderate geothermal potential because of high temperature at 2 m, heat flow, quaternary fault density, and Li^+ concentrations; however, low values for the geothermometers suggest subsurface temperatures may not be suitable for a geothermal resource. The locations associated with signature C have the lowest geothermal resource potential because no geothermal attributes have a major contribution to the signature.

MT Inversion Interpretation

Once a spatial location is determined through NMF*k*, MT can be a valuable tool to aid in the subsurface characterization of a potential geothermal resource by analyzing resistivity trends. Resistivity values are found through numerical inversion of MT data. Generally, geothermal fluid demonstrates low resistivity because of the presence of high-concentration elemental composition or total dissolved solids. The resistivity values of the McGregor geothermal system potentially indicate three resistivity layers and two resistivity structures (Fig. 2.11).

Layer 1 (L1) is characterized by the lowest resistivity (<8 Ωm) and is confined generally to the upper 500 m of the study interval. L1 is thickest to the west and thins to about 300 m in the east (Fig. 2.11). L1 is the thinnest in the northeast corner near Davis Dome. This regional low resistivity cap is most likely attributed to basin-fill deposits. O'Donnell, Jr., et al.[61] performed a seismic reflection survey over the same study area and observed a wedge-shaped feature above the bedrock attributed to alluvial fan deposits shed from the surrounding mountains. The observed thickening of L1 to the west in the MT data is consistent with the wedge-shaped feature observed in the seismic survey (Fig. 2.11).

Layer 2 (L2) is a low resistivity (10 – 100 Ωm) layer with the top 200 – 600 m beneath the surface. In general, L2 is shallower to the east (~300 m) and deeper to the west (~ 600 m). Wells drilled in the northeast portion of the study area suggest that the top of L2 corresponds to Paleozoic (Pennsylvanian limestone) bedrock[58,60]. Finger & Jacobson[58] observed and measured fracture permeability in cores in nearly all Paleozoic units. Phase tensor analysis in the western part of the study area indicates a 2D resistivity structure that suggests the presence of a possible fault system (Fig. 2.10B). The thicker and lower resistivity L2 in the west may be attributed to increased fractures and/or faults that act as storage or conduits for geothermal fluids decreasing resistivity, i.e., L2 in the west is influenced by higher fractured and/or faulted units.

A low resistivity structure (RS1) is present below MT stations 039, 047, 051, 052, and 053 in the southeast section of the study area (Fig. 2.11). The structure has similar resistivity as L2 but extends to 2000 m. The lower resistivity of RS1 is interpreted to be related to a deformation observed in surrounding wells. A thrust fault and overturned beds are observed in cores from well 51-8 located to the northeast of cross-section EW3, suggesting deformation in the area (Fig. 2.11). Units related to this structure are pervasively fractured and may provide a conduit for fluid flow and associated lower resistivity in RS1, as observed in Fig. 2.11.

A high resistivity structure (RS2) is present in the northeast portion of the study area and has similar resistivity values to L3 (Fig. 2.11). The spatial distribution of resistivity and cored wells in the area (45-5, 46-6, and 61-6) suggest RS2 coincides with structures related to Davis Dome, an intrusive igneous laccolith (Fig. 2.11). Cored wells encounter felsic sills, a felsic laccolith, and Mississippian limestone and shale at relatively shallow depths between 360 m and 530 m[58,61]. The thin L2 layer above RS2 is most likely fractured Paleozoic strata and high resistivity RS2 is most likely a low permeability felsic body associated with the Davis Dome intrusion. These interpretations are consistent with a structural high from a laccolith intrusion observed in reflection seismic data velocity and gravity models from O'Donnell Jr. et al.[61].

The west-central section of L2 is interpreted as a possible fault system with the highest geothermal potential. Geothermal reservoirs tend to have resistivity values between 10 – 60 Ωm, similar to those observed in L2[30,68]. The location where L2 is the thickest coincides with north-northwest trending, anomalously high thermal gradients (up to 140°C/km). The anomaly may be due to geothermal waters rising along a common fault zone or fractured bedrock adjacent to the fault zone[69], which is consistent with the highly faulted and/or fractured units observed in L2 to the west (Fig. 2.11). Furthermore, the westward thickening of L2 suggests the possibility for a corresponding increase in reservoir transmissivity and an increase in well productivity[70].

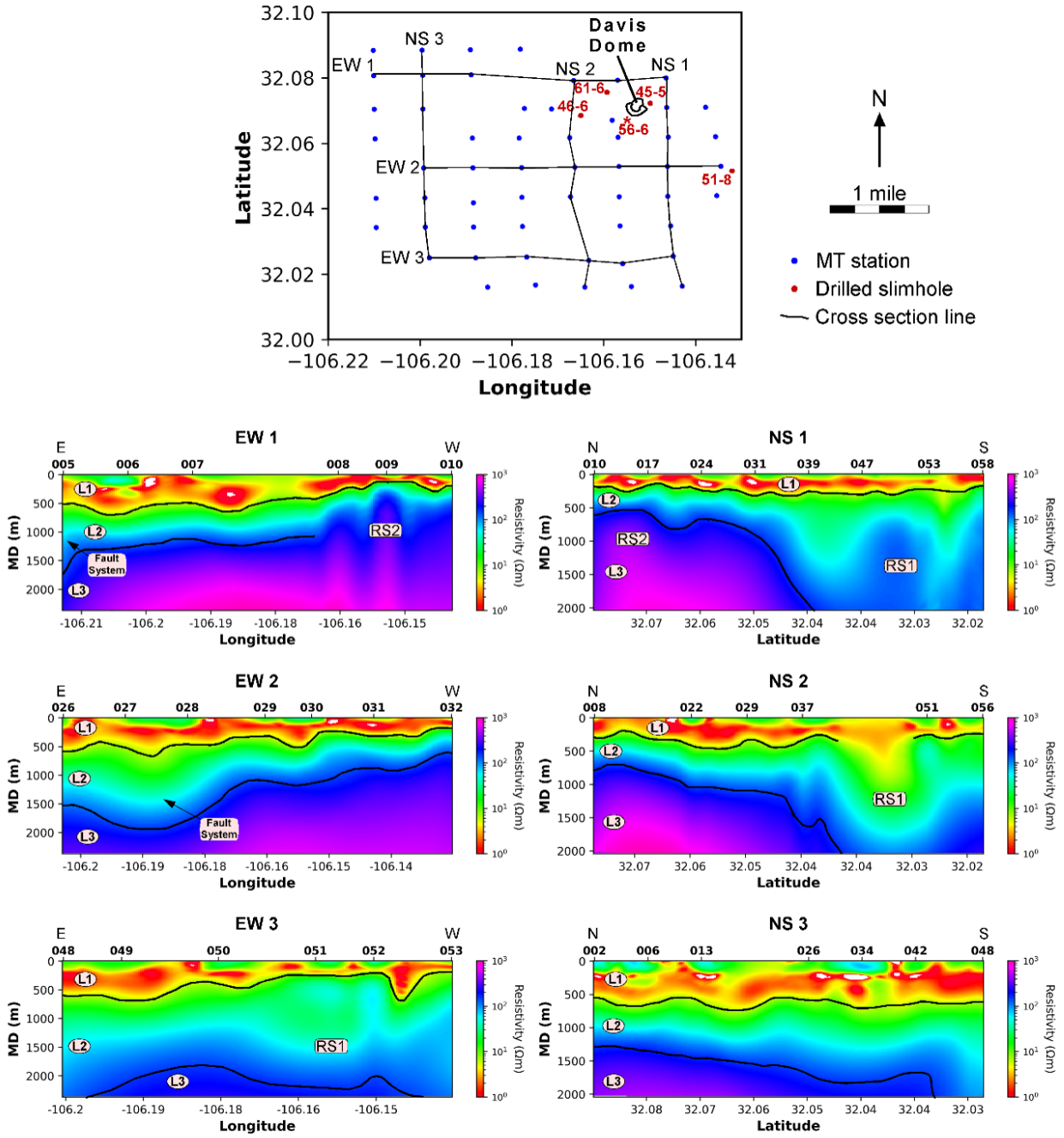

Fig. 2.11: Three north-south and east-west MT cross sections with interpreted resistivity layers and structures. The low resistivity to the west is interpreted as a fault system. The faults, fractures, and possible dissolution because of geothermal fluids increase porosity thus decreasing resistivity. Assuming temperature is consistent with a geothermal reservoir, the west-central part of the McGregor Range has the highest geothermal potential because of the increase in porosity and associated permeability attributed to the interpreted fault system.

Limitations of MT

MT data is limited by its hectometer-scale vertical resolution. Resistivity is measured in well 56-6 using wireline logs with a vertical resolution of 0.6[71]. Compared to inverted MT resistivity, the well logs provide more detailed variations in resistivity (Fig. 2.12). For example, from 90 – 220 m, well-log resistivity is characterized by high variability due to thinly interbedded limestones and shales that are not detected in the MT resistivity. Only general interpretations of fluid saturation and porosity can be made with MT data because of the low vertical resolution.

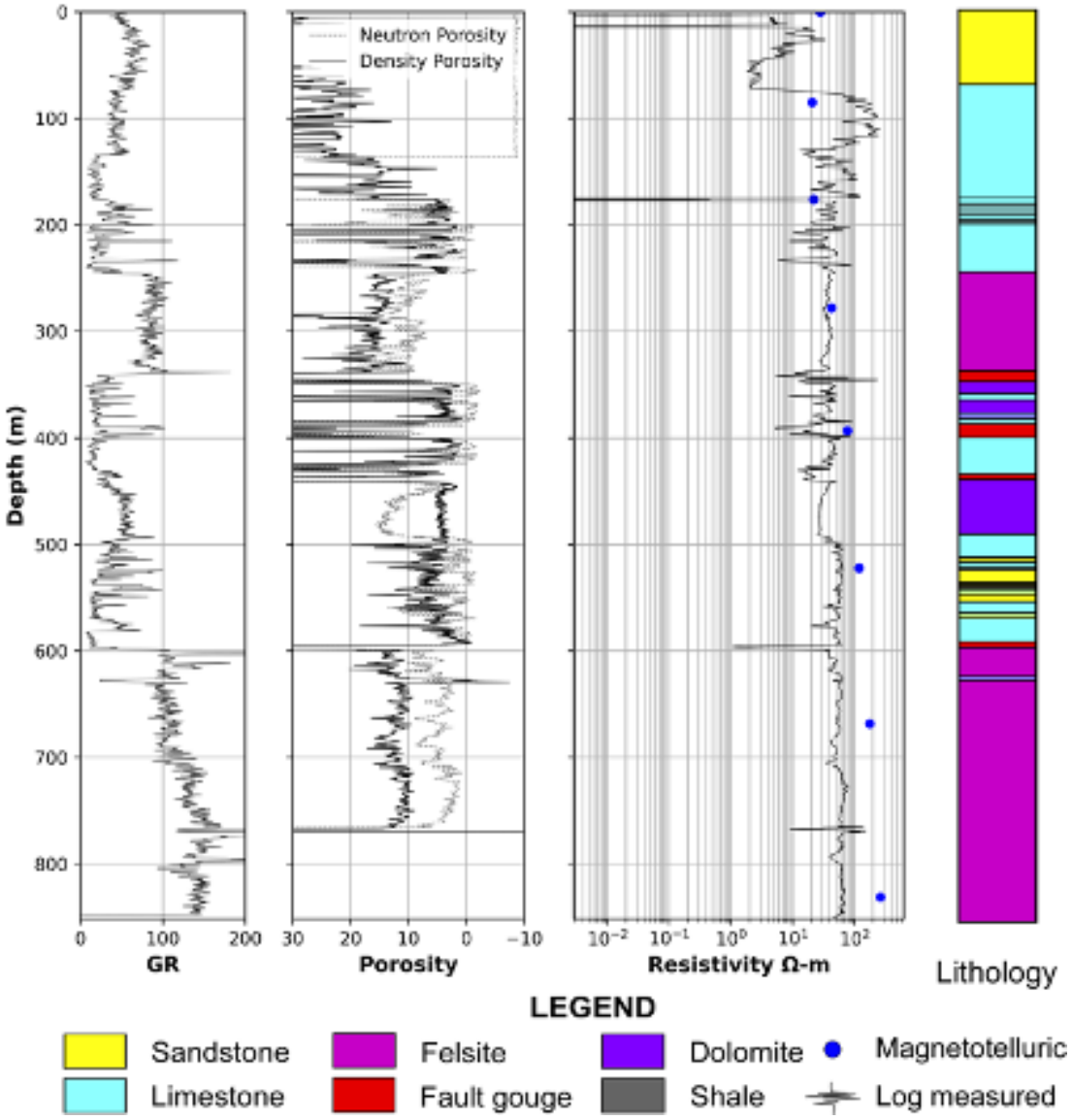

Fig. 2.12: Comparison of wireline logs, resistivity logs, and MT resistivity of well 56-5. The resistivity from well logs provides more detailed variations in resistivity that are not detected from lower resolution, inverted MT resistivity data. Lithologies are based on petrophysical interpretations from accompanying gamma ray (GR), neutron and density porosity, photoelectric effect (PE), deep resistivity logs, and core cutting descriptions.

Lithologic interpretations from MT inversions are difficult since resistivity is primarily influenced by the salinity of pore-filling fluid and secondarily by porosity[59]. Because all rock matrices are potentially saturated with similar saline water, porosity controls resistivity variations. In general, lithification increases with depth and is associated with a decrease in porosity and permeability consistent with the observed increase in MT resistivity from L1 to L3 (Fig. 2.11)[67]. Correlations between the four cored wells in the northeast portion of the study area indicate that L1 coincides with Quaternary basin fill that is under-compacted and highly porous and permeable and, therefore, characterized by low resistivity. Older strata associated with L2 and L3 are highly compacted and cemented and characterized by lower porosity and permeability and higher resistivity. The transition from L2 to L3 is controlled by porosity rather than lithology. For example, as seen in EW2, L2 thickness increases to the west, suggesting an increase in porosity. The phase tensors in the west show 2D resistivity structures with increasing depth suggestive of a possible fault system (Fig. 2.11). Secondary pore networks derived from fluid-rock interactions induced by the high permeability fault system are interpreted to be filled with high salinity and low resistivity fluids. Also, cored wells 61-6, 45-5, 46-6, 56-6, and 51-5 indicate that L2 and L3 coincide with Paleozoic bedrock composed primarily of resistive carbonates. The resolution limitations of MT resistivity measurements mean that small-scale changes in carbonate lithologies are not detected and suggest that differences between L2 and L3 are not related to lithology (Fig. 2.12).

Conclusions

NMF*k* is a useful ML tool to assess prospective geothermal regions by evaluating variability in geothermal, geological, geophysical, and geochemical attributes. In the southwestern portion of the Tularosa Basin at White Sands Missile Range, four signatures (A-D) were established through NMF*k* for their geothermal resource potential. Signature A is interpreted to have the highest geothermal potential due to a combination of high heat flow, reservoir temperatures, and comparatively high porosity and permeability. Signatures B and D have moderate potential because of their relatively low heat flow and temperature. Signature C has the lowest geothermal resource potential because no geothermal attributes have a major contribution to the signature.

MT inversions detect subsurface geothermal prospects based on resistivity. MT provides insight into relative porosity and associated permeability that is related to the subsurface resistivity trends detected in the MT inversion. From an MT survey from McGregor Range, three resistivity layers (L1, L2, and L3) and 2 resistivity structures (RS1 and RS2) are identified. The layers are inferred to be related to a combination of depth-related compaction and lithification effects, and the resistivity structures are related to Davis Dome, laccolith, and faulting. A fault system is interpreted in the western portion of the study area as indicated by the thickening of L2. Because low resistivity is a defining characteristic of geothermal prospects, the western portion of the McGregor MT survey has the highest geothermal potential.

The low vertical resolution of MT data, in contrast with high-resolution borehole resistivity measurements, makes it difficult to relate lithological variability and associated rock attributes with MT inversions. MT is limited because the interpreted resistivity layers only provide insight into relative porosity and do not correlate with lithological or stratigraphic units. Only large-scale characterization of porosity and associated permeability can be made when interpreting MT inversions. Therefore, the MT survey may be used as a preliminary study before drilling a well, which will provide more detailed information for developing a geothermal field.

Chapter 3: Characterization of Potential Geothermal Energy Utilization in West Texas

Introduction

The total U.S. energy consumption is ~13.68×10^9 GJ[48], mostly from fossil fuels that emit carbon into the atmosphere. To reduce CO_2 emissions, carbon-free energy sources such as wind, solar, and geothermal are becoming more prevalent. Geothermal energy is poised to become an important continuous source of heat and energy. Currently, geothermal energy makes up <1% of U.S. electricity generation but can increase dramatically as the U.S. has ~2×10^{14} GJ of extractable geothermal energy[48].

Large areas of land in the U.S. with a high geothermal gradient may possess hot water resources. Most importantly, many oil and gas fields have high thermal gradients that can be converted into geothermal energy. As geothermal energy use becomes more prevalent, it is important to easily determine the proper setting and attributes to displace the greatest amount of fossil fuels. Therefore, the main purpose of this work is to estimate geothermal prospectivities and commercial feasibility in western Texas (Fig. 3.1) using publicly available oil and gas field data.

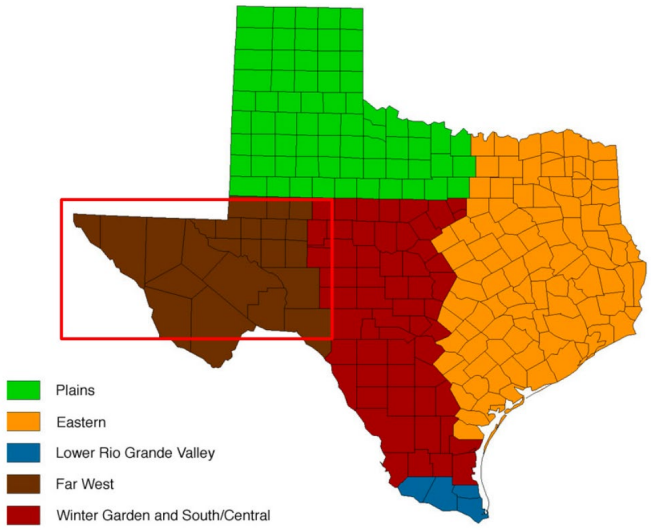

Fig. 3.1: The map of Texas, including their basin configuration. The study area is in west Texas, bounded by the red rectangle.

Western Texas because it not only has a high number of existing and orphaned oil fields/wells but also has a medium geothermal gradient and easy-to-drill sedimentary formations. These existing or abandoned oil wells are a great opportunity for geothermal energy as their interconnected piping infrastructure and drilled wells can be repurposed for geothermal energy production, reducing a large portion of the costs associated with geothermal development. Medium geothermal gradient and soft sedimentary formations favor drilling new wells if necessary. Additionally, geothermal resources in the form of water and other heated fluids can be found along with oil and gas.

We mainly used three geothermal attributes including thermal conductivity, heat flow, geothermal gradient, and bottom hole temperatures (BHT). Next, preprocessing was performed to remove spurious data. Next, we interpolated using the inverse distance weighting (IDW) technique to estimate values at unknown locations based on known locations. Next, we delineated the proper utilization of this geothermal energy for electricity production, spas & balneology, and greenhouse farming based on their temperatures at 1, 2, 3, and 4 km depths.

Three variables used in this study contained about 48% outliers. For instance, the maximum and minimum values for the temperature gradient far exceeded the appropriate range of the geothermal gradient throughout the U.S. Whereas the average geothermal gradient range in western Texas is contoured between 15 – 40°C/km, the provided data ranged between 0 - 1386°C/km[72]. We removed these outliers from the data by creating a new dataset that only included values that were greater than or equal to 15°C/km or less than or equal to 40°C/km. Additional outliers existed within the heat flow data set, so we instead opted to use the following formula to calculate new data for the heat flow throughout the West Texas region:

$$q = K_T \nabla T \tag{3.1}$$

where q is heat flow (W/m^2), K_T is thermal conductivity (W/mC), and ∇T is temperature gradient (C/m). To obtain accurate heat flow data, we located the thermal conductivity points either in the same location or closest to those in the new geothermal gradient dataset. To do so, we conducted a nearest neighbor calculation using a binary search tree or K-D tree to determine the shortest Euclidean distance between points based on the longitude and latitude data. The data provided by this calculation allowed us to extract only the points in thermal conductivity data that geospatially coincided with the new geothermal gradient dataset. Next, we performed the IDW described in the method section of Chapter 1.

Utilization Scheme

Each industry has a unique temperature requirement to continue its business. For spas, a comfortable inlet water temperature is around 40 °C with 50 °C. While current spas can use water temperatures above 50 °C, this water requires additional cooling to achieve a safe temperature. Following Germany's example, the maximum allowed inlet water temperature was 60 °C.

The temperature required for heating systems in greenhouses ranges from 40 – 100 °C, as greenhouses can use various heating systems. These greenhouses can utilize this geothermal energy through finned pipes, fan coil units, soil heating, plastic tubing, cascading, bare pipes, unit heaters, or a combination. The heating method used in these greenhouses will determine the inlet temperature for the water.

There are three major types of geothermal power plants, dry steam, flash steam, and binary (Table 3.1). A dry steam power plant primarily uses steam extracted directly from the geothermal reservoir. Flash steam is the most common type of power generation plant in operation today but required temperatures greater than 150°C. The power plant with the greatest potential for geothermal utilization is the binary cycle power plant. This plant differs by heating a secondary fluid through a heat exchanger. The benefit here is that binary cycle power plants can use low-enthalpy fluids with temperatures ranging from 95 - 150°C.

Table 3.1: Geothermal power plant types, corresponding fluid types and temperature ranges.

Geothermal power plant type	Fluid type	Temperature range (°C)
Dry steam	Steam	>150
Flash steam	Water	>150
Binary	Organic	95-150

Results and Discussion

We received numerous attributes from the Bureau of Economic Geology, UT Austin. Among those attributes, only bottomhole temperature, geothermal gradient, thermal conductivity, and heat flow possess good quality data (Fig. 3.2). Continuous interpolated contour at 1 km depth of each attribute is shown in Fig. 3.2a-c.

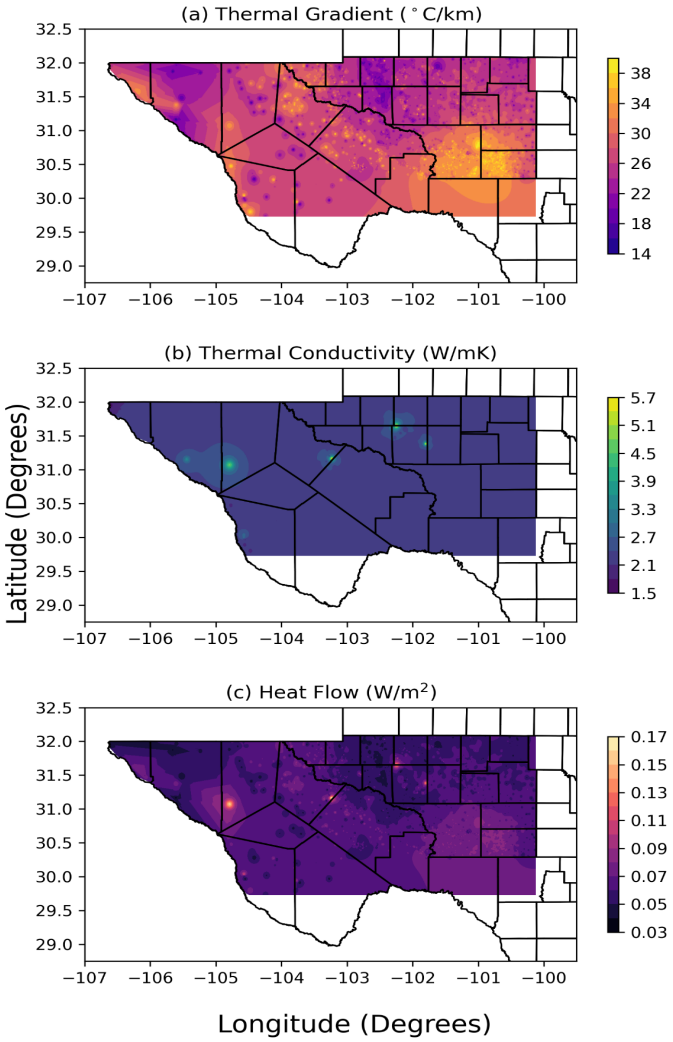

Fig. 3.2: Contours of geothermal gradient (a), thermal conductivity (b), and heat flow (c).

Thermal gradient is the change in temperature per unit depth and is vital in determining temperatures at specified depths. The geothermal gradient in the study area had much greater variation in values than the other attributes and averaged 27.5°C/km with a maximum of 39.5°C/km and a minimum of 15.3°C/km (Fig. 3.2a). The average of 27.5°C/km is only 5.3% below the average gradient for the continental U.S. However, when compared to western states, the West Texas geothermal gradient was 21.14% below the 34°C/km value.

The thermal conductivity throughout the majority of the West Texas region lies at approximately 2.5 W/mK with spikes in conductivity up to 5.44 W/mK towards the western edge and throughout the center of the region (Fig. 3.2b). Thermal conductivity describes a material's ability to transfer heat through conduction. For a geothermal resource, thermal conductivity is critical to understand as it directly controls the steady state temperature field[73]. Additionally, it can have a large impact on required bore hole depth to meet the heating demands of a utility when utilizing a ground-source heat pump or ground coupled heat exchanger.

Heat flow in a geothermal context is the movement of heat/energy from the interior of the Earth to the surface. A larger heat flow is typically indicative of good geothermal heat production. Additionally, heat flow determines vertical conductive heat flow losses as geothermal fluids rise to the surface either naturally or through piping. Throughout the West Texas Region heat flow averages around 0.0637 W/m^2, with a few spikes up to 0.1635 W/m^2 (Fig. 3.2c).

To determine the borehole temperatures at depths between 1 km and 4 km with 1 km incremental depth, the geothermal gradient dataset was multiplied by the chosen depth and added to the standard surface temperature of 25°C. Utilities were then added to their corresponding temperature ranges on the plots to highlight the potential forms of utilization and their pervasiveness throughout the region (Figs. 3.3–3.6). Bottom hole temperature rises following geothermal gradients, ranging from a minimum of 40°C at 1 km to a maximum of 178°C at 4 km, hence the utilization (Table 2).

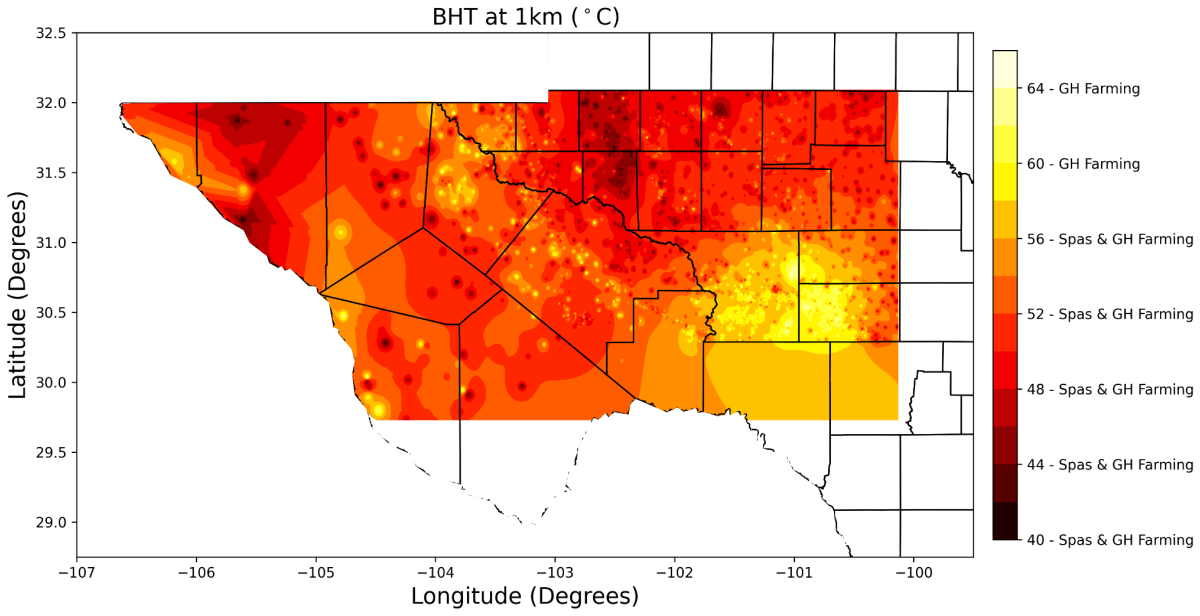

Fig. 3.3: Spas could be a favorable utility at 1 km depth.

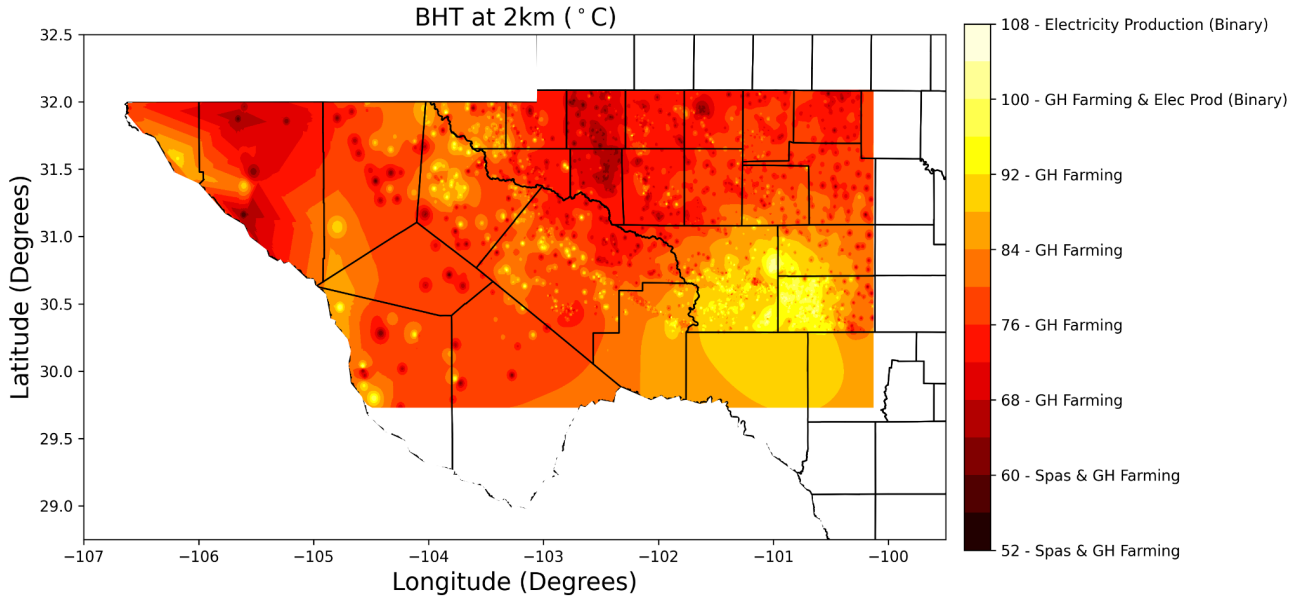

Fig. 3.4: Green house farming could be a favorable utility at 2 km depth.

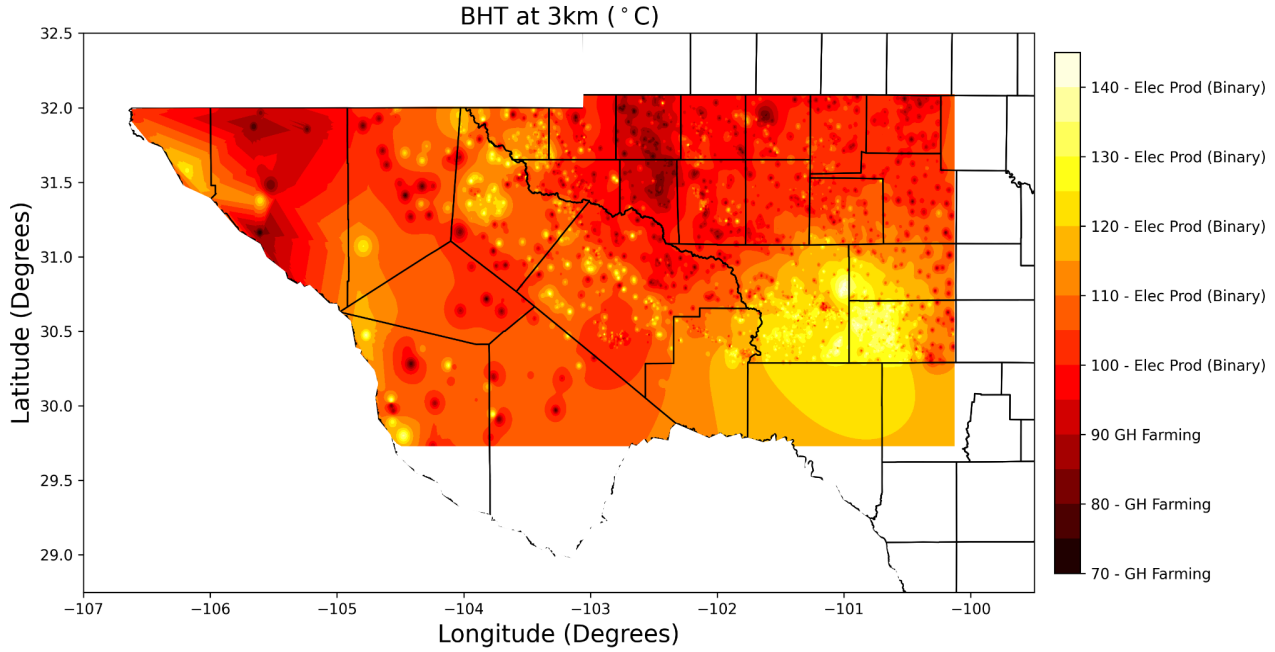

Fig. 3.5: Electricity production through binary geothermal power plant could be a favorable utility at 3 km depth.

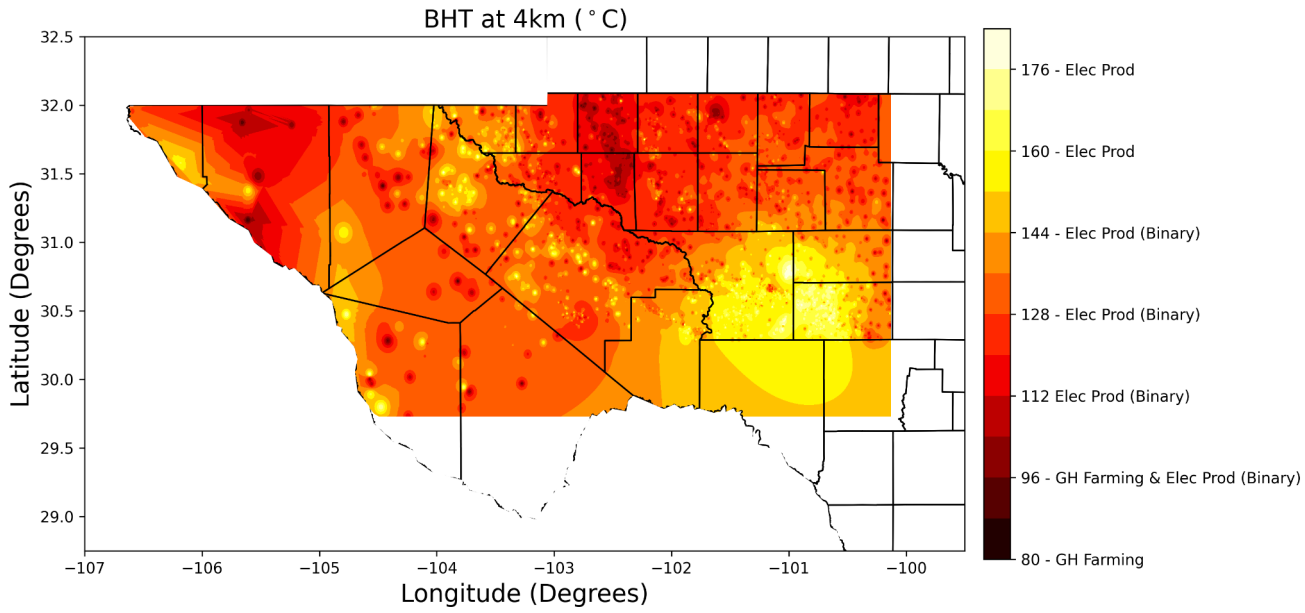

Fig. 3.6: Electricity production through binary & steam flash geothermal power plant could be a favorable utility at 4 km depth.

Table 3.2. Summary of potential utilities for 1 - 4 km depth.

Utility	1km	2km	3km	4km
Spas & GH Farming	98.94%	0.10%	N/A	N/A
GH Farming	1.06%	98.84%	6.8%	0.10%
GH Farming & Elec Prod (Binary)	N/A	0.93%	10.97%	0.21%
Elec Prod (Binary)	N/A	0.12%	82.24%	85.37%
Elec Production	N/A	N/A	N/A	14.32%

It is important to note that Table 3.2 is reflective of only the data points created from the interpolated datasets and not the actual geospatial locations. As displayed above, at 1km, spas and greenhouse farming could be the dominant utility encompassing 98.94% of the West Texas geothermal resources. However, beyond 1 km, the temperature becomes too high to support safe and efficient geothermal spas, so spas are essentially infeasible. At 2 km, the greenhouse farming utility dominates 98.84% of the potential available utilities. Since the average depth of crude oil and natural gas wells is approximately 2 km, geothermal greenhouse farming operations become the most potentially viable utilities if they are able to take advantage of the existing infrastructure. Additionally, 2 km is where it can be seen that some binary electricity production can begin to occur. At 3 and 4 km, binary electricity production becomes the dominant utility with some potential for greenhouse farming. The flash steam power plant is only feasible at or beyond 4 km. While BHT at 4 km is still considered reasonable, it is quite costly to drill that deep. If electric

utility companies are willing to spend higher upfront costs, there is a large potential for the expansion of flash steam cycle energy production.

We also plotted orphan wells on top of the BHT map at 2km (Fig. 3.7). Many of the wells are located on top of geothermal resources that could be used for greenhouse farming, with some located on resources that could be used to produce electricity from a binary cycle power plant (Fig. 3.7). These orphan wells might be a good avenue to reduce upfront cost to set up utility facilities.

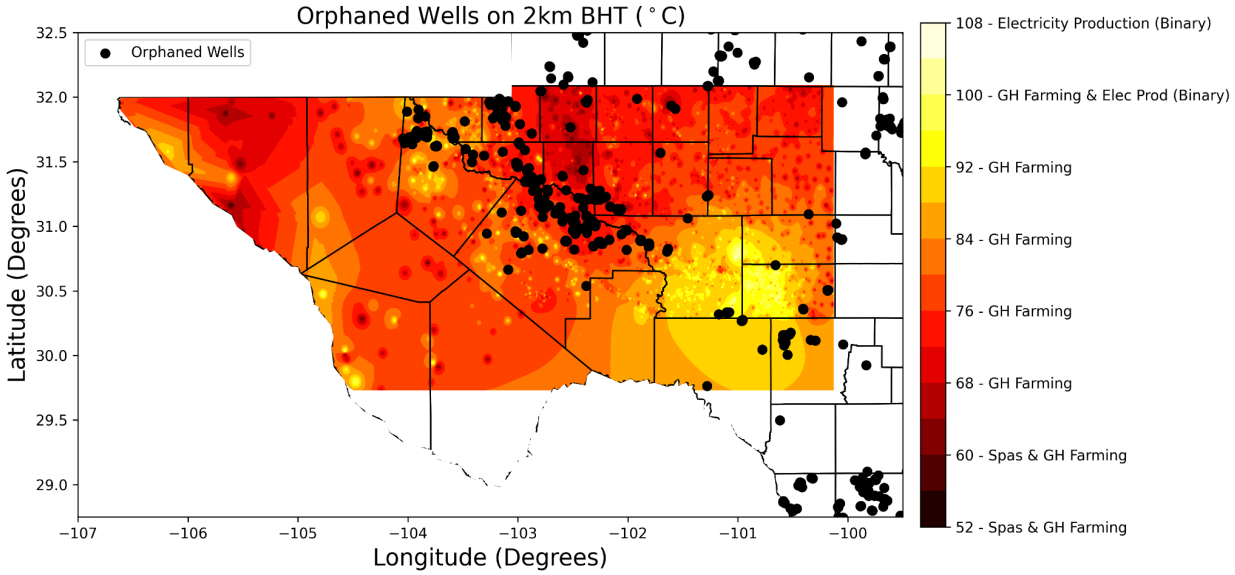

Fig 3.7: Orphan wells could be used to extract hot fluid, however, a detail study is required on whether they can sustain thousands of barrel fluid withdrawal in a day.

Conclusions

West Texas has a huge potential for certain geothermal utilization facilities ranging from spas to electricity production that varies with depth. For instance, at 1 km depth, geothermal spas could be a favorable utility while greenhouse farming can be expected to make great use of not only the geothermal resources but also the existing oil and gas infrastructure at 2 km depth. At 3 & 4 km, binary cycle power plants would predominantly use the geothermal resource to produce clean and continuous electricity. At a depth of 4 km, a steam-flash power plant could be used to generate electricity, although spatially sporadically. Orphan wells can be used to reduce cost; however, a thorough study is required to determine if they can sustain 1000 barrels of fluid extraction in a day.

Chapter 4: Machine Learning and a Process Model to Better Characterize Hidden Geothermal Resources in Tularosa Basin

Introduction

Geothermal is a growing renewable energy resource that can be utilized 24 hours a day without shutting off a geothermal power plant. However, in the U.S. ~3.7 GJ/year (<1%) of electricity generation is from geothermal resources[48] although it has ~2 x 10^{14} GJ/year tappable energy[50,74]. This potential energy resource is largely unexplored because many geothermal reservoirs are hidden or blind (no apparent surface exposures), which often leads to expensive and risky exploration[75,76]. Typically, play fairway analysis (PFA), adapted from the oil and gas industry, is performed for geothermal discovery, exploration, and development. PFA integrates available geologic, geophysical, and geochemical attributes indicative of geothermal activity and estimates the importance of these attributes for the characterization of the geothermal resource[77–82]. PFA separately quantifies the relative importance of each attribute instead of the simultaneous usage of all attributes. Here, we used a tool called GTC, which simultaneously analyzes available attributes, finds geothermal prospectivities, and discovers key parameters defining geothermal prospectivities[1,37].

GTC utilizes different machine learning (ML) methods. GTC can (1) analyze large field datasets, (2) assimilate model simulations (large inputs and outputs), (3) process sparse datasets, (4) perform transfer learning (between sites with different exploratory levels), (5) extract hidden geothermal signatures in the field and simulation data, (6) label geothermal resources and processes, (7) identify high-value data acquisition targets, and (8) guide geothermal exploration and production by selecting optimal exploration, production, and drilling strategies. Although GTC can implement different ML methods, its core component is an unsupervised machine learning (ML) called non-negative matrix factorization with customized *k*-means clustering (NMF*k*)[1,16,25,54]. Here, we applied NMFk to the Tularosa Basin PFA dataset collected by the Department of Energy (DOE).

The Tularosa Basin is located in the Basin and Range province, which exhibits high favorability of occurrence for geothermal resources due to high heat flow related to the Rio Grande rift. A few geothermal facilities have been developed within the Basin and Range province[83,84]. Recently, it has been the subject of geothermal studies due to its high geothermal potential coupled with the U.S. Army's interest in using the geothermal resource as an energy source for White Sands Missile Test Range and McGregor Range[58,60,61].

Geologically, the Tularosa Basin is located on the eastern flank of the Rio Grande rift zone as a north-trending, intermontane graben located in south-central New Mexico. It is bounded to the east by the uplifted Sacramento Mountains and to the west by the uplifted Organ and San Andreas Mountains. Faults related to the Rio Grande rift with several thousand feet of displacement separate the basin from the surrounding, uplifted mountains. Stratigraphically, the Tularosa Basin consists of Paleozoic limestones and shales to Tertiary age rocks[58,60–62]. Rifting during the Paleogene resulted in characteristically high heat flow in south-central New Mexico[85,86]. High heat flow makes the southern part of the Tularosa Basin favorable for geothermal exploration.

Recently, the DOE has collected data to develop geothermal fields in the Tularosa Basin. The data include geological, geophysical, geothermal, and geochemical attributes. Also, a comprehensive PFA study was conducted by Ruby Mountain Inc.[39,86], and they demonstrated prospective geothermal locations. In this study, we curated data from the DOE Geothermal Data Repository and then used them as input parameters for GTC. Results from GTC provide insights into the relationship between attributes and prospective geothermal locations, which we then compared to the PFA study by Ruby Mountain Inc.. Lastly, we discussed how NMFk and Burns' equation[34] can be coupled to obtain a better understanding of prospective geothermal sites.

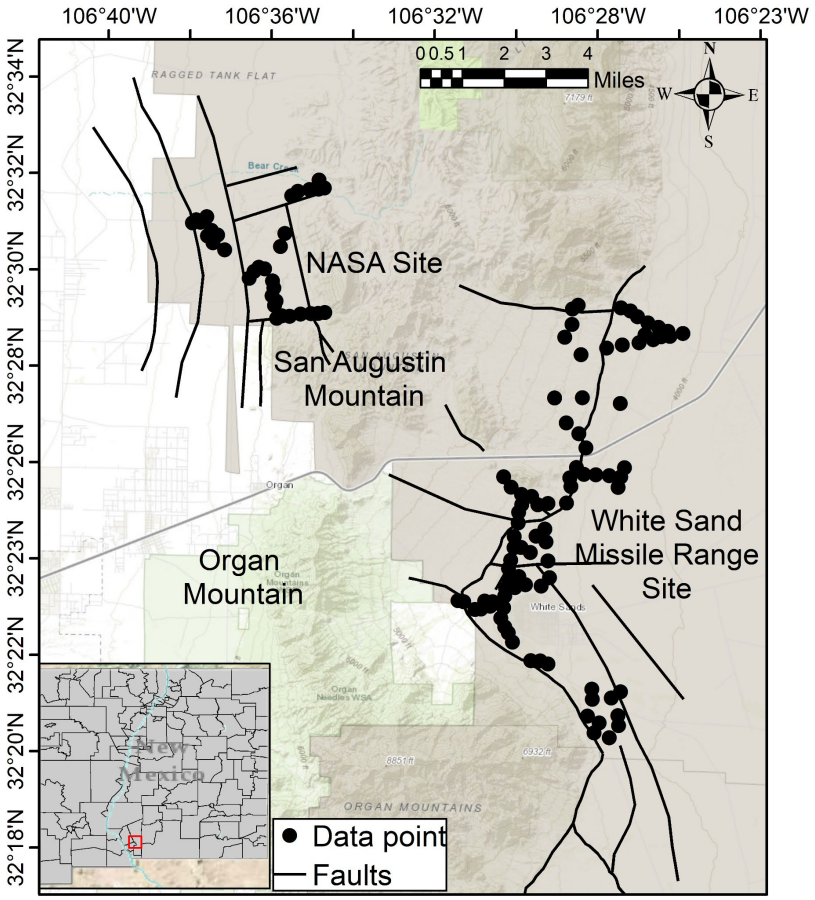

Fig. 4.1: Data locations and Quaternary faults in the study area.

Data

In this study, we used a total of 10 attributes: temperature at 2m depth (temperature at 2m), heatflow, NaK-Giggenbach geothermometer, K-Mg geothermometer, NaK-Fourneir geothermometer, silica geothermometer, gravity, fault distance, quaternary fault density, and Li concentration. All these attributes are critical for geothermal resources discovery and exploration. Temperature at 2 m has been used to explore geothermal fields at Dead Horse Wells, the Hawthorne Army Depot, and Emerson Passin in Nevada[87]. Heatflow defines how heat flows to the geothermal reservoir from the deep subsurface. Geothermometers (NaK-Giggenbach geothermometer, K-Mg geothermometer, NaK-Fourneir geothermometer, and silica

geothermometer) are used to estimate potential reservoir temperature and geochemical processes in the reservoir. These geothermometers help estimate potential reservoir temperature, leading to less exploratory well drilling. Gravity may represent secondary mineralization and help characterize geologic structure[88]. Faults can act as conduits of (1) groundwater flow water from depth to the ground surface as well as (2) groundwater recharge. We have two fault attributes: fault distance and quaternary fault density. Fault distance represents the distance from the fault to the data point. Fault density (quaternary) is the number of faults per square meter of an area. Finally, Li concentration is a geochemical element that represents deep fluid circulation. All these attributes were used at 120 locations (Fig. 4.1)

However, all attributes are dispersely located and are not available at 120 locations except temperature at 2 m. We applied different interpolation techniques to sample all attributes at the specified 120 locations. For heatflow, NaK-Giggenbach geothermometer, K-Mg geothermometer, NaK-Fourneir geothermometer, silica geothermometer, gravity, and Li concentration interpolation was used by making the study area as a grid. Interpolation was performed based on block mean, kriging, and inverse distance weighting. Next, R^2 score was computed based on interpolated values and real values. We found all methods provide equivalent R^2 scores. Block mean was selected as the optimal interpolation method because it takes the least time to execute. The interpolated values were used in the nearest neighbor algorithm to sample 120 values at 120 locations. The nearest neighbor algorithm finds a mean value based on the radius or the number of points around a point. Here, we use radius to find the mean value. The radius was calculated based on a variogram study of the data.

Fault distance and fault density were estimated using different approaches. For estimating fault distance, we generated a normal raster on ArcMap. The raster was converted to points. Next, a near coverage tool on ArcMap was used to compute the distance of each point from the nearest faults. For estimating fault density, we also generated a normal raster followed by converting points. Next, the near coverage tool was used to find the distance from a point to the nearest faults. Finally, the kernel density function was used to calculate fault density. The unit of fault density is m/m^2.

To develop a neural network-based ML model, we generated data based on Eastern Snake River Plain by varying input parameter ranges based on variance and mean of data using Eqn. 6. Next, we form a 1D deep neural network with three layers. Each layer has 256, 128, and 64 layers, respectively. We used relu as the activation function. We trained the model for 500 epochs with a learning rate of 0.001. Using a data matrix instead of generating files is the main benefit of utilizing the neural network model. Also, point-based prediction is feasible with the neural network-based model but is not possible with Burns' equation.

Results

Fig. 4.2 shows the reconstruction quality $O(k)$ and average silhouette width $S(k)$ for different numbers of geothermal signatures k. $O(k)$ values exponentially decrease with the increase of the number of signatures. However, that is not generally true $S(k)$. Although optimal solutions have low $O(k)$ and high $S(k)$values, their optimal values are not theoretically established. Generally, low $O(k)$ and $S(k)$>0.25 can be considered to be acceptable. Here, the solutions for k=2, 3, 4, 5, and 6 were accepted, while the k=8 to 10 solutions were rejected by the algorithm. This conclusion

is based on the high $S(k)$values (>0.25) and the $O(k)$ decline curve (Fig. 4.2). The k=4 solution is found to be optimal because of its low $O(k)$ and high $S(k)$ values. The solution with k<4 is an underfitting representation of data, while k>3 is an overfitting data representation. In the following paragraphs, we will describe each signature of the k=4 solution (Fig. 4.3).

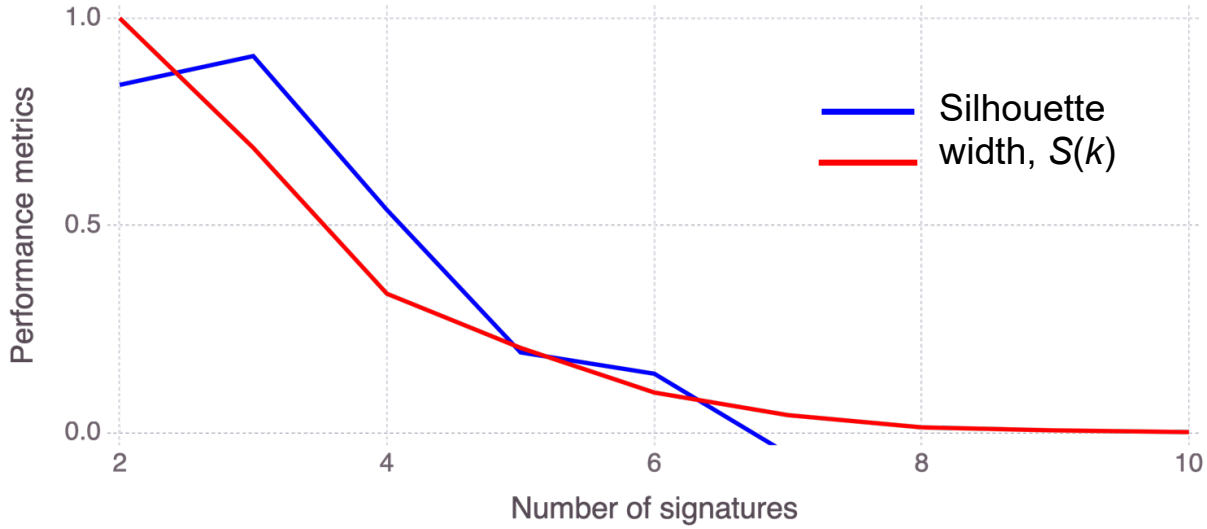

Fig. 4.2: NMFk results for normalized reconstruction quality/fit $O(k)$in red color and solution robustness (based on the average silhouette $S(k)$ width of the clusters) in blue color for different numbers of signals k.

Fig. 3 shows a heatmap of signatures found by GTC. Each signature captures certain characteristics in the dataset. The colors in each signature represent the contribution of each attribute. Green, yellow, and brown-red colors represent minor, moderate, and major contributions. The minor and major contributions also mean the dataset's low and high attribute values.

The dominant attributes of Signature A are heat flow, K-Mg geothermometer, silica geothermometer, and quaternary fault density (Fig. 3a). Heat flow is one of the main geothermal attributes while K-Mg and silica geothermometers potentially represent high reservoir temperature. Low contribution from NaK-Giggenbach and NaK-Fourneir geothermometers suggests that geochemical processes in the reservoir are not controlled by Na enriched minerals. High contribution of quaternary fault density may indicate elevated secondary permeability. The contribution of Temperature at 2 m is medium that is consistent with high heat flow. Another critical component of this signature is low contribution from fault distance. Low fault distance means fault is close to the locations associated with this signature that may lead to elevated secondary permeability. All these factors are good indicators for high geothermal prospects; therefore, the locations associated with Signature A have a high chance of having geothermal resources (Fig. 3b).

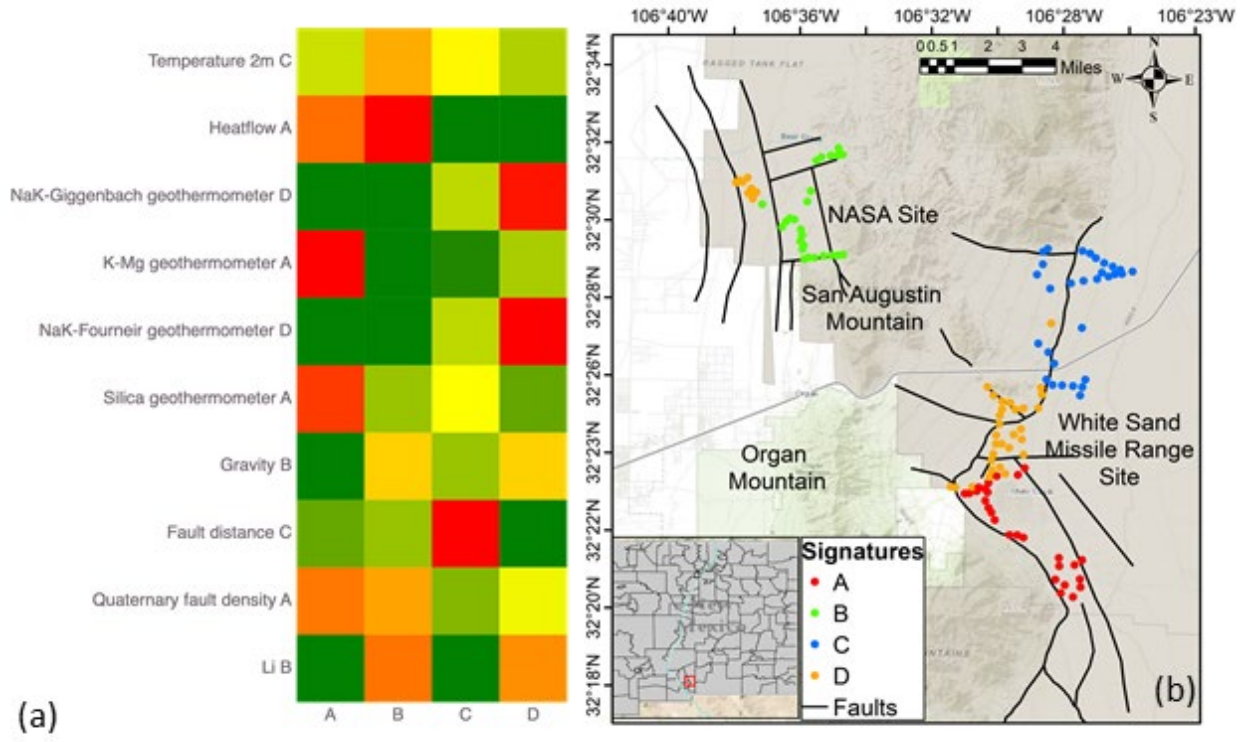

Fig. 4.3: Geothermal signature heatmap (a) and their spatial distribution (b). Each signature captures certain characteristics in the data. Here, Signatures A and B represent highly prospective geothermal signatures. Green, golden, and red colors in (a) represent low, medium, and high contributions, respectively.

The dominant attributes of Signature B are Temperature 2 m and heat flow, quaternary fault density, and Li concentration (Fig. 3a). Temperature 2 m and heat flow are two main geothermal attributes. The high contribution of quaternary fault density may indicate elevated secondary permeability. The high contribution from Li suggests a potential fluid circulation from the deep subsurface that is a good indicator of potential geothermal resources. The contribution from fault distance is also low. Low fault distance means faults are close to the locations associated with this signature. All these factors are good indicators for high geothermal prospects; therefore, the locations associated with Signature B have a high chance of potential geothermal resources (Fig. 3b). However, no geothermometers had major contributions on this signature except close to medium contribution from silica geothermometer suggesting the geothermal potential is not as high as Signature A. a careful approach should be taken prior to making any decision about geothermal resource development.

No geothermal attributes had a major contribution on Signature C; therefore, we conclude that the locations associated with it have a low chance of possessing geothermal resources. In Signature D, the dominant attributes are NaK-Giggenbach and NaK-Fourneir geothermometers. These attributes suggest that the reservoir has a high temperature. The medium and high contribution of Quaternary fault density and Li concentration suggest elevated secondary permeability and deep fluid circulation. However, temperature 2 m and heat flow had low contributions. All these factors suggest that the locations associated with Signature D (Fig. 3b) may or may not have high

prospectivity. However, Signature D has some positive characteristics for exploring geothermal resources and because of its proximity to Signature A (high prospective signature), there is some potential for sustainable geothermal resources in the locations associated with Signature A. Note that the prospective geothermal locations are consistent with the Ruby Mountain's PFA prospective locations.

NMFk results help us discover potential geothermal resources and their spatial locations. Regional hydrogeological and geothermal conditions would facilitate a better understanding on whether we can develop a long-term geothermal facility here. To obtain such results, we can apply Eq. (3) to compute aquifer temperature, viscous heat flux, vadose heat flux, and advective heat flux. Among these four attributes, viscous heat flux and advective heat flux could be used to estimate the potential time to heat up the geothermal reservoir temperature during energy production and injection, hence, the viability and sustainability of geothermal reservoirs. We coupled the Burns' equation with NMFk, and GTC can perform such tasks. However, we could not demonstrate a study because of a lack of data. We will conduct and demonstrate such a study if we receive a good dataset in the future.

Conclusions

Tularosa basin has potential geothermal resources, which can be used to support several federal facilities in the area. To find geothermal prospects, we studied 10 attributes at 120 locations. Attributes include temperature 2 m, heatflow, NaK-Giggenbach geothermometer, K-Mg geothermometer, NaK-Fourneir geothermometer, silica geothermometer, gravity, fault distance, quaternary fault density, and Li concentration. The dataset was used as input parameters to GTC. GTC finds four signatures (A, B, C, and D), two of which are geothermal signatures. The locations associated with Signatures A and B have high geothermal resource prospectivities that are spatially consistent with the Ruby Mountain's PFA study. We also found that the locations associated with Signature D are not as prospective as Signatures A and B, but they might assist a sustainable geothermal reservoir in the area around the locations of Signature A. The key attributes defining the geothermal resources are heat flow, K-Mg geothermometer, silica geothermometer, quaternary fault density, temperature 2 m, fault density, and Li concentration. Finally, we discussed how we can couple an existing analytical equation to GTC computing the viability and sustainability of geothermal reservoirs.

Chapter 5: A FORGE Datathon Case Study to Optimize Well Spacing and Flow Rate for Power Generation

Introduction

Enhanced geothermal systems (EGS) present a significant and long-term opportunity for widespread power production and direct heat[76,89]. However, high exploration costs and uncertainties associated with subsurface characteristics (such as permeability, reservoir temperature, fault connectivity, geochemistry, and in situ stress distribution) have impeded the geothermal market growth[76,89]. Moreover, building a profitable EGS is a major challenge. Profitable EGS fields will depend on many design parameters[3,4]. We will focus on the parameters of reservoir depth, project lifespan, injection temperature, well spacing, well length, well azimuth, well depth, well skew (i.e., non-parallel wells), well count, well toe (i.e., decreasing well spacing from heel to toe), well proportion (i.e., the ratio of injection well length to production well length), well phase (i.e., the placement of the production well above, beside, or below the injection well), well intervals (i.e., the number of isolated perforation clusters), production well pressure drawdown, stimulation flow rate, stimulation volume, and circulation flow rate. Finding optimal values for these design parameters is a computationally expensive task to say the least.

To tackle this challenge, PIVOT organized a first-ever Geo Datathon event in 2022[90]. The primary goal of this Datathon was to identify production well placement. Participants in this event used different machine-learning methods to solve a geothermal engineering problem on a simulated dataset of the Utah FORGE site (Fig. 5.1). Data for the Datathon was generated by the geothermal design tool (GeoDT) to investigate the power production potential of an EGS system. Six teams (Team Naturals, Benjamin Cassidy, Pebbles, GeoT360, S-Team, and GeotherML) completed the competition in this event. Team Naturals of Stanford University, Benjamin Cassidy of Hammer and Tongs Polymer Development, and Pebbles of the Colorado School of Mine were awarded champion, 1st runner up, and 2nd runner up, respectively.

Despite a short time for the competition and a challenging task, each team made a great contribution to identifying suitable locations for the production well. Team Naturals included metrics for risk by considering averages and standard deviations in power production. Also, they clearly demonstrated that net power production was not the best value to optimize. Benjamin Cassidy applied a unique set of approaches to the ML challenge to optimize well placement from more than one perspective. Crucially, these competitors also revealed several problems that needed to be solved to get the best answer to optimizing the well spacing: (1) identifying a suitable objective function (e.g., net present value), (2) finding a robust optimization method for the complex dataset, and (3) accounting for uncertainty and risk tolerance.

Here, the primary purpose of our study is to find optimal well spacing (w_spacing) and per-interval circulation flow rate (Qinj) for the same dataset. First, we define a new objective function, which yields reduced parameters for comparing realizations, e.g., average power or net present value (NPV) in dollar amount. We chose NPV because it provides the best estimate of monetary value. Second, we developed a binning-based optimization approach. Third, we identified optimized w_spacing and Qinj with an assessment of uncertainty.

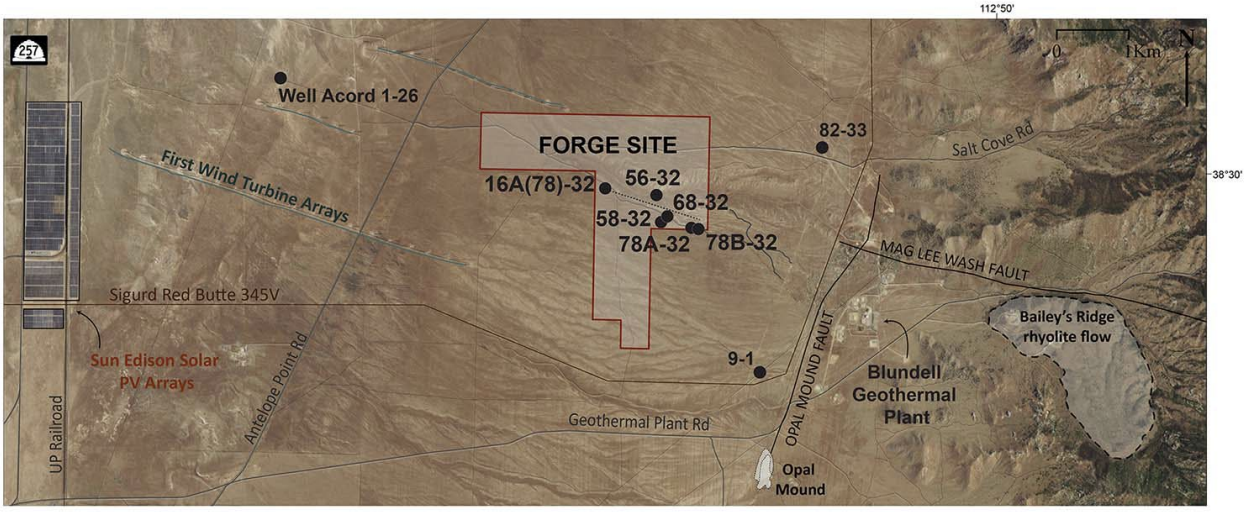

Fig. 5.1: Utah FORGE site with the injection well 16A(78)-32 and five monitoring wells (taken from Moore et al. 2021[91]).

Net Present Value (NPV) Estimation

Our new economic module in GeoDT yields estimated NPV in circa 2019 U.S. dollar amounts for a hot dry rock EGS geothermal project[92]. Such a reduced value is critical for optimizing geothermal design parameters. This module considers capital costs, maintenance costs, pumping costs, and power sales. Following the theme of fast-simplified physics, this module uses simplified methods to estimate costs where the underlying goal is to give a conservative view of the economic potential of a project. The cost terms that we employ in this study are summarized in Table 5.1. True costs for an EGS site depend on many factors beyond what our simple model includes. Ultimately, we use this cost model as an objective function to better contrast increasing power production with increasing capital costs and other financial risks.

Table 5.1: Constants used to estimate NPV.

Parameter	Unit	Value	Reference
Electricity sales per kilowatt-hour	USD/kWh	0.1372	EIA, 2022
Drilling cost per length	USD/m	2763	Lowry et al., 2017
Drill pad cost	kUSD	590	Lowry et al., 2017
Power plant cost	USD	2026	GETEM
Exploration cost per depth	USD/m	2683	GETEM
Operating cost per kilowatt-hour	USD/kWh	0.0365	GETEM

Outputs from GeoDT that pair with these cost factors include the net power output (Pout) for each model timestep and timestep parameters (TimeSteps and LifeSpan). The net power production term (Pout) for the Datathon only included the flash steam cycle for power generation. In this study, we add a simplified estimate for isobutane binary-cycle power generation and an improved estimate of injection well pumping losses that account for open-loop fluid losses (https://github.com/GeoDesignTool/GeoDT). Each power term includes the effect of inefficiencies, with this study using a conservative 85% efficiency (GenEfficiency). Discrete fracture networks with open-flow boundaries formed the basis of all the GeoDT models.

Data Description

The 16 most critical controllable design parameters (Table 2) can be divided into four categories: reservoir/site, power cycle, well, and stimulation. Of these, only 10 design parameters were varied to a meaningful degree because the first well at the site, well 16A(78)-32, has already been drilled at a diameter of 0.11 m to a depth of 2350 m with a highly deviated lateral length of 1114 in the direction of 1.833 radians Azimuth at a dip of 0.483 rad below the horizon. This azimuthal direction is near-parallel to the in-situ minimum horizontal stress direction. Reservoir depth is the only controllable reservoir parameter, but it is not a variable in this study because of the preceding reasons. Injection temperature was the only power cycle parameter that was varied because this study focuses on subsurface EGS design optimization, not power systems engineering. While GeoDT is capable of modeling hydraulic stimulation separately from circulation, in this study, the circulation stage is treated as a continuous stimulation stage for the lifespan of the EGS, so we did not parameterize these two stages independently. In other words, GeoDT predicts hydraulic fracturing and shearing at the same rate of injection as what is used for long-term circulation and heat mining. Our focus for design optimization will be set on well spacing (w_spacing) and per-interval circulation rate (Qinj) because these two terms were predicted to be first-order controls for power production.

Using statistical distributions for all the known and unknown sites, fracture network, and design parameters, 44,492 realizations were generated for the Datathon (PIVOT, 2022). All the well parameters were generated using uniform distributions. The minimum and maximum values of the distribution are listed in Table 5.2, and histograms of six example parameters are shown in Fig. 5.2. The lifespan of the field was considered only 30 years, and injection temperatures varied from 85-99°C (Fig. 5.3). The injection rates per-interval (Qinj), which also serve as the stimulation rates, were generated using exponential distribution because this offers improved resolution for realizations with low flow rates, relative to the maximum simulated flow rate. When the optimal flow rate is not known, the exponential distribution helps explore a larger probability space in order to more clearly identify the optimal flow rates.

Table 5.2: EGS project design parameters and corresponding units, minimum and maximum values, and their statistical distributions. Parameters in green color cells were optimized in this study.

Variable	Parameter	Unit	Min Value	Max Value	Distribution
ResDepth	Nominal reservoir depth	m	2340	2360	
LifeSpan	Project lifespan	yr	30	30	-
Tinj	Injection temperature	C	85	99	-
w spacing	Well spacing	m	50	1000	Uniform
w length	Well length	m	1114	1114	Lognormal
w azimuth	Well azimuth	deg	1.833	1.833	Uniform
w dip	Well dip	deg	0.438	0.438	Uniform
w skew	Well skew	deg	-10	10	Uniform
w count	Well count	wells	1	4	Uniform
w toe	Well toe	deg	-5	5	Uniform
w proportion	Well proportion	deg	0.8	1.1	Uniform
w phase	Well phase	deg	0	360	Uniform
w intervals	Well intervals	zones	1	6	Uniform
dPp	Production well pressure rise	MPa	-10	2	Uniform
perf	Perforation count	perfs	1	1	Uniform
Qinj	Circulation flow rate	m3/s	0.001	0.1	Exponential

Methods

In any optimization technique, identifying a suitable objection function is a crucial first step. Here, our goal is to maximize the NPV value of a geothermal project because NPV provides a common framework to measure the relative benefit and cost of each design decision. This contrasts with optimizing power production, where the most productive scenarios can be unreasonably expensive with respect to drilling and pumping costs. The traditional parameter estimation study fits a physical model to data, finding optimal parameters. Such a study finds a single optimal value for each parameter and then the Markov chain Monte Carlo (MCMC) method or its variant is performed to generate distributions of parameters to provide uncertainty of the value in its distribution. However, MCMC cannot provide uncertainty based on the most likely scenarios for peak NPVs, an important attribute to investors.

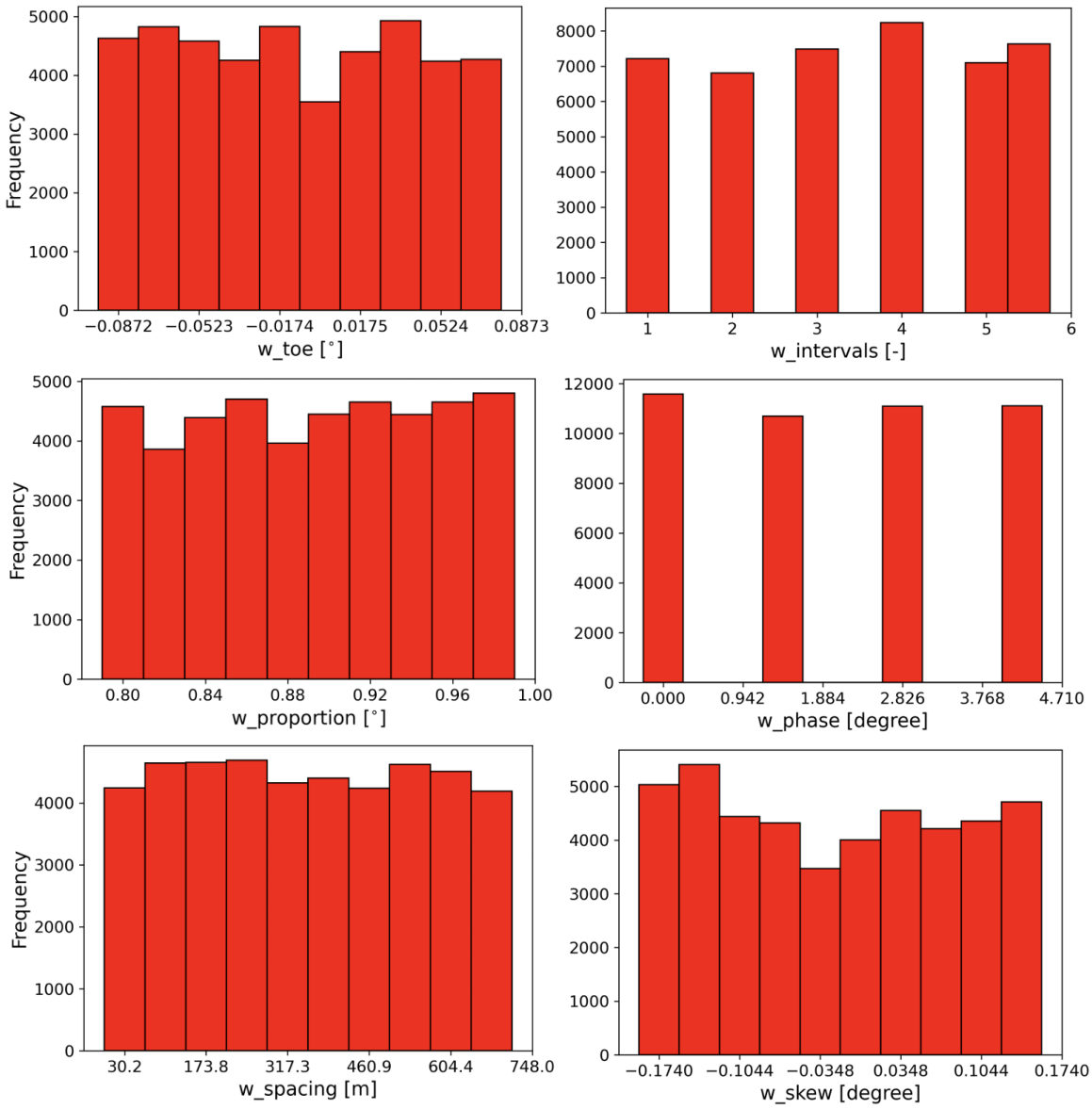

Fig. 5.2: Distribution of design parameters for well.

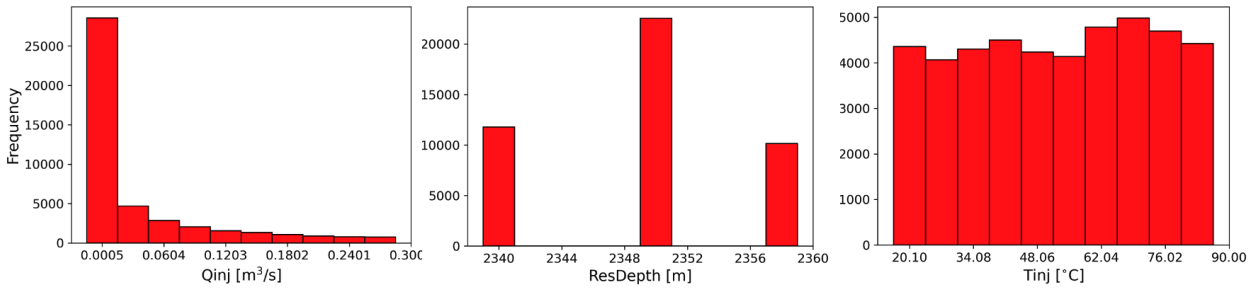

Fig. 5.3: Distribution of injected flow rate (Qinj), reservoir depth (ResDepth), and temperature of injected fluid (Tinj).

Investors would like to see what is the most likely chance of a profitable geothermal project based on NPVs; for instance, what are the 10^{th}, 50^{th}, and 90^{th} percentile of NPVs for a given set of design parameters? Therefore, we chose binning-based optimization in this study (Fig. 5.4). In this technique, we define a bin volume based on discrete splitting of the design parameter values of injection rate and well spacing. Then, we compute NPVs of each realization in the corresponding volume. Finally, we compute the 10^{th}, 50^{th}, and 90^{th} percentile of NPVs and their corresponding design parameters. Here, percentile values of NPV demonstrate the profitability of geothermal fields while the design parameter ranges provide the range within which the NPV would be profitable. For this study, w_spacing and Qinj were evenly split into 9 and 4 intervals, giving a total of 36 bins for our realizations. Nine intervals provided the finest discretization that yielded suitably large populations of data within each bin for achieving statistical significance.

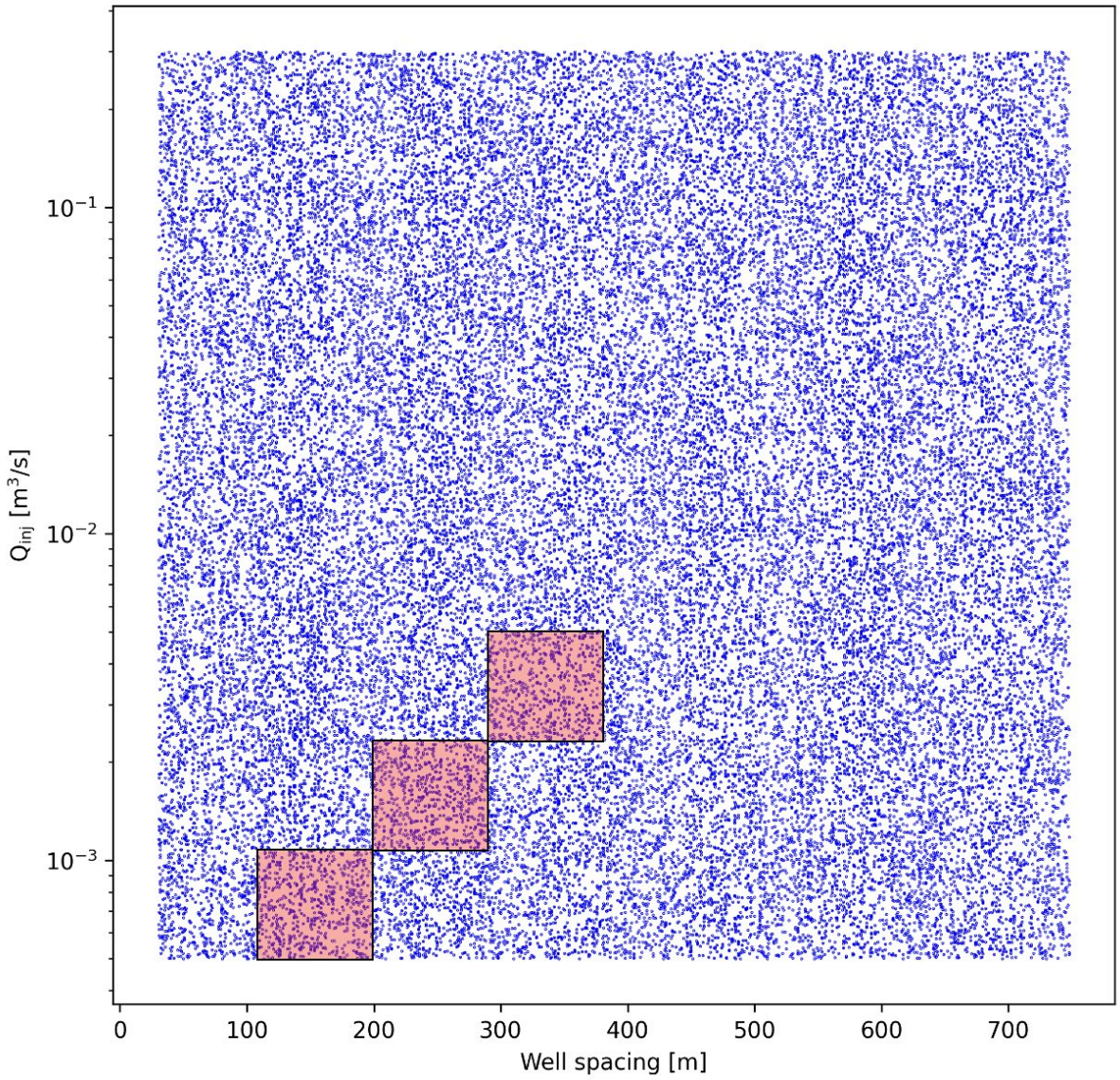

Fig. 5.4: Binning based optimization technique where blue dots represent each realization and red color rectangle shows example binned areas.

Results

The model's NPV values are widely distributed, ranging from negative to hundreds of millions USD (Fig. 5.5). We plotted the frequency distribution plot of NPVs using 30 bins. The most common outcome was negative NPV due to the relatively cold 200℃ temperature at the current depth of FORGE when treated as an EGS. Out of 44,492, 42,960 (96.55%) realizations fall into this non-profitable category. Only 3.45% or 1,532 realizations fall into the profitable category. The profitable NPVs range from 0 to ~1500 million USD. The most likely profitable range was 25 to 676 million USD.

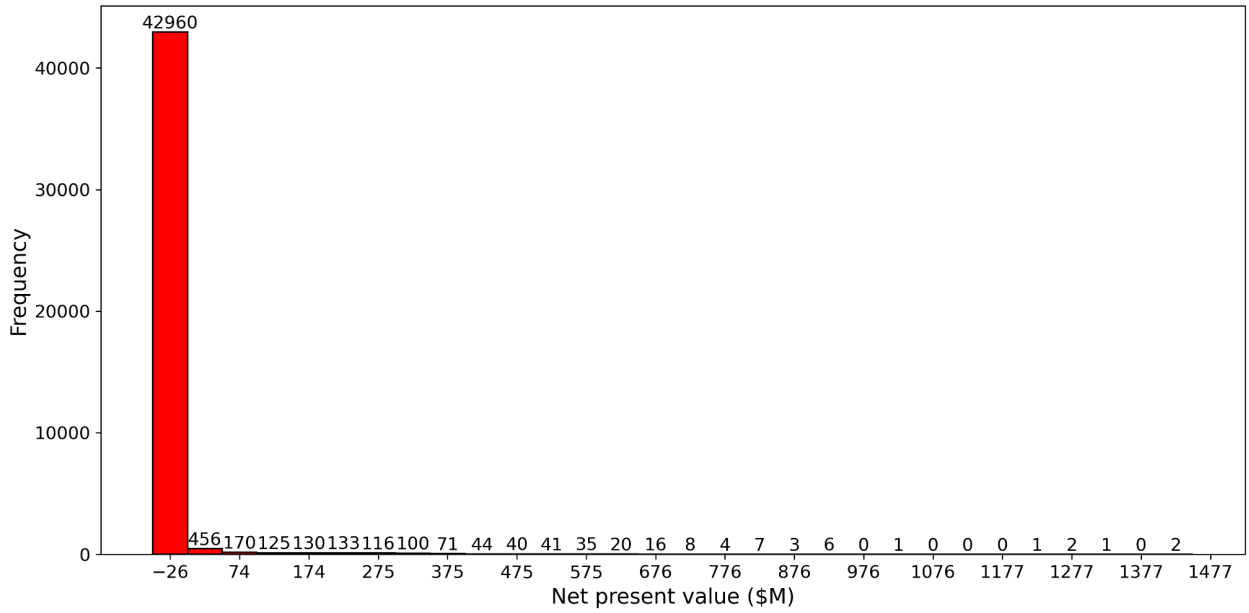

Fig. 5.5: Histogram of NPVs where negative and positive values represent non-profitable and profitable geothermal fields, respectively. The number on top of each bar represents the total count of NPV for the corresponding bar. All drilling costs and pumping losses are included in this model. Note that this plot includes non-optimized flow rates and well spacing. For additional reading, please refer to Frash et al., 2023[113].

All NPVs are plotted against Qinj and w_spacing in Fig. 5.6. Here, only positive or profitable NPVs are present, while negative values are absent. It is clearly shown that geothermal fields are non-profitable or marginally profitable for Qinj < 0.01 m^3/s. High and extreme Qinj at rates above 0.2 m^3/s do not make a geothermal project profitable either. Therefore, the optimization of Qinj is critical for achieving economic EGS, which confirms our apriori expectation but now better quantifies this trend. A similar optimization trend is less visible for w_spacing because profitable to non-profitable geothermal fields are present across the full w_spacing range. Therefore, we applied a binning-based optimization technique to find optimal w_spacing and Qinj.

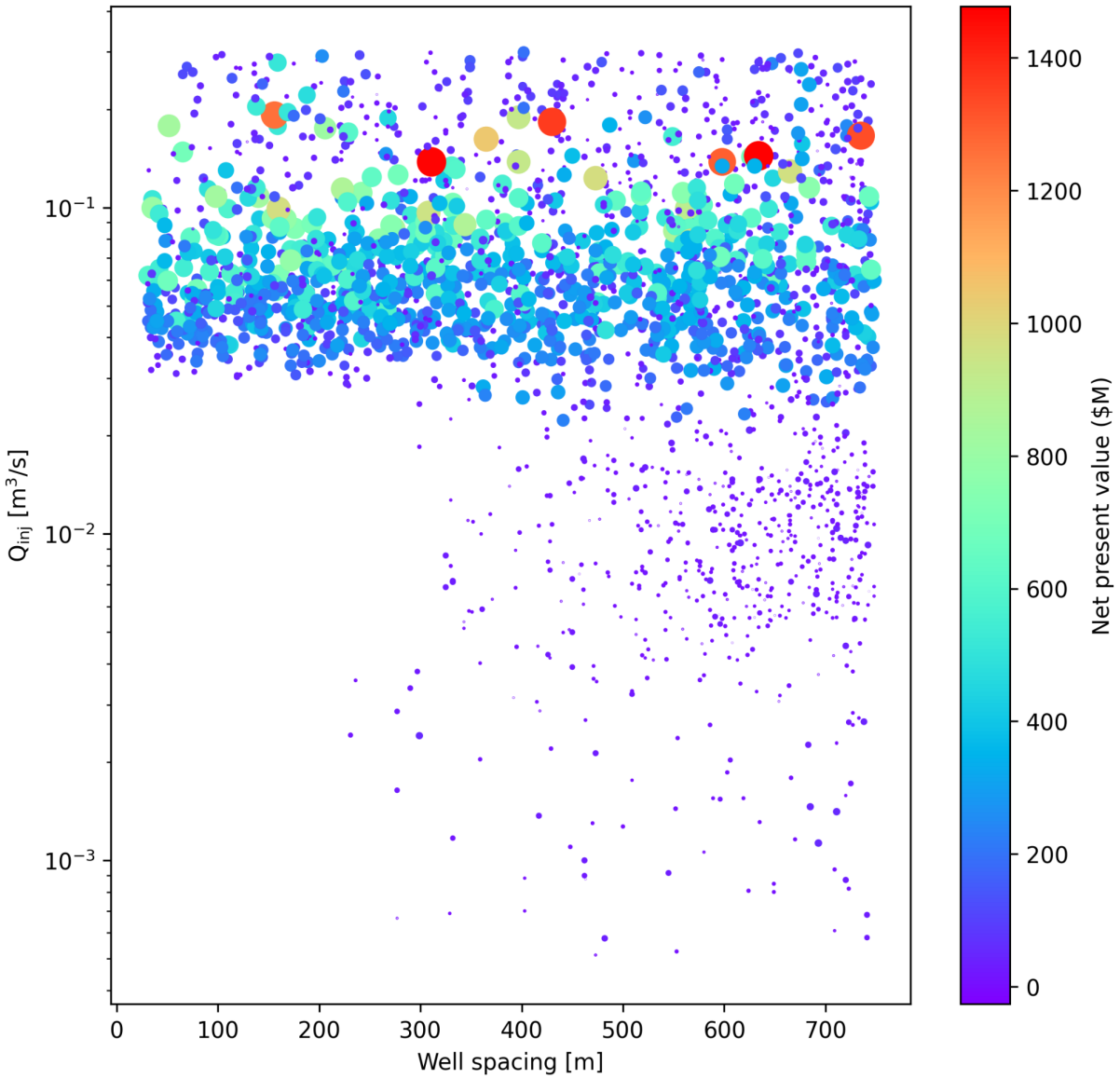

Fig. 5.6: Positive (profitable) NPVs against Qinj and w_spacing where color and size represent NPVs. Warm and larger-sized circles represent higher NPVs or vice versa. Most realizations are not in this plot because of their negative USD values.

The 10th percentile values show profitable geothermal fields most likely occur between 110 to 348 m w_spacing and 0.0005 to 0.001 m^3/s Qinj (Fig. 5.7a). Here, the closer space provides more profit because of the presence of fluid. The highest profit within the 10th percentile reached up to 0.5 million USD. The 50th percentile values demonstrate that profitable geothermal fields are feasible between 190 and 747 m w_spacing and 0.001 - 0.01 m^3/s Qinj (Fig. 5.7b). The highest profit within the 50th percentile reached up to 5.5 million USD.

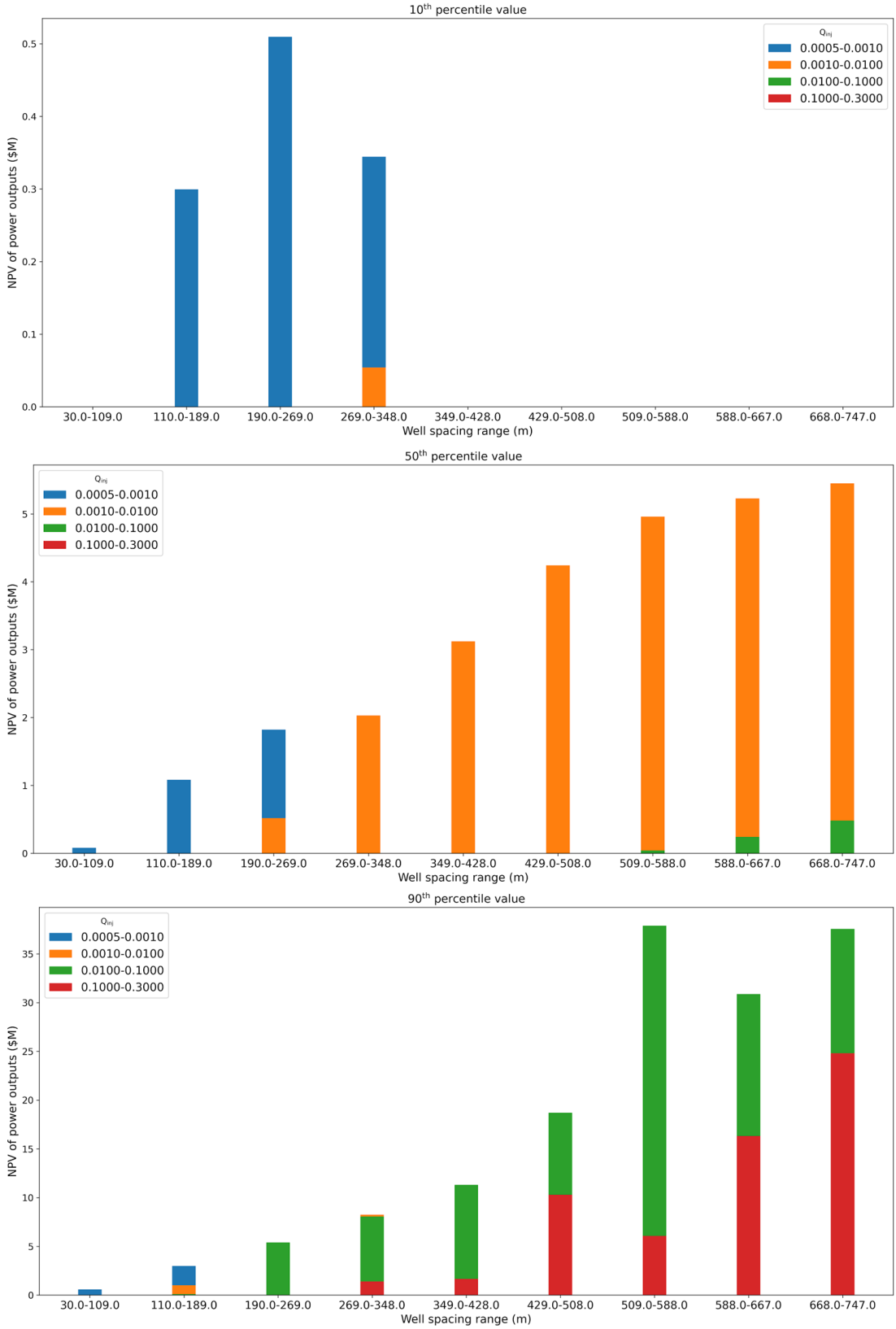

Fig. 5.7: 10th (a), 50th (b), and 90th (c) percentile values of NPV in USD.

The 90th percentile values show more interesting characteristics across the ranges for both Qinj and w_spacing (Fig. 5.7c). Although all Qinj seem profitable, the prominent Qinj is 0.01 to 0.1 m^3/s. The next most profitable Qinj range is 0.1 to 0.3 m^3/s. The w_spacing range between 190 to 747 m is profitable. Among these ranges, the most profitable range is between 509 to 588 m. The next most profitable w_spacing range is between 668 to 747 m. The highest profit within the 90th percentile can reach up to ~36 million USD. For both 50th and 90th percentile cases, low w_spacing provides less profit, and high w_spacing provides higher profits. This phenomenon contradicts the idea that close spacing will benefit from having a better flow rate. Here, the total fluid volume generated more heat, thereby, more profits. So, it is clear that a total hot fluid volume is preferred to the flow rate in estimating NPV. In other words, more w_spacing provides more volume, facilitating more fluid extraction.

Conclusions

We analyzed GeoDatathon data based on the Utah FORGE site parameters. The dataset has a total of 16 design parameters that control geothermal energy production, hence, its NPVs in USD. The primary goal of this study is to find the optimal design values for well spacing (w_spacing) and per-interval injection rate (Qinj) for developing profitable geothermal fields with specified uncertainties. We used a binning-based optimization technique to compute NPVs. We subdivided the whole realizations into 36 bins based on nine ranges for both w_spacing and Qinj. Following, NPV was calculated for all realizations in each bin. Next, we computed 10th, 50th, and 90th percentile scores of NPV in all bins. Based on the analysis, we came to the following conclusions: (1) The 10th percentile values demonstrate that profitable geothermal fields are feasible between 110 to 348 m w_spacing and 0.0005 to 0.001 m^3/s Qinj. The maximum profit can reach up to 0.5 million USD. (2) The 50th percentile values demonstrate that profitable geothermal fields are possible between 190 to 747 m w_spacing and 0.001 - 0.01 m^3/s Qinj. Low w_spacing provides less profit, and high w_spacing provides high profits. The maximum profit can reach up to 5.5 million USD. The 90th percentile values are better to consider than the 10th and 50th percentile values because of (1) higher certainty and wide ranges of w_spacing and Qinj. The most profitable Qinj is between 0.01 to 0.3 m^3/s. The w_spacing range between 190 to 747 m is profitable. Among these ranges, the most profitable range is between 509 to 588 m. The next most profitable w_spacing range is between 668 to 747 m. The maximum profit can reach up to 35 million USD.

Chapter 6: Coupling Thermo-hydro-chemical Modeling and Markov Chain Monte Carlo Method for Permeability and Porosity Estimation in a Geothermal Reservoir

Introduction

Accurate geothermal reservoir characterization and maintenance help design a profitable geothermal power plant[3,93]. Specifically, accurate estimation of permeability and porosity is crucial for understanding the fluid flow mechanism and resource estimation of a geothermal field. For instance, higher permeability and porosity values could provide over-optimistic resource estimation and resource extraction mechanisms or vice versa. However, the detailed permeability and porosity field of geothermal fields remains unknown because of sparse core measurements. Crucially, there is no workflow for determining permeability and porosity values with quantified certainties from sparse measurements. The primary goal of this study is to demonstrate a workflow that estimates the permeability and porosity distribution in a geothermal site from sparse core measurements.

Several studies predicted the permeability of geothermal reservoirs using either numerical simulation or lab experiments[94–100]. One notable study was performed by Jafari and Babadagli[97] on estimating correlation coefficient of fractures by investigating the fractal and statistical parameters of fractures. The major limitation of this study is that they did not use critical geothermal measurements, e.g., groundwater temperature and tracer concentration, to constrain the model. Catinat et al.[98] used nuclear magnetic resonance measurements to establish a relationship between porosity and permeability. This approach is reliable with two limitations: (1) data are sparse, and (2) it fails to provide a good relation if one considers the total porosity. Weibel et al.[95] developed a relationship between porosity and permeability in low-enthalpy geothermal reservoirs by investigating the effect of diagenesis on sandstone permeability. However, they did not verify the relationship between groundwater temperature and tracer concentration. Jiang et al.[99] estimated heterogeneous permeability distributions in an enhanced geothermal synthetic reservoir by combining an autoencoder neural network and a Bayesian inversion algorithm based on Markov chain Monte Carlo (MCMC) sampling. They used single-well injection withdrawal as measurement data that are not readily available. Suzuki et al.[100] developed a supervised machine-learning-based model, random forest, for estimating permeability distributions for a geothermal field using temperature and pressure distribution as measurements.

The preceding studies did not estimate permeability or porosity, constraining the model based on critical attributes for geothermal exploration. The critical attributes are groundwater temperature and tracer (e.g., Li^+, Ba^{2+}) concentration in the subsurface. Groundwater temperature captures thermal gradient or heat flow, while tracer concentration indicates deep fluid circulation[1,101]. Moreover, they are easy to measure, and USGS installed numerous wells to measure these two attributes. To address the limitations, we estimated permeability and porosity of a 3D reservoir scale model constrained by groundwater temperature and tracer concentration.

For such a parameter estimation study, many flow, heat flux, and chemical transport simulations are often needed. Although the high-fidelity coupled thermal-hydrologic-chemical (THC) model

is reliable and accurate in performing this task, the computational cost is huge. With the growth of parallel computing hardware like Graphical Processing Units(GPU), integrating machine learning (ML) tools could greatly speed up the simulations while maintaining accuracy. In this study, we train a deep CNN model as the surrogate using a relatively small and accurate simulation dataset obtained from the coupled THC model runs using PFLOTRAN[44]. Next, we generated 6,000 permeability and porosity distribution realizations coupling the CNN model and MCMC sampling. Moreover, we discuss when MCMC performs better.

Data Generation

This study is on thermal-hydrologic-chemical physical processes involved in heat conduction and energy transfer due to fluid flow and chemical transport in a site-scale reservoir[102]. The governing equations for fluid flow, chemical transport, and heat transfer processes are explained in Mudunuru et al.[102]. This study develops a 3D model with heterogeneous and anisotropic porous geologic systems representing the Tularosa Basin in New Mexico using PFLOTRAN. The model dimension is 6000 x 6000 x 6000 m^3, discretized into 10 x 10 x 30 grid cells. We developed a big model to capture the optimal temperature distribution in the model domain[103].

The PFLOTRAN simulator takes the following terms as the variable input: the permeability, the initial temperature profile, the heat flux on the bottom of the reservoir modeling the geothermal resource, and the tracer concentration of lithium and boron. Other modeling parameters, such as fluid thermal conductivity, solid thermal conductivity, rock density, and diffusivity, are known and are considered uniform over the simulation domain. The same Neumann boundary conditions are applied to the west, east, north, and south faces of the 3D rectangular domain, i.e., no flow, no heat or concentration flux. The pressure on the top and bottom faces is fixed; the flow is upward with the higher bottom pressure. Zero concentration fluxes are assumed on the top and bottom surfaces. The only varying boundary condition is the heat flux on the bottom face.

Aiming for a neural network surrogate model to predict the pressure, tracer concentration, and temperature field, we adopt a dataset containing various combinations of a stratified permeability field, initial temperature gradient, and heat flux on the bottom as the input, the corresponding future temperature gradient, liquid pressure, tracer concentration as the output.

The initial temperature field is determined with the initial temperature gradient; the initial temperature at the top surface is assumed to be 25°C/km and 25°C. The temperature is proportional to depth in the entire domain, assuming a uniform geothermal gradient of 25°C/km. The bottom heat flux and initial temperature gradient are randomly drawn from the uniform choices shown in Table 6.1. The permeability field of the modeling domain is discretized into nine geologic layers. The rock types, depth, and range of permeability of each layer are listed in Table 6.2[1,104]. The temperature, tracer, and pressure distribution at the first and last time steps are shown in Figs 6.1 and 6.2, respectively.

Table 6.1: Input parameters ranges for the initial temperature gradient and the bottom heat flux.

Parameter Name	Uniform random choices
Initial temperature gradient: °C/m	$[0.023, 0.024, ..., 0.04]$
Bottom heat flux: W/m^2	$[0.06, 0.07, 0.08, 0.09]$

Table 6.2: Permeability of the 9 layers. The permeability of each layer is drawn from the three choices following Gaussian distribution.

Layers	Rock type	Thickness [m]	$\log_{10}$k [m^2] range
Layer 1	Fluvial sediments	800	$[-13, -12, -11]$
Layer 2	Lava flow and ash flow	1000	$[-17, -16, -15]$
Layer 3	Sandstone, shale, and conglomerate	2000	$[-18, -17, -16]$
Layer 4	Sandstone, shale, and conglomerate	200	$[-18, -17, -16]$
Layer 5	Mudstone, sandstone, and siltstone	200	$[-16, -15, -14]$
Layer 6	Limestone, shale and dolomite	800	$[-12, -11, -10]$
Layer 7	Limestone and shale	200	$[-13, -12, -11]$
Layer 8	Limestone and dolomite	400	$[-14, -13, -12]$
Layer 9	Granite and metamorphic	300	$[-16, -15, -14]$

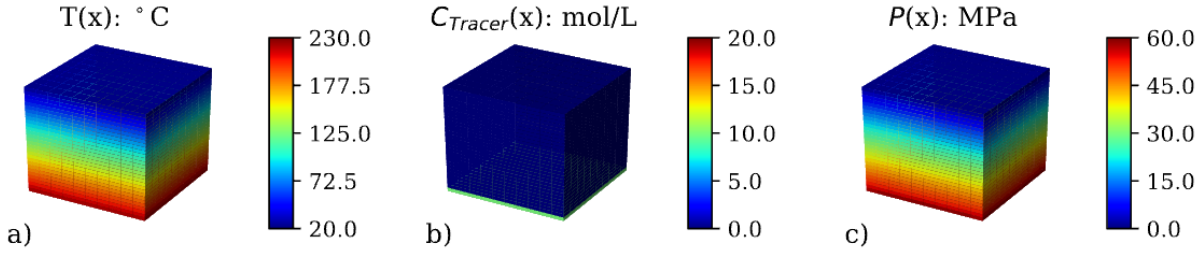

Fig. 6.1: Distribution of (a) temperature, (b) tracer, and (c) pressure at the first time step.

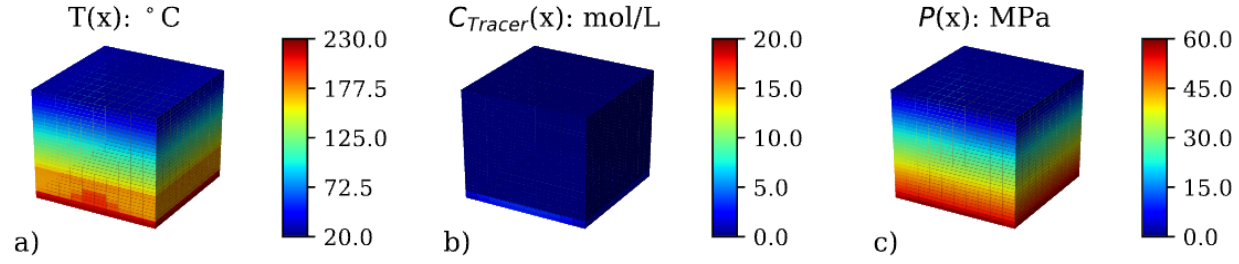

Fig. 6.2: Distribution of (a) temperature, (b) tracer, and (c) pressure at the last time step.

Neural Network Surrogate

For inverse analysis and the MCMC approach, the model is evaluated multiple times. Consequently, the development of a surrogate model significantly accelerates the analysis. We train a deep neural network (DNN) in order to perform the same task as the PDE solver. For the surrogate model, we choose an image-to-image 3D Convolutional Neural Network (CNN) with encoder-decoder architecture because it performs well for simulating contaminants transports in the subsurface[105,106]. The input of the model is a 6-channel of 10 x 10 x 30 voxels, consisting of the initial pressure, initial temperature, initial tracer concentration, permeability, porosity, and heat flux. For using heat flux as a boundary condition, the heat flux input is a 3D matrix with zero values everywhere except the bottom, where the value of the boundary heat flux is given. The permeability in the vertical direction is defined as 1/10 of the horizontal permeability; therefore, the vertical input was not as an input as it would be redundant.

The kernel of the CNN model consists of 3 x 3 x 3. For capturing physics in the dataset, the number of layers in the encoder part is increased while the number of voxels is decreased after every convolution. The proposed architecture is based on DenseNet, which transfers the features from all the preceding layers to facilitate backpropagation of gradient information[107]. The softplus is used for the activation function. The decoder part takes the same steps as the encoder but in reverse order, resulting in the output matrices having the same dimensions as the input. The initial number of filters after the first convolution and the rate of increase of the filters after each following convolution for the encoding are two hyper-parameters that are investigated for their influence on the model accuracy. The L_1 norm is used as the loss/cost/objective function for training the model.

The output of the model is 72 channel 10 x 10 x 30 voxels, which consists of pressure, temperature, and tracer concentration for 24 time-steps corresponding to the PFLOTRAN output timesteps. A different approach would be an auto-regressive approach that would predict the features for the next time steps and use them as input for the next time step. The approach of using all the time steps as the output instead of advancing the CNN for one time step each time is selected because the outputs can have a varying time interval without cumulative errors.

The output data consists of three quantities of interest with significantly different orders of magnitude; for this reason, the data is normalized, and all input and output values are divided by their corresponding standard deviation. Furthermore, the concentrations of the tracers are more difficult to predict and more localized; therefore, they are weighted differently for the regions where significant changes are observed in the domain. The weight of the localized L_1 norm of the tracer W_c is an additional hyperparameter that was tuned during the study to achieve the best-performing surrogate model. The ADAM algorithm is used to optimize the CNN model because it is good at searching a wide range of hyperparameters[108]. The additional hyperparameters are the learning rate and the weight decay of ADAM algorithm. A grid search was performed for the hyperparameters and is listed in Table 6.3.

Table 6.3: Hyperparameter range for the optimization of the CNN model.

Parameter Name	Values
Initial layer number	[64, 128, 256, 512]
Growth rate	[32, 64, 128]
Learning rate	[1e-4, 1e-5, 5e-6, 1e-6]
Weight decay	[1e-4, 1e-5, 1e-6]
Tracer weight	[1, 10 , 50, 100, 200, 500]

MCMC analysis

This step's main objective is to estimate the porosity and permeability of model layers using temperature, tracer concentration, and pressure as proxies of measurements. For an efficient sampling of model parameters, the No-U-Turn Sampler (NUTS) is selected for the MCMC framework[109], which is a gradient-based modified Hamiltonian Monte Carlo (HMC) approach[110]. For MCMC, a PFLOTRAN forward solution is used as the ground truth. The data/measurements are the surface temperature, the heat flux, and the initial temperature gradient. Additionally, we consider that the time series for the temperature, tracer concentration, and pressure for voxels are scarcely distributed in three vertical columns. This sampling imitates the use of three vertical wells measuring the required information. Therefore, the unknown parameters we obtain through inference are porosity and permeability.

Each layer's permeability and porosity realizations are generated using the uniform distribution with their corresponding range. Subsequently, the values are normalized and formed as the input of the trained CNN model. Next, a normally distributed random noise is added to the model outputs to capture the model and measurement errors. The final outputs are conditioned to the solution of the ground truth obtained. Finally, the MCMC sampler is used to obtain the posterior distribution of the inputs. Experiments are performed on hardware with the following specification: Intel Xenon Gold 6126 CPU (2.6 GHz), 60GB RAM, and Nvidia V100 GPU with 16GB vRAM.

Results

CNN Surrogate Training

The 2,000 simulation results are used to train and evaluate the surrogate model. After generating the input-output pairs, 1,600 are used for training, and the remaining 400 pairs serve as the testing set. The evaluation of the model is based on the R^2 value (Fig. 6.3). Training and testing scores are close to 1 in the best-performing CNN models (Table 6.4). The optimal hyperparameters for the best-performing models are listed in Table 6.4.

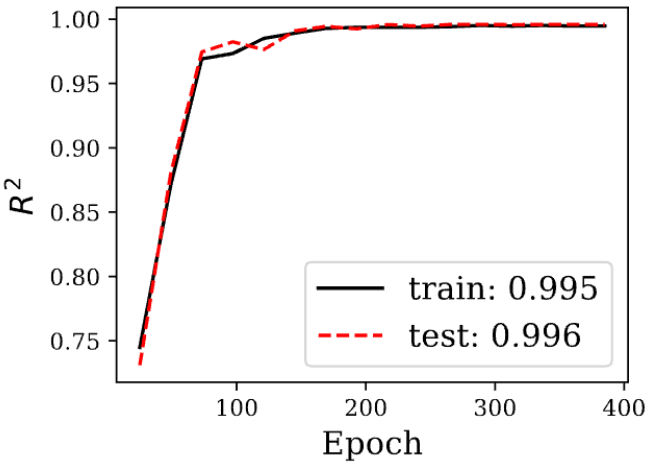

Fig. 6.3 High and consistent training and testing scores suggest a well-trained model.

Table 6.4: The best-performing models and their corresponding hyperparameters.

R^2 Train Set	R^2 Test Set	Initial number	Growth rate	Learning rate	Weight decay	Tracer weight
0.995	0.996	512	128	10^{-4}	10^{-5}	100
0.994	0.995	256	128	10^{-4}	10^{-5}	100
0.994	0.995	512	128	10^{-4}	10^{-6}	100
0.993	0.994	256	64	10^{-4}	10^{-5}	100
0.992	0.994	256	64	10^{-4}	10^{-6}	100
0.992	0.994	512	64	10^{-4}	10^{-5}	100
0.992	0.994	256	128	10^{-4}	10^{-6}	100
0.993	0.994	512	64	10^{-4}	10^{-6}	100
0.992	0.993	512	128	10^{-4}	10^{-5}	200
0.992	0.993	512	64	10^{-4}	10^{-5}	200

The CNN model is only trained for 400 epochs because, after it, the R^2 scores of training and testing reach a plateau (Fig. 6.3). The optimal initial number of channels and the growth rate are relatively large compared to models with similar architecture used for other tasks. The potential reasons are relatively larger outputs and more time steps in the outputs. However, similar R^2 values for training and testing sets indicate that the model is not overfitted instead of complexity in the dataset (Fig. 6.3). The minimum difference between the prediction of temperature, tracer, and pressure by PFLOTRAN and ML model also suggests a well trained ML model (Fig. 6.4).

MCMC Inference

We drew a total of 6000 samples and discarded 2000 samples in the burn-in stage; therefore, the estimation of the parameters relies on 4000 samples. MCMC inference of porosity and permeability values for the first three (bottom) layers is consistent (Figs 6.4–6.5). However, there are discrepancies in the porosity and permeability prediction for the top six layers. Note, the first layer has a high tracer concentration while the top layers have a low tracer concentration.

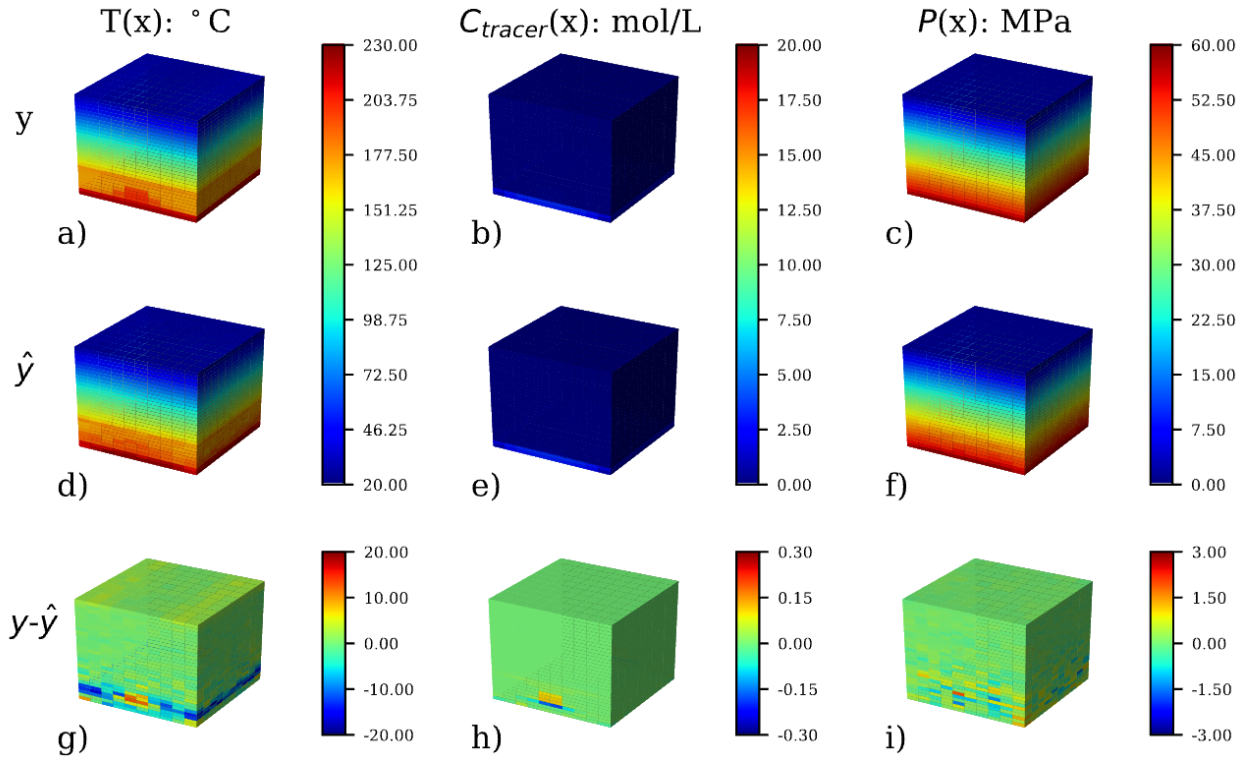

Fig. 6.4: Distribution of temperature by PFLOTRAN (a), ML model (d), and PFLOTRAN–ML model (g); tracer distribution by PFLOTRAN (b), ML model (e), and PFLOTRAN–ML model (h); pressure distribution by PFLOTRAN (c), ML model (f), and PFLOTRAN–ML model (i) after the last time step.

The discrepancy of the real value and the estimated value for the higher layers can be explained by the fact that the tracer plume is not reaching above the third layer and therefore there is no information that can be assessed by the model. It is worth noting that for the first layer for which there is the most flow of the tracer the standard deviation of the estimated parameters are in the order of 0.05 and 0.01 for permeability and porosity accordingly. The difficulty of the MCMC method to estimate the parameters of the higher layers shows the importance of the correct regularization as the tracer moves upwards is diluted and the concentration decreases by an order of magnitude. Therefore, if there was no normalization the MCMC would not be able to provide any reliable information for the second and third layer.

NUTS sampling uses gradient information to facilitate faster convergence of the distribution. The main advantage of the use of the neural network surrogate model is the efficient calculation of every iteration, as the average time for sampling is 1.5 secs. Additionally, the PFLOTRAN or other subsurface simulators are not developed to leverage the GPU architecture; thereby, its integration with a probabilistic programming platform would be more challenging. The use of the open-source and off-the-shelf solution for both the surrogate model and the MCMC inference do not only decrease the development time but also increase the efficiency as the implementation have been developed and maintained to fully utilize modern hardware.

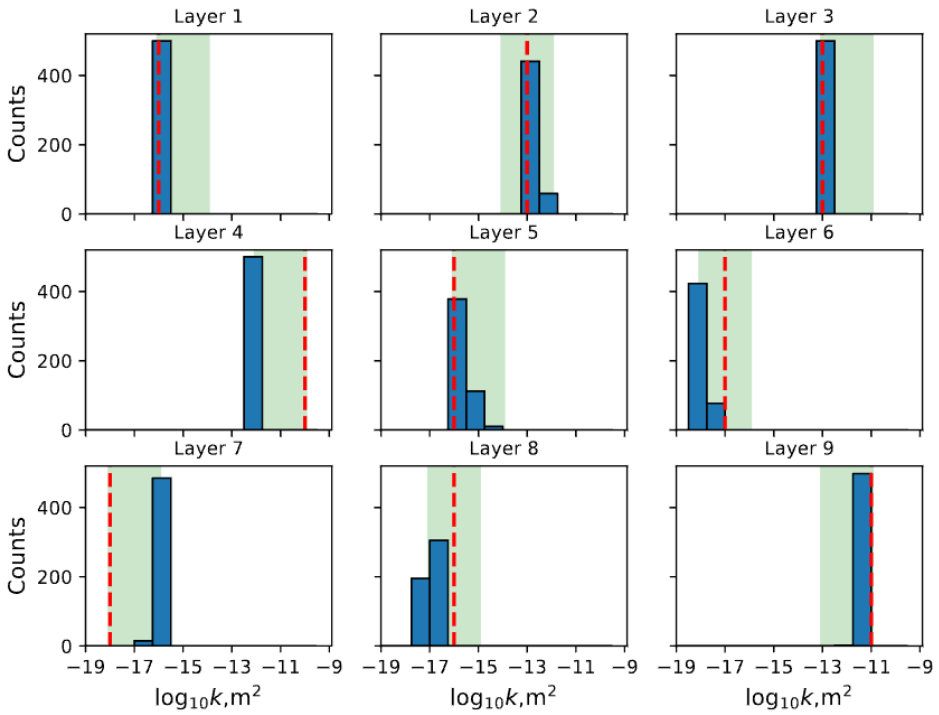

Fig. 6.5: Histograms of assimilated permeability on each layer. The green shaded area indicates the range of the initial guess, and the dotted line is the ground truth.

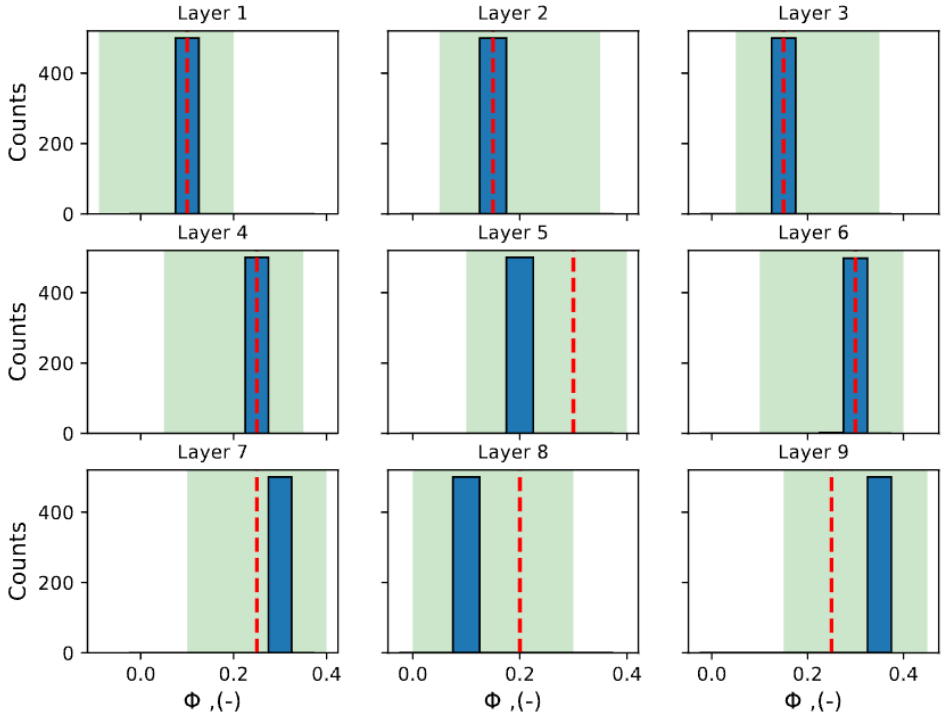

Fig. 6.6: Histograms of assimilated porosity on each layer. The green shaded area indicates the range of the initial guess, and the dotted line is the ground truth.

Conclusions

For this study, the use of MCMC with NUTS sampling was proposed to infer permeability and porosity of a geothermal reservoir. The model used was a surrogate CNN trained on data generated by a PDE-based model. For the inference of the parameters, an example of the generated dataset was used as ground truth and the model is conditioned to data on virtual vertical wells with sparse information. The analysis concludes in the following findings:

1. The CNN-based surrogate model can reproduce the results of the PDE-based solution of both thermal and advection processes.

2. The MCMC using a surrogate model can evaluate the unknown parameters if enough information is provided, as it happens for the first layers.

3. For the areas where there is no change of concentration and temperature, the permeability and porosity inference is unreliable, as the inverse problem is ill-posed.

4. The use of a surrogate model can significantly decrease the computation time as the complex PDE-based model is evaluated only 2000 times, which is the number of realizations needed for the training of the model.

This study shows that the CNN surrogate model can reproduce PDE-based solutions and can be used for inference; they have the same limitations as the PDE-based solutions. In our case, in the area where there was no significant movement of the tracer, it was possible to retrieve the rock parameters reliably. The gain of the proposed workflow is that the time-consuming PDE-based simulation is used to explore the parameter space to train the model and then is substituted with the faster CNN-based model to sample the unknown parameters to reduce computational time.

Chapter 7: INGENIOUS and GeoDAWN Data Processing

INGENIOUS

The U.S. Department of Energy's Geothermal Technologies Office has collected plenty of data through INnovative Geothermal Exploration through Novel Investigations Of Undiscovered Systems (INGENIOUS) Project with an aim to accelerate discoveries of new, commercially viable hidden geothermal systems in the Great Basin, NV, US. The INGENIOUS Project released its data in 2022 on the geothermal data repository available at (https://gdr.openei.org/submissions/1391)[111]. The dataset includes 24 geological, geophysical, and geochemical attributes. Data counts for each attribute significantly vary. Some attributes have too fine resolution data, others are too sparse, and others are between two. The main purpose of this task is to bring them on the same scale so that ML practitioners can load the data and use it for their purpose without going through excruciating preprocessing steps. We curated and processed the dataset. Next, we sometimes used only inverse distance weighting (IDW) or both NMFk and IDW algorithms for predicting data in unsampled locations.

This regional scale dataset provides information for predicting geothermal favourability in the Great Basin region. The geochemical attributes include Al^{3+}, B^{+}, Ba^{2+}, Be^{2+}, Br^{-}, Ca^{2+}, chalcedony, Cl^{-}, HCO3, K^{+}, Li^{+}, Mg^{2+}, Na^{+}, quartz, total dissolved solids (TDS), groundwater temperature. These data are heavily sparse. To remove the sparsity, we used NMFk followed by IDW for interpolation. The common locations were 14,341 geochemical data locations in the Great Basin[36]. The scaled data are shown in Figs 7.1-7.4.

Other geological and geophysical attributes include depth to the basement, dilation rate, magnetic anomaly, seismicity (N50_alpha_10^{-12}/yr), strain rate, shear rate, temperature at 2 m, and heat flow (Figs 7.5-7.6). Depth to the basement, dilation rate, magnetic anomaly, seismicity (N50_alpha_10^{-12}/yr), strain rate, and shear rate contain fine resolution data while temperature 2 m and heat flow contain both coarse resolution and sparse data (Figs 7.5-7.6). We applied IDW to upscale the fine-resolution data and downscale the coarse-resolution data (Figs 7.5-7.6).

Moreover, we fed the processed data to GTC and estimated prospectivities in the Great Basin. It mostly provided accurate results except one false positive (Fig. 7.7). Here, we discovered that we require more geochemistry data for a better prediction in the white rectangular region of Fig. 7.7.

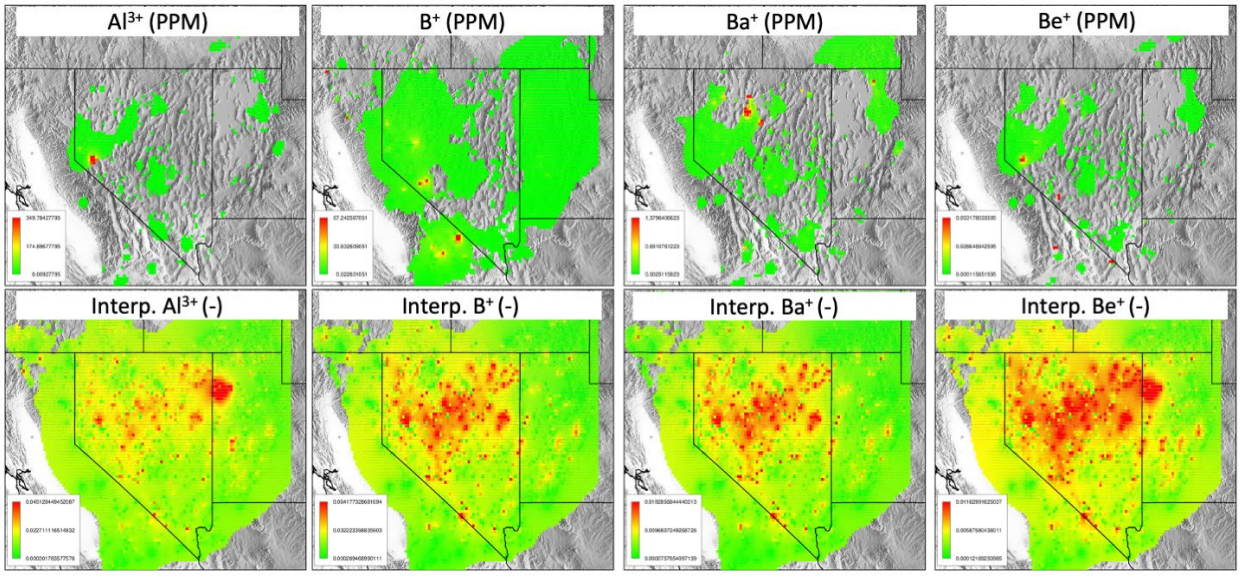

Fig. 7.1: The top and bottom rows represent ingenious and interpolated data, respectively. Here, each attribute was fine-scaled applying IDW on NMFk prediction.

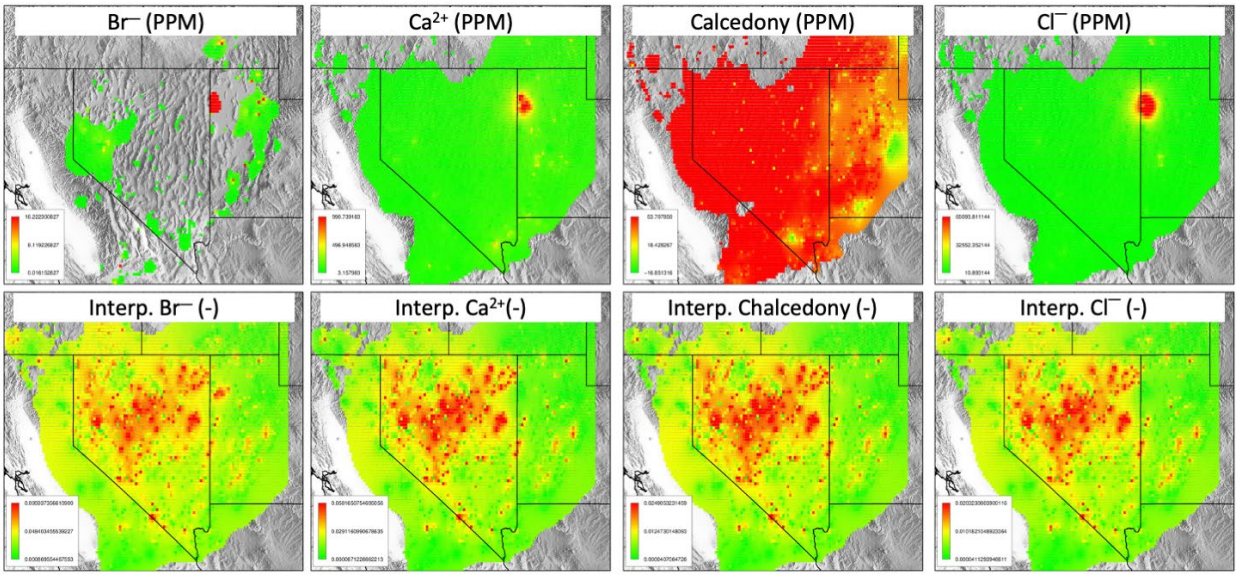

Fig. 7.2: The top and bottom rows represent ingenious and interpolated data. Here, each attribute was fine-scaled applying IDW on NMFk prediction.

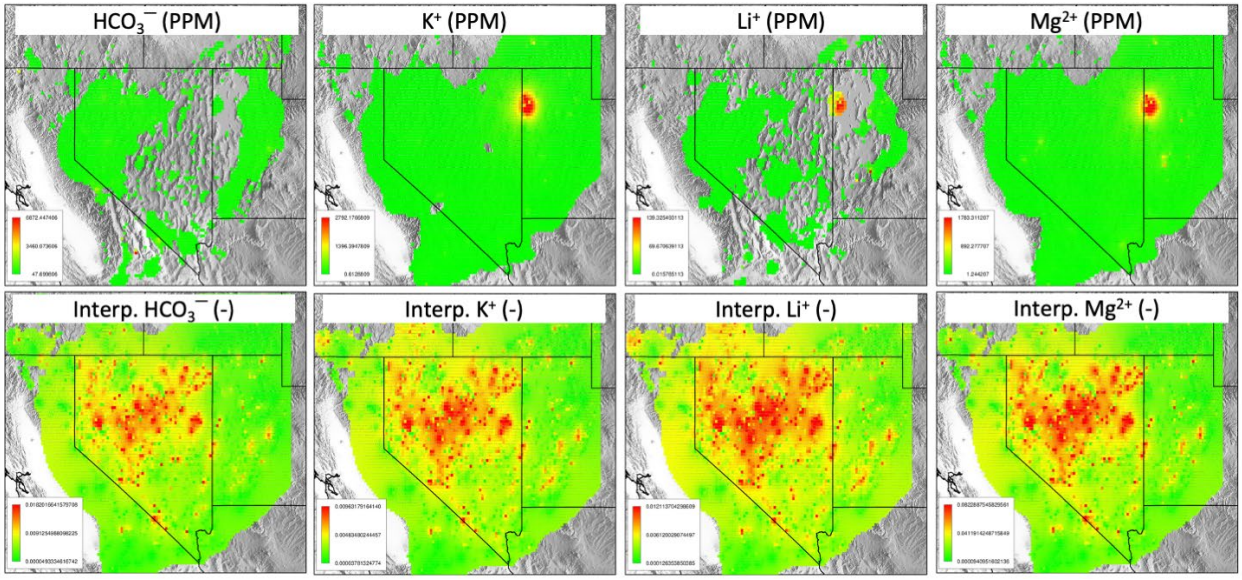

Fig. 7.3: The top and bottom rows represent ingenious and interpolated data. Here, each attribute was fine-scaled, applying IDW on NMFk prediction.

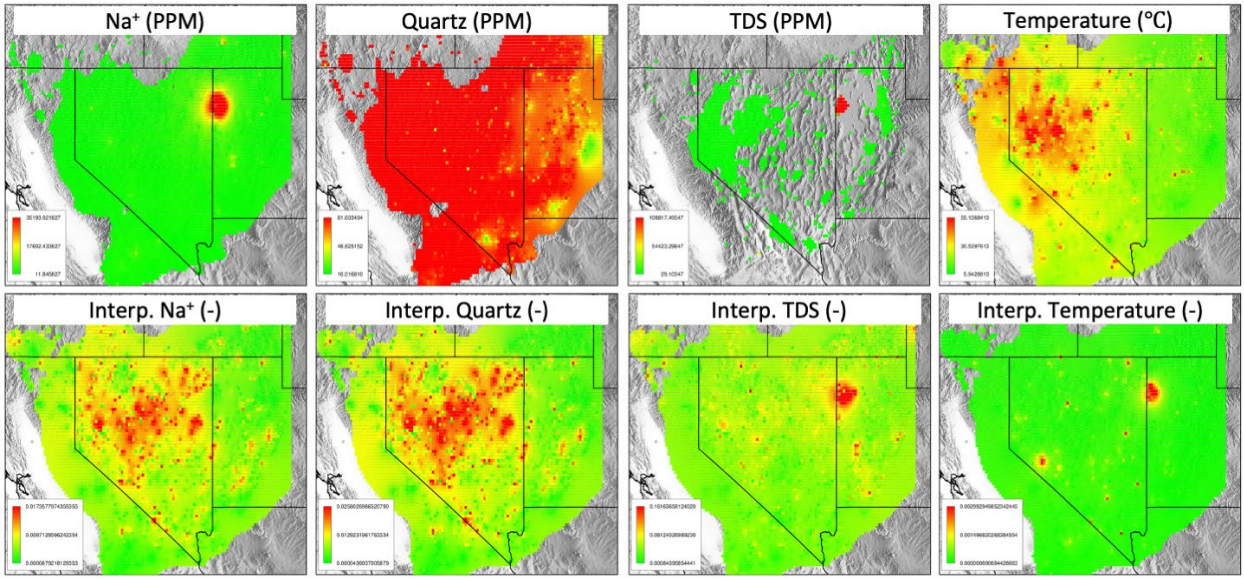

Fig. 7.4: The top and bottom rows represent ingenious and interpolated data. Here, each attribute was fine-scaled, applying IDW on NMFk prediction.

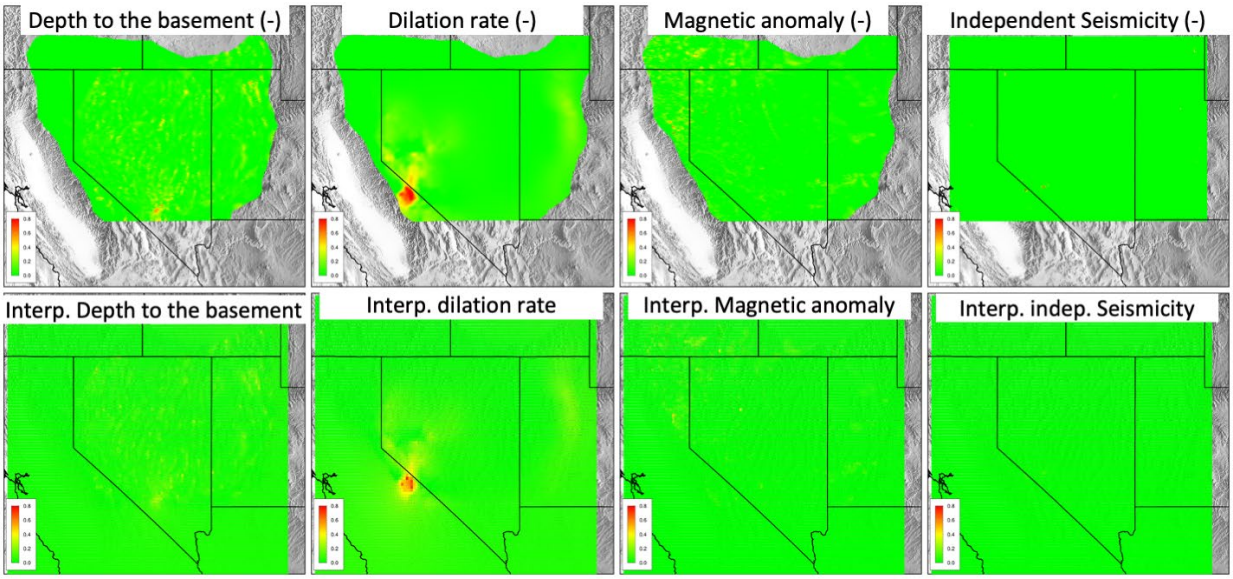

Fig. 7.5: The top and bottom rows represent ingenious and interpolated data. Here, each attribute was upscaled by applying IDW.

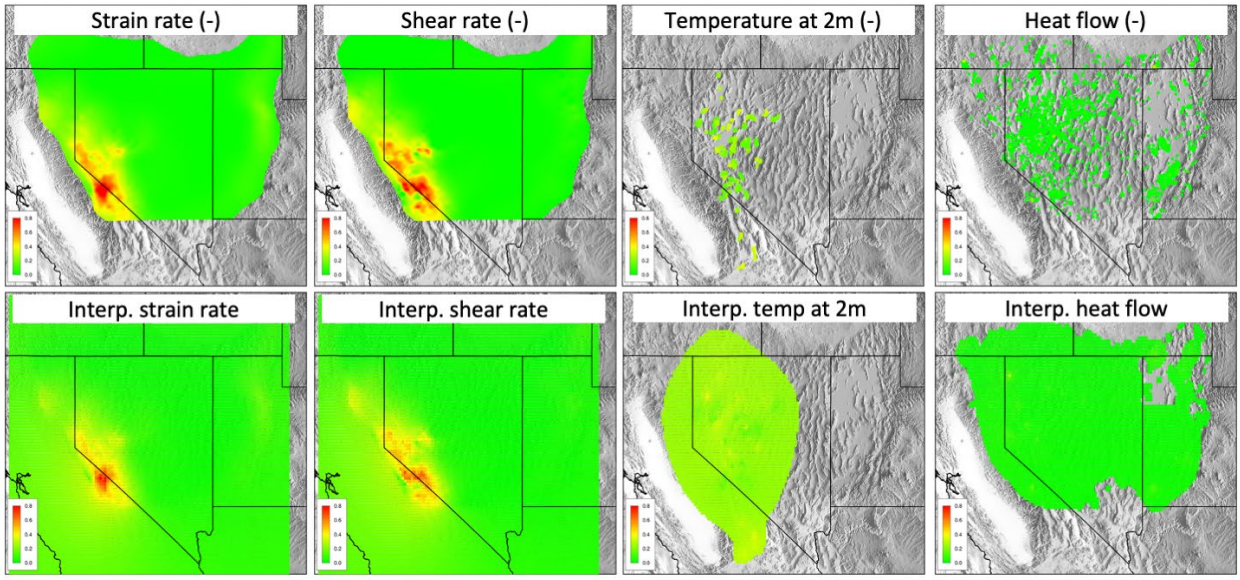

Fig. 7.6: The top and bottom rows represent ingenious and interpolated data. Applying IDW, strain and shear rates were upscaled while the temperature and heat flow at 2m depth were fine-scaled.

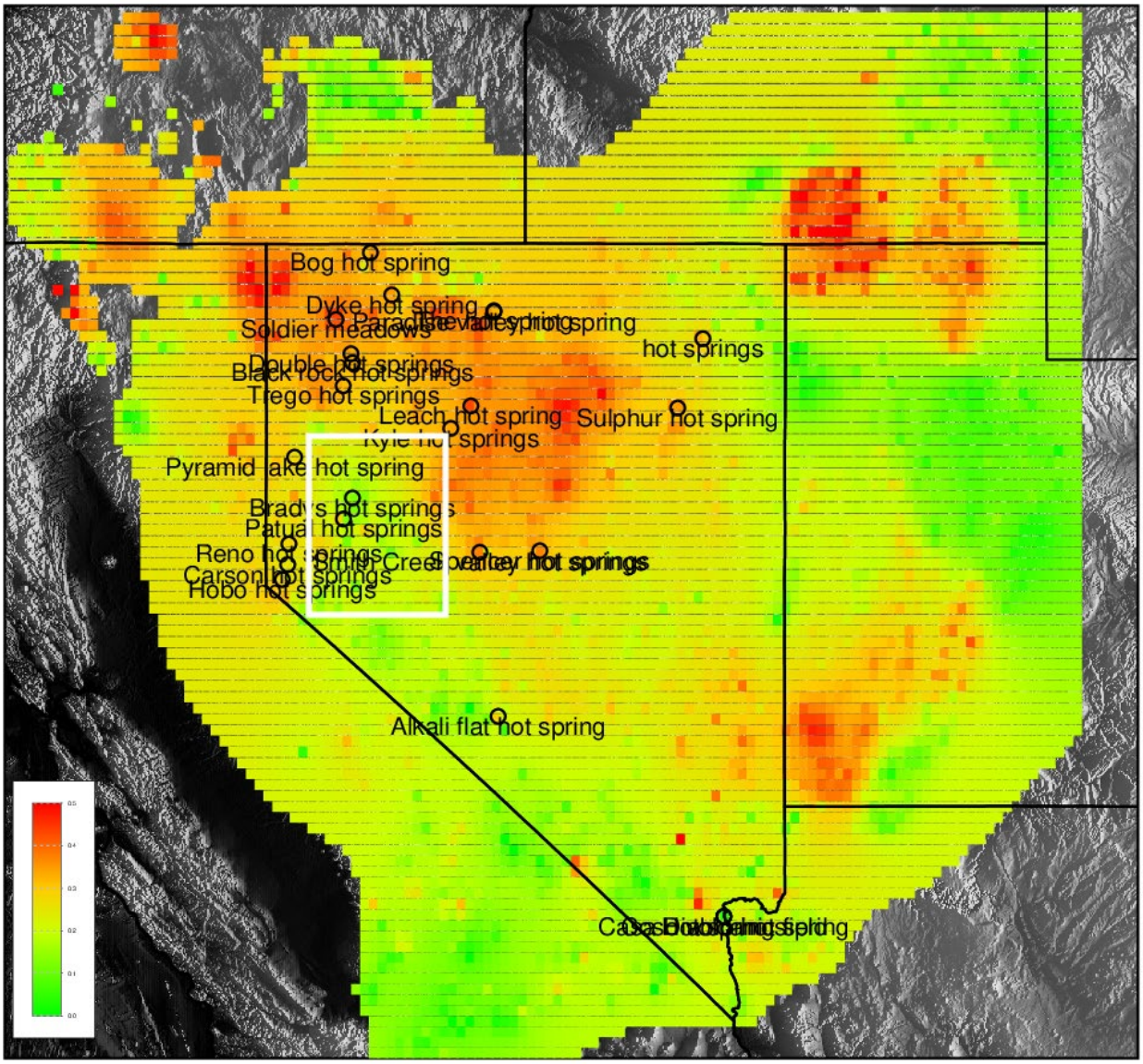

Fig. 7.7: Geothermal prospectivity based on INGENIOUS data. Black circles represent known hot springs in the study area. The white rectangular portion lacks geochemistry data.

GeoDAWN

A recent interagency agreement–Geoscience Data Acquisition for Western Nevada (GeoDAWN)—unites EERE's Geothermal Technologies Office (GTO) with the USGS Earth Mapping Resource Initiative (Earth MRI) and 3D Elevation Program[112]. This initiative aims to collect LiDAR and electromagnetic data to find hidden geothermal resources and critical minerals. Next, use advanced machine learning algorithms to analyze the data and to discover new geothermal and critical mineral resources. So far, this project disseminated LiDAR point cloud (LPC) within Nevada and parts of the CA region (Fig. 7.7). Such a dataset has a huge potential to reduce the risks and costs associated with geothermal exploration and production.

To appropriately utilize this dataset, we need to create labels of favorable geothermal settings with corresponding LPC data. Labeling such a dataset is a non-trivial task because they are huge (in terabytes scale) and contain 1000s of tiles. We have to sort the tiles and find their neighboring tiles. Then, label each tile and whether they contain favorable geothermal settings. For this purpose, we wrote a Python script to sort the tiles and find their neighboring tiles.

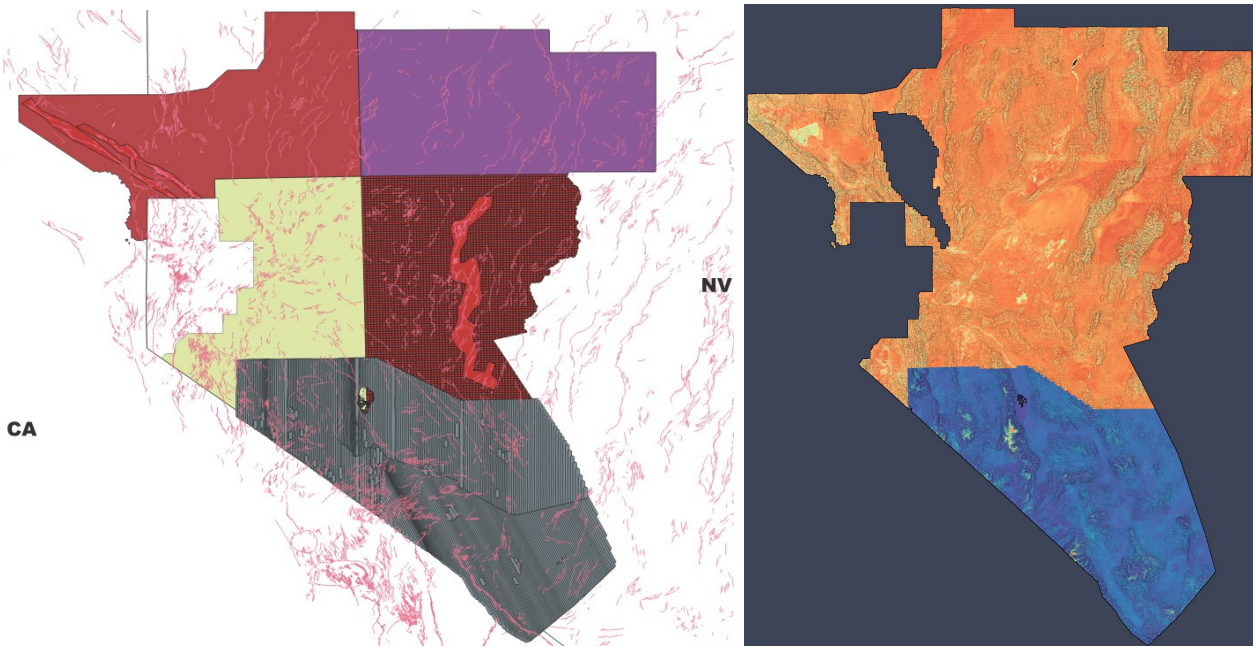

Fig. 7.7: Each color represents a unique flight line duration used to collect lidar data at different times (a) and intensity distribution of the collected lidar data (d).

Chapter 8: Report Conclusions

GTC, an open-source, cloud-based ML framework, is designed for geothermal exploration and can handle public and proprietary datasets. It features advanced pre-processing, post-processing, and visualization tools that simplify applications for non-experts, eliminating the need for deep ML or subject-matter expertise. Built on the novel, award-winning SmartTensors technology from LANL, GTC, along with its component GeoDT-ML, efficiently processes and analyzes diverse, even sparse datasets, uncovering critical actionable insights for decision-making in geothermal exploration and production. Our analysis of eight diverse site datasets demonstrates its capability to reveal key insights not discernible through conventional methods.

Overall, GTC can (1) analyze large field datasets, (2) assimilate model simulations (large inputs and outputs), (3) process sparse datasets, (4) perform transfer learning (between sites with different exploratory levels), (5) extract hidden geothermal signatures in the field and simulation data, (6) label geothermal resources and processes, (7) identify high-value data acquisition targets, and (8) guide geothermal exploration and production by selecting optimal exploration, production, and drilling strategies.

GeoDT-ML, an ML-enhanced version of GeoDT, is a fast, multi-physics solver optimized for EGS design evaluation in uncertain geological conditions, capable of modeling thousands of scenarios quickly on a desktop computer. This study introduces preliminary deep learning workflows to predict EGS economics from design parameters, using a database created with GeoDT and analyzed through sensitivity tests for deeper insights. We offer notebooks and pre-trained ML models on GitHub for the geothermal community to address the computational demands of training and tuning.

In addition to developing GTC and GeoDT-ML, we provided comprehensive solutions for various geothermal challenges. These include (1) accurately determining drilling depths, (2) exploring geothermal resources in West Texas, (3) identifying key design parameters essential for geothermal energy production, and (4) utilizing machine learning techniques for permeability estimation. Furthermore, we enhanced our Great Basin analysis with INGENIOUS data and prepared GeoDAWN data for future applications. The following paragraph details the contributions and outcomes of the first four items.

1. To enhance the precision of our analysis, we integrated field data from the GTC framework with magnetotellurics data. This combination significantly improved our ability to pinpoint drilling depths with greater certainty. We successfully applied this dual-method approach to data from the Tularosa Basin.

2. West Texas offers reasonable geothermal potential across various depths, enabling diverse applications from spas at 1 km depth to greenhouse farming at 2 km. Leveraging geothermal resources and existing oil and gas infrastructure, deeper at 3 and 4 km, binary cycle and steam-

flash power plants become viable for continuous, clean electricity generation. While orphan wells present an opportunity to reduce costs, their feasibility for sustaining thousands of barrels of fluid extraction daily requires in-depth study.

3. In our analysis of the GeoDatathon data, focused on the Utah FORGE site, we examined 16 design parameters crucial for geothermal energy production and their impact on Net Present Values (NPVs). Our primary objective was to identify optimal well spacing (w_spacing) and per-interval injection rate (Qinj) for profitable geothermal fields under specific uncertainties, utilizing a binning-based optimization approach. This involved dividing the data into 36 bins based on w_spacing and Qinj ranges and calculating NPVs' 10th, 50th, and 90th percentile scores in each bin. Our findings indicate that the most profitable scenarios are achieved with w_spacing between 190 to 747 m and Qinj between 0.01 to 0.3 m^3/s, particularly in the 509 to 588 m range for w_spacing, with potential profits up to 35 million USD.

4. MCMC was used with NUTS sampling to infer permeability and porosity in a geothermal reservoir, employing a surrogate CNN model trained on data from a PDE-based model. Our findings revealed that the CNN surrogate effectively replicates PDE-based results for thermal and advection processes and can estimate unknown parameters in well-informed layers. However, in areas with no significant data, permeability and porosity inference proved unreliable due to the ill-posed nature of the inverse problem. The study highlights that, while CNN surrogates mirror PDE model limitations, they offer computational time savings by replacing the need for repeated PDE simulations, especially in areas with minimal tracer movement, allowing for efficient parameter space exploration and faster parameter sampling.

References

1. Vesselinov, V. V. *et al.* Discovering hidden geothermal signatures using non-negative matrix factorization with customized k-means clustering. *Geothermics* 106, 102576 (2022).

2. Mudunuru, M. K., Vesselinov, V. V. & Ahmmed, B. GEOTHERMALCLOUD: Machine learning for geothermal resource exploration. *JMLMC* 3, (2022).

3. Frash, L. P. Geothermal Design Tool (GeoDT). in *Proceedings of the 46^\mathrmth Workshop on Geothermal Reservoir Engineering Stanford University, Stanford, February 15* vol. 17 (2021).

4. Frash, L. P. Optimized Enhanced Geothermal Development Strategies with GeoDT and Fracture Caging. in *Proceedings of 47th Workshop on Geothermal Reservoir Engineering* vol. 47 (Stanford University, Stanford, California, 2022).

5. Ahmmed, B. & Frash, L. A FORGE Datathon Case Study to Optimize Well Spacing and Flow Rate for Power Generation. in *48th Stanford Geothermal Workshop* (Stanford, CA, 2023).

6. Mudunuru, M. K., Ahmmed, B. & Frash, L. P. Deep Learning for Modeling Enhanced Geothermal Systems. in *PROCEEDINGS of 48th Workshop on Geothermal Reservoir Engineering* (Stanford University, Stanford, California, 2023).

7. Singh, A., Thakur, N. & Sharma, A. A review of supervised machine learning algorithms. in *2016 3rd International Conference on Computing for Sustainable Global Development (INDIACom)* 1310–1315 (2016).

8. Sharma, P., Austin, D. & Liu, H. Attacks on Machine Learning: Adversarial Examples in Connected and Autonomous Vehicles. in *2019 IEEE International Symposium on Technologies for Homeland Security (HST)* 1–7 (2019). doi:10.1109/HST47167.2019.9032989.

9. Feldman, D., Margolis, R., Denholm, P. & Stekli, J. *Exploring the Potential Competitiveness of Utility-Scale Photovoltaics plus Batteries with Concentrating Solar Power, 2015–2030*. (2016).

10. Gu, J. *et al.* Recent advances in convolutional neural networks. *Pattern Recognition* 77, 354–377 (2018).

11. Sherstinsky, A. Fundamentals of Recurrent Neural Network (RNN) and Long Short-Term Memory (LSTM) network. *Physica D: Nonlinear Phenomena* 404, 132306 (2020).

12. Breiman, L. Random Forests. *Machine Learning* 45, 5–32 (2001).

13. Lagaris, I. E., Likas, A. & Fotiadis, D. I. Artificial neural networks for solving ordinary and partial differential equations. *IEEE transactions on neural networks* 9, 987–1000 (1998).

14. Raissi, M., Perdikaris, P. & Karniadakis, G. E. Physics-informed neural networks: A deep learning framework for solving forward and inverse problems involving nonlinear partial differential equations. *Journal of Computational Physics* 378, 686–707 (2019).

15. Vesselinov, V. V., Middleton, R. S. & Talsma, C. *COVID-19: Spatiotemporal Social Data Analytics and Machine Learning for Pandemic Exploration and Forecasting* (2021).

16. Alexandrov, B. S. & Vesselinov, V. V. Blind source separation for groundwater pressure analysis based on nonnegative matrix factorization. *Water Resources Research* 50, 7332–7347 (2014).

17. Lee, D. D. & Seung, H. S. Learning the parts of objects by non-negative matrix factorization. *Nature* 401, 788–791 (1999).

18. Wold, S., Esbensen, K. & Geladi, P. Principal component analysis. *Chemometrics and Intelligent Laboratory Systems* 2, 37–52 (1987).

19. Hyvärinen, A. & Oja, E. Independent component analysis: algorithms and applications. *Neural Networks* 13, 411–430 (2000).

20. De Lathauwer, L., De Moor, B. & Vandewalle, J. A Multilinear Singular Value Decomposition. *SIAM J. Matrix Anal. Appl.* 21, 1253–1278 (2000).

21. Cichocki, A., Zdunek, R. & Amari, S. Nonnegative Matrix and Tensor Factorization [Lecture Notes]. *IEEE Signal Processing Magazine* 25, 142–145 (2008).

22. Shi, J. Q., Murray-Smith, R. & Titterington, D. M. Hierarchical Gaussian process mixtures for regression. *Stat Comput* 15, 31–41 (2005).

23. Los Alamos National Laboratory. SmartTensors: Artificial Intelligence and Machine Learning using Unsupervised, Supervised, and Physics-Informed Methods. https://tensors.lanl.gov/. (2019).

24. Böttcher, A. & Wenzel, D. The Frobenius norm and the commutator. *Linear Algebra and its Applications* 429, 1864–1885 (2008).

25. Vesselinov, V. V., Mudunuru, M. K., Karra, S., O'Malley, D. & Alexandrov, B. S. Unsupervised machine learning based on non-negative tensor factorization for analyzing reactive-mixing. *Journal of Computational Physics* 395, 85–104 (2019).

26. Lu, G. Y. & Wong, D. W. An adaptive inverse-distance weighting spatial interpolation technique. *Computers & Geosciences* 34, 1044–1055 (2008).

27. Burrough, P. A., McDonnell, R. A. & Lloyd, C. D. *Principles of Geographical Information Systems*. (OUP Oxford, 2015).

28. Cumming, W. & Mackie, R. 3D MT resistivity imaging for geothermal resource assessment and environmental mitigation at the glass mountain KGRA, California. *GRC Transactions* 31, 331–334 (2007).

29. Coppo, N. *et al.* 3-D magnetotelluric investigations for geothermal exploration in Martinique (Lesser Antilles). Characteristic deep resistivity structures, and shallow resistivity distribution matching heliborne TEM results. *arXiv preprint arXiv:1501.06541* (2015).

30. Johnston, J. M., Pellerin, L. & Hohmann, G. W. Evaluation of electromagnetic methods for geothermal reservoir detection. *Transactions- Geothermal Resources Council* (1992).

31. Muñoz, G. Exploring for Geothermal Resources with Electromagnetic Methods. *Surv Geophys* 35, 101–122 (2014).

32. Caldwell, T. G., Bibby, H. M. & Brown, C. The magnetotelluric phase tensor. *Geophysical Journal International* 158, 457–469 (2004).

33. Grimm, R. *et al.* A magnetotelluric instrument for probing the interiors of Europa and other worlds. *Advances in Space Research* 68, 2022–2037 (2021).

34. Burns, E. R., Ingebritsen, S. E., Manga, M. & Williams, C. F. Evaluating geothermal and hydrogeologic controls on regional groundwater temperature distribution. *Water Resources Research* 52, 1328–1344 (2015).

35. Vesselinov, V., Ahmmed, B., Frash, L. & Mudunuru, M. K. GeoThermalCloud: Machine Learning for Discovery, Exploration, and Development of Hidden Geothermal Resources. in *47th SGW* (Stanford University, Stanford, California, 2022).

36. Ahmmed, B. & Vesselinov, V. V. Machine learning and shallow groundwater chemistry to identify geothermal prospects in the Great Basin, USA. *Renewable Energy* 197, 1034–1048 (2022).

37. Siler, D. L., Pepin, J. D., Vesselinov, V. V., Mudunuru, M. K. & Ahmmed, B. Machine learning to identify geologic factors associated with production in geothermal fields: a case-study using 3D geologic data, Brady geothermal field, Nevada. *Geothermal Energy* 9, 17 (2021).

38. Ahmmed, B., Vesselinov, V. V., Rau, E., Mudunuru, M. & Karra, S. *Machine Learning and a Process Model to Better Characterize Hidden Geothermal Resources*. (2022).

39. Bennett, C. R. & Nash, G. D. *The Convergence of Heat, Groundwater & Fracture Permeability: Innovative Play Fairway Modelling Applied to the Tularosa Basin*. (2017).

40. Ahmmed, B. & Vesselinov, V. V. *Exploration of Groundwater and Geothermal Characteristics of Tohatchi Hot Springs Aquifer at Local and Regional Scales*. (2022).

41. Ahmmed, B., Lautze, N., Vesselinov, V. V., Dores, D. & Mudunuru, M. K. *Unsupervised Machine Learning to Extract Dominant Geothermal Attributes in Hawaii Island Play Fairway Data*. (Geothermal Resources Council, Online, 2020).

42. Ahmmed, B. & Vesselinov, V. V. Prospectivity Analyses of the Utah FORGE Site using Unsupervised Machine Learning. in *Geothermal Rising, San Diego, CA* (2021).

43. Pedregosa, F. *et al.* Scikit-learn: Machine Learning in Python. *Journal of Machine Learning Research* 12, 2825–2830 (2011).

44. Lichtner, P. C. *et al. PFLOTRAN User Manual: A Massively Parallel Reactive Flow and Transport Model for Describing Surface and Subsurface Processes*. https://www.osti.gov/biblio/1168703 (2015) doi:10.2172/1168703.

45. Christopher Frey, H. & Patil, S. R. Identification and Review of Sensitivity Analysis Methods. *Risk Analysis* 22, 553–578 (2002).

46. Saltelli, A. Sensitivity Analysis for Importance Assessment. *Risk Analysis* 22, 579–590 (2002).

47. Finsterle, S. Practical notes on local data-worth analysis. *Water Resources Research* 51, 9904–9924 (2015).

48. U.S. Energy Information Administration. *December 2021 Monthly Energy Review (Section 1)*. (2021).

49. Hamm, S. G. *et al.* Geothermal Energy R&D: An Overview of the U.S. Department of Energy's Geothermal Technologies Office. *Journal of Energy Resources Technology* 143, (2021).

50. Tester, J. W., Beckers, K. F., Hawkins, A. J. & Lukawski, M. Z. The evolving role of geothermal energy for decarbonizing the United States. *Energy & Environmental Science* 14, 6211–6241 (2021).

51. Barbier, E. Geothermal energy technology and current status: an overview. *Renewable and sustainable energy reviews* 6, 3–65 (2002).

52. Jolie, E. *et al.* Geological controls on geothermal resources for power generation. *Nature Reviews Earth & Environment* 2, 324–339 (2021).

53. Blackwell, D. D., Negraru, P. T. & Richards, M. C. Assessment of the enhanced geothermal system resource base of the United States. *Natural Resources Research* 15, 283–308 (2006).

54. Iliev, F. L., Stanev, V. G., Vesselinov, V. V. & Alexandrov, S., B. Nonnegative matrix factorization for identification of unknown number of sources emitting delayed signals. *PloS one* 13, e0193974 (2018).

55. Arnason, K., Karlsdottir, R., Eysteinsson, H., Flóvenz, Ó. & Gudlaugsson, S. T. The resistivity structure of high-temperature geothermal systems in Iceland. in *Proceedings of the World Geothermal Congress 2000, Kyushu-Tohoku, Japan* 923–928 (2000).

56. Seager, W. R. & Morgan, P. Rio Grande rift in southern New Mexico, west Texas, and northern Chihuahua. *Rio Grande rift: Tectonics and magmatism* 14, 87–106 (1979).

57. Sinno, Y. A., Daggett, P. H., Keller, G. R., Morgan, P. & Harder, S. H. Crustal structure of the southern Rio Grande rift determined from seismic refraction profiling. *Journal of Geophysical Research: Solid Earth* 91, 6143–6156 (1986).

58. Finger, J. T. & Jacobson, R. D. *Fort Bliss Exploratory Slimholes: Drilling and Testing*. (1997).

59. Ussher, G., Harvey, C., Johnstone, R. & Anderson, E. Understanding the resistivities observed in geothermal systems. in *proceedings world geothermal congress* 1915–1920 (Kyushu Japan, 2000).

60. Barker, B. *et al.* Exploration Drilling and Technology Demonstration At Fort Bliss. in *Thirty-Ninth Workshop on Geothermal Reservoir Engineering Stanford University* (2014).

61. O'Donnell Jr, T. M., Miller, K. C. & Witcher, J. C. A seismic and gravity study of the McGregor geothermal system, southern New Mexico. *Geophysics* 66, 1002–1014 (2001).

62. Broadhead, R. F. Petroleum geology of the McGregor Range, Otero County, New Mexico: New Mexico Geological Society. in *53rd Field Conference, Guidebook* 331–338 (2002).

63. Rukundo, O. & Cao, H. Nearest neighbor value interpolation. *arXiv preprint arXiv:1211.1768* (2012).

64. Smith, W. H. F. & Wessel, P. Gridding with continuous curvature splines in tension. *Geophysics* 55, 293–305 (1990).

65. Krige, D. G. A statistical approach to some basic mine valuation problems on the Witwatersrand. *Journal of the Southern African Institute of Mining and Metallurgy* 52, 119–139 (1951).

66. Ahmmed, B., Karra, S., Vesselinov, V. V. & Mudunuru, M. K. Machine learning to discover mineral trapping signatures due to CO2 injection. *International Journal of Greenhouse Gas Control* 109, 103382 (2021).

67. James, E. D., Hoang, V. T. & Epperson, I. J. *Structure, Permeability and Production Characteristics of the Heber, California Geothermal Field*. (1987).

68. Cherkose, B. A. & Mizunaga, H. Resistivity imaging of Aluto-Langano geothermal field using 3-D magnetotelluric inversion. *Journal of African Earth Sciences* 139, 307–318 (2018).

69. Henry, C. D. A preliminary assessment of the geologic setting, hydrology, and geochemistry of the Hueco Tanks Geothermal Area, Texas and New Mexico. *Virtual Landscapes of Texas* (1981).

70. Augustine, C. Analysis of sedimentary geothermal systems using an analytical reservoir model. *Geothermal Resources Council Transactions* 38, 641–647 (2014).

71. Passey, Q. R. *et al. Petrophysical Evaluation of Hydrocarbon Pore-Thickness in Thinly Bedded Clastic Reservoirs: AAPG Archie Series, No. 1*. (AAPG, 2006).

72. Nathenson, M. & Guffanti, M. Geothermal gradients in the conterminous United States. *Journal of Geophysical Research: Solid Earth* 93, 6437–6450 (1988).

73. Di Sipio, E. *et al.* Rock Thermal Conductivity as Key Parameter for Geothermal Numerical Models. *Energy Procedia* 40, 87–94 (2013).

74. Huttrer, G. W. Geothermal power generation in the world 2015-2020 update report. in *World Geothermal Congress; International Geothermal Association: Reykjavik, Iceland* (2020).

75. Dobson, P. F. A review of exploration methods for discovering hidden geothermal systems. *Geothermal Resources Council Transactions* 695–706 (2016).

76. Tester, J. W. *The Future of Geothermal Energy, Impact of Enhanced Geothermal System (EGS) on the United State in the 21st Century: An Assessment by an MIT-Led Interdisciplinary Panel*. (2007).

77. Faulds, J. E. & Hinz, N. H. Favorable tectonic and structural settings of geothermal systems in the Great Basin region, western USA: Proxies for discovering blind geothermal systems. in *Proceedings of the World Geothermal Congress* vol. 6 (2015).

78. Faulds, J. E. *et al.* Integrated geologic and geophysical approach for establishing geothermal play fairways and discovering blind geothermal systems in the Great Basin region, western USA: A progress report. *GRC Transactions* 39, (2015).

79. Faulds, J. E. *et al.* Discovery of a Blind Geothermal System in Southern Gabbs Valley, Western Nevada, through Application of the Play Fairway Analysis at Multiple Scales. *GRC Transactions* 42, (2018).

80. Faulds, J. E. *et al.* Vectoring into Potential Blind Geothermal Systems in the Granite Springs Valley Area, Western Nevada: Application of the Play Fairway Analysis at Multiple Scales. *PROCEEDINGS, 44th Workshop on Geothermal Reservoir Engineering, Stanford University* (2019).

81. Faulds, J. E., Hinz, N., Coolbaugh, M., Shevenell, L. & Siler, D. The Nevada Play Fairway Project — Phase II: Initial Search for New Viable Geothermal Systems in the Great Basin Region, Western USA. *GRC Transactions* 40, (2016).

82. Siler, D. L. *et al.* Three-dimensional geologic mapping to assess geothermal potential: examples from Nevada and Oregon. *Geothermal Energy* 7, 2 (2019).

83. Stone, W. J. & McLin, S. *Hydrologic Tests at Characterization Wells R-9i, R-13, R-19, R-22, and R-31*. https://www.osti.gov/biblio/884954 (2003) doi:10.2172/884954.

84. Williams, C. F., Reed, M. J., Mariner, R. H., DeAngelo, J. & Galanis, S. P. *Assessment of Moderate-and High-Temperature Geothermal Resources of the United States*. (2008).

85. Williams, C. F., Reed, M. J., Mariner, R. H., DeAngelo, J. & Galanis, S. P. *Assessment of Moderate-and High-Temperature Geothermal Resources of the United States, Institution = Geological Survey (US)*. (2008).

86. Nash, G. D. & Bennett, C. R. Adaptation of a petroleum exploration tool to geothermal exploration: Preliminary play fairway model of Tularosa Basin. *New Mexico, and Texas: Geothermal Resources Council Transactions* 39, 743–749 (2015).

87. Kratt, C., Sladek, C. & Coolbaugh, M. Boom and bust with the latest 2 m temperature surveys: Dead Horse Wells, Hawthorne Army Depot, Terraced Hills and other areas in Nevada. *Geothermal Resources Council Transactions* 34, 567–574 (2010).

88. Biehler, S. Gravity studies in the Imperial Valley. *Cooperative Geological-Geophysical-Geochemical Investigations of Geothermal Resources in the Imperial Valley of California: Riverside, California, University of California–Riverside Education Research Service* 29–41 (1971).

89. Olasolo, P., Juárez, M. C., Morales, M. P., D´Amico, S. & Liarte, I. A. Enhanced geothermal systems (EGS): A review. *Renewable and Sustainable Energy Reviews* 56, 133–144 (2016).

90. PIVOT. PIVOT Geothermal Datathon. https://www.spe.org/datasets/2022_PIVOT_Geothermal_Datathon (2022).

91. Moore, J. *et al.* The Utah Frontier Observatory for Research in Geothermal Energy (FORGE): A Laboratory for Characterizing, Creating and Sustaining Enhanced Geothermal Systems. in *World Geothermal Congress* (Reykjavik, Iceland, 2021).

92. Frash, L. P. *et al.* A Proposal for Profitable Enhanced Geothermal Systems in Hot Dry Rock. in *48th Stanford Geothermal Workshop* (Stanford, CA, 2023).

93. Pandey, S. N., Vishal, V. & Chaudhuri, A. Geothermal reservoir modeling in a coupled thermo-hydro-mechanical-chemical approach: A review. *Earth-Science Reviews* 185, 1157–1169 (2018).

94. Kristensen, L. *et al.* Pre-drilling assessments of average porosity and permeability in the geothermal reservoirs of the Danish area. *Geothermal Energy* 4, 1–27 (2016).

95. Weibel, R. *et al.* Predicting permeability of low-enthalpy geothermal reservoirs: A case study from the Upper Triassic–Lower Jurassic Gassum Formation, Norwegian–Danish Basin. *Geothermics* 65, 135–157 (2017).

96. Bauer, J. F., Krumbholz, M., Meier, S. & Tanner, D. C. Predictability of properties of a fractured geothermal

reservoir: the opportunities and limitations of an outcrop analogue study. *Geothermal Energy* 5, 1–27 (2017).

97. Jafari, A. & Babadagli, T. Effective fracture network permeability of geothermal reservoirs. *Geothermics* 40, 25–38 (2011).

98. Catinat, M., Fleury, M., Brigaud, B., Antics, M. & Ungemach, P. Estimating permeability in a limestone geothermal reservoir from NMR laboratory experiments. *Geothermics* 111, 102707 (2023).

99. Jiang, Z., Zhang, S., Turnadge, C. & Xu, T. Combining autoencoder neural network and Bayesian inversion to estimate heterogeneous permeability distributions in enhanced geothermal reservoir: Model development and verification. *Geothermics* 97, 102262 (2021).

100. Suzuki, A., Fukui, K., Onodera, S., Ishizaki, J. & Hashida, T. Data-Driven Geothermal Reservoir Modeling: Estimating Permeability Distributions by Machine Learning. *Geosciences* 12, 130 (2022).

101. Pepin, J. *et al.* Deep fluid circulation within crystalline basement rocks and the role of hydrologic windows in the formation of the Truth or Consequences, New Mexico low-temperature geothermal system. *Geofluids* 15, 139–160 (2015).

102. Mudunuru, M. K. *et al.* Site-Scale and Regional-Scale Modeling for Geothermal Resource Analysis and Exploration. in *45th Annu. Stanf. Geotherm. Workshop* (Stanford, CA, 2020).

103. Johnson, P. J., Stauffer, P. H., Omagbon, J. & Moore, C. R. Implications of rootless geothermal models: Missing processes, parameter compensation, and imposter convection. *Geothermics* 102, 102391 (2022).

104. Bielicki, J. *et al. Hydrogeolgic Windows: Regional Signature Detection for Blind and Traditional Geothermal Play Fairways, Final Reports, Los Alamos National Laboratory*. (2015).

105. Mo, S., Zabaras, N., Shi, X. & Wu, J. Deep autoregressive neural networks for high-dimensional inverse problems in groundwater contaminant source identification. *Water Resources Research* 55, 3856–3881 (2019).

106. Zhou, Z. & Tartakovsky, D. M. Markov chain Monte Carlo with neural network surrogates: Application to contaminant source identification. *Stochastic Environmental Research and Risk Assessment* 35, 639–651 (2021).

107. Huang, G., Liu, Z., Van Der Maaten, L. & Weinberger, K. Q. Densely connected convolutional networks. in *Proceedings of the IEEE conference on computer vision and pattern recognition* 4700–4708 (2017).

108. Kingma, D. P. & Ba, J. Adam: A method for stochastic optimization. *arXiv preprint arXiv:1412.6980* (2014).

109. Hoffman, M. D. & Gelman, A. The No-U-Turn sampler: adaptively setting path lengths in Hamiltonian Monte Carlo. *J. Mach. Learn. Res.* 15, 1593–1623 (2014).

110. Neal, R. M. MCMC using Hamiltonian dynamics. *Handbook of Markov chain Monte Carlo* 2, 2 (2011).

111. Ayling, B., Faulds, J. E. & Rivera, A. M. *INGENIOUS - Great Basin Regional Dataset Compilation*. https://gdr.openei.org/submissions/1391 (2022).

112. EERE-GTO, U. USGS and EERE: Collaborating to Strengthen America's Energy and Resource Independence. *Energy.gov* https://www.energy.gov/eere/articles/usgs-and-eere-collaborating-strengthen-americas-energy-and-resource-independence. (2020).

113. Frash, L. P., Carey, J.W., Ahmmed, B., Sweeney, M., Meng, M., Li, W., K C, B., Iyare, U A Proposal for Safe and Profitable Enhanced Geothermal Systems in Hot Dry Rock. In *48th Workshop on Geothermal Reservoir Engineering*, Stanford, CA (2023).

ADDENDUM TO THE FINAL REPORT

DANIEL M. TARTAKOVSKY, STANFORD UNIVERSITY

The Stanford team consisted of Professor Daniel Tartakovsky (Stanford PI) and PhD students Zitong Zhou, Dimitrios Belivanis, and Xiaoyu Yang. Throughout the project, the team interacted closely with its LANL collaborators. The team's effort resulted in publications [1, 2, 3, 4]. Key results and findings are reported below.

1. Machine Learning for Fractured Rock Characterization

The interpretation of hydraulic and tracer experiments involves inverse modeling. The choice of a strategy for the latter depends on the properties of interest, the data considered, the models available to reproduce the data, and the prior information about the studied environment. For canonical fracture configurations between two boreholes, (semi-)analytical and numerical models can be used to the cross-borehole flow-meter experiments mentioned above to evaluate the transmissivity and storativity of the fractures that intersect the boreholes at known depths. Large-scale systems with complex fracture configurations require the use of sophisticated inversion strategies designed for high volumes of data. Most of such studies generate data via hydraulic and/or tracer tomography experiments, and use the inversion to identify the geometric and hydraulic properties of a fracture network. These studies limit the number of fractures in a network in order to work with a tractable number of parameters to invert.

Forward models relating the fracture network properties to chemical or thermal breakthrough curves show that the shape of these curves is impacted by two factors. The first is the degree of heterogeneity of the fracture network and the matrix block size distribution; the second is the fracture density and fractal dimension, with the latter impacting the breakthrough curves when a fracture network is dense and flow is slow. In contrast to strategies inferring geometric and hydraulic properties, the number of statistical parameters in this framework is sufficiently low to be identified via inverse modeling.

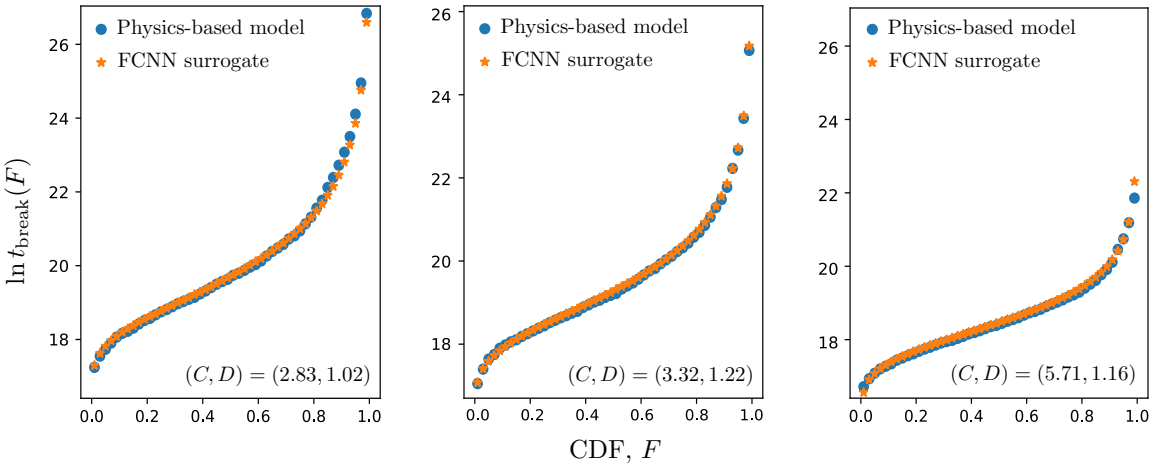

Figure 1. Physics-based and FCNN (fully connected neural network) predictions of iCDFs (inverse cumulative distribution functions) of the particle breakthrough times in discrete fracture networks (DFNs) characterized by different parameter-pairs (C, D) not used for training.

Identification of these parameters rests on ensemble-based computation, which involves repeated solves of a forward model. Two complementary strategies for making the inversion feasible for large, complex problems are i) to reduce the number of forward solves that are necessary for the inversion algorithm to converge, and ii) to reduce the computational cost of an individual forward solve. The former strategy includes the development of accelerated Markov chain samplers, Hamiltonian Monte Carlo sampling, iterative local updating ensemble smoother, ensemble Kalman filters, and learning on

statistical manifolds. The latter strategy aims to replace an expensive forward model with its cheap surrogate/emulator/reduced-order model. Among these techniques, various flavors of deep neural networks (DNNs) have attracted attention, in part, because they remain robust for large numbers of inputs and outputs. Another benefit of DNNs is that their implementation in open-source software is portable to advanced computer architectures, such as graphics processing units and tensor processing units, without significant coding effort from the user.

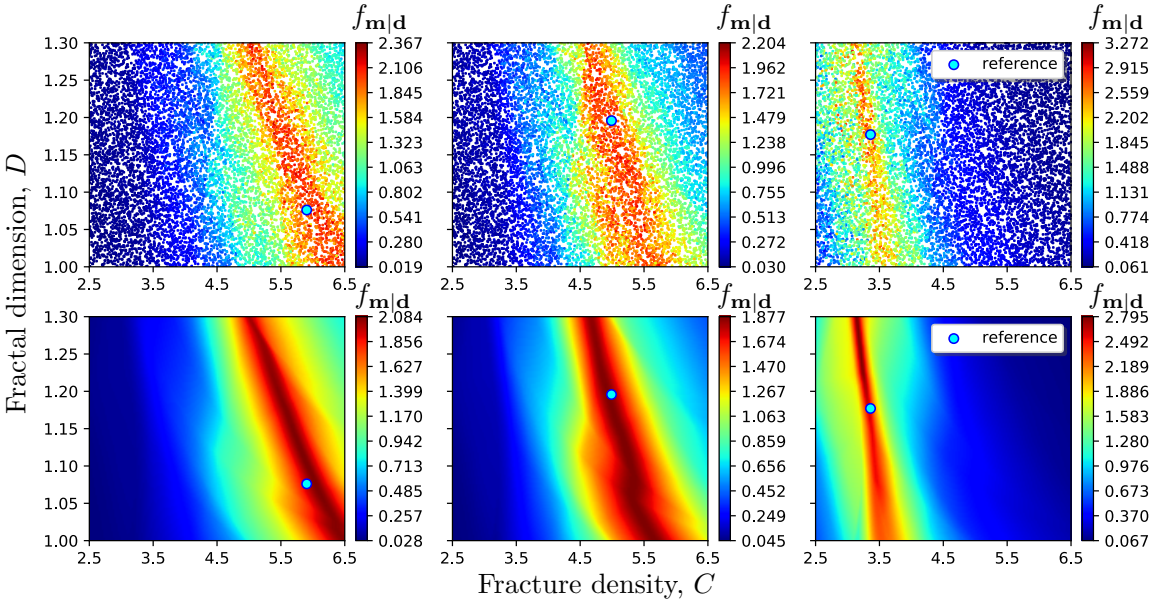

FIGURE 2. Examples of the normalized posterior PDFs of the DFN parameters C and D: $f_{\mathbf{m}|\mathbf{d}}(\tilde{\mathbf{m}};\cdot)$, $\mathbf{m} = (C, D)^\top$, for three experiments defined by the reference parameter values (blue circles). These PDFs are computed via Bayesian assimilation of either 10^4 runs of the physics-based model (top row) or additional 10^7 runs of the FCNN surrogate (bottom row).

We [4] combined these two strategies for ensemble-based computation to develop an inversion method, which makes it possible to infer the statistical properties of a fracture network from cross-borehole thermal experiments (CBTEs). To alleviate the high cost of a forward model of hydro-thermal experiments, we used a meshless, particle-based method to solve the two-dimensional governing equations for fluid flow and heat transfer in discrete fracture networks (DFNs). These solutions, obtained for several realizations of the DFN parameters, were used to train an accurate and robust surrogate based on a fully connected neural network (Fig. 1). The latter's cost is so negligible as to enable us to deploy a fully Bayesian inversion that, unlike ensemble Kalman filter, does not require our quantity of interest to be (approximately) Gaussian. Our numerical experiments showed that our approach is four orders of magnitude faster than the equivalent inversion based on the physics-based model. These synthetic experiments also revealed (Fig. 2) that the CBTE data allow one to obtain accurate estimates of fracture density, while the inference of a DFN's fractal dimension is less robust.

2. AI-Assisted Analysis of Well-Temperature Logs

Downhole measurements are widely used to characterize fractures in geothermal reservoirs, especially to identify the fractures intersected by the borehole. While the inference of a complete subsurface fracture pattern from downhole measurements is challenging due to the limited sampling space of a wellbore, those measurements still provide effective near-wellbore fracture delineation. The latter may be further combined with other information, e.g., chemical data, to obtain a more complete fracture characterization. The basic idea is to generate detectable signals and then identify fractures based on model-derived relations. A prime example of such measurable signals is the downhole temperature measured by either traditional production logging tools or the fiber-optic-based distributed temperature sensing (DTS).

Thanks to their high spatiotemporal resolution, DTS measurements have become one of the most commonly measured signals over the life of a well. The continuous and integrated temperature information reflects dynamic thermal transport between wellbore and reservoir, which is strongly coupled with flow behavior and therefore influenced by the fracture characteristics. Inverse methods, used to infer fracture distribution from wellbore temperature, include stochastic approaches, e.g., Markov chain Monte Carlo and optimization-based techniques such as the Gauss-Newton method and the Levenberg-Marquardt method. The accuracy and robustness of such algorithms depend, in large part, on the adequacy of the forward mapping. Physics-based forward models simplify complex flow and heat-transfer processes in a fractured reservoir, which causes the temperature-fracture mapping to be imperfect and may lead to the inversion failure. Data-driven algorithms (e.g., machine learning or ML) do not require a pre-established perfect forward map, directly learning a mapping relation from data. ML has been used to solve inverse problems in geothermal applications. Unlike physics-based algorithms that process cases one by one, well-trained machine learning algorithms can automatically process a large number of cases at the same time, rendering the solution of inversion problems more efficient and effective.

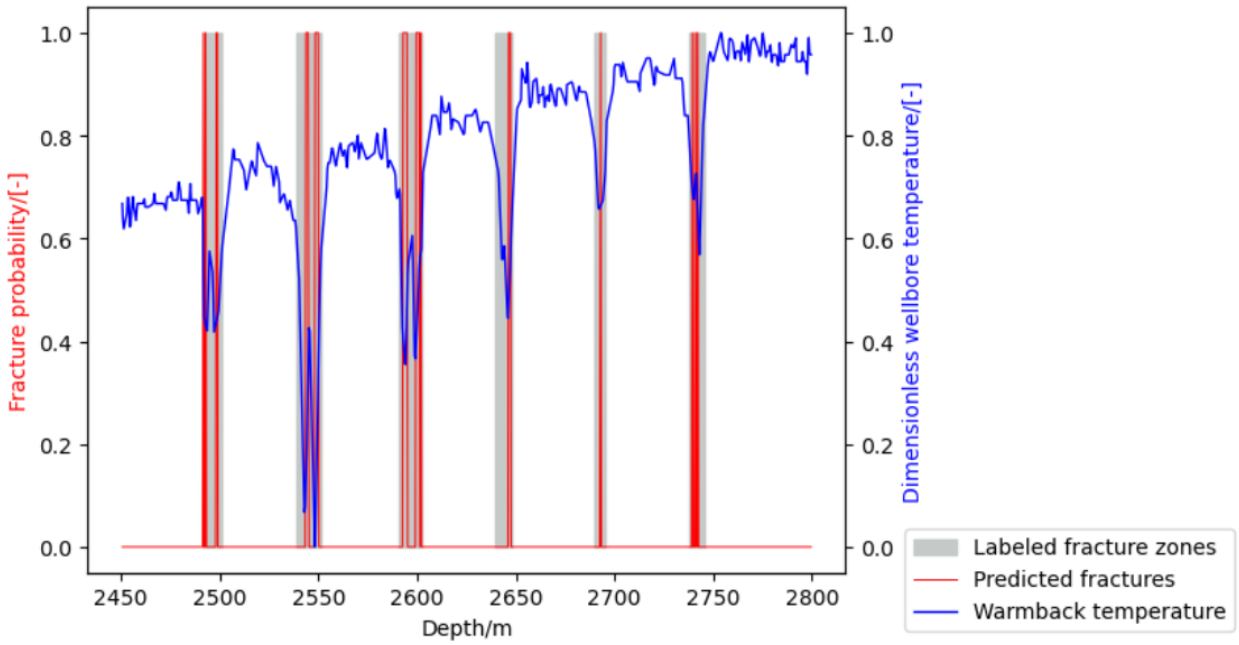

FIGURE 3. Labeled and predicted fracture distributions for a real warmback case.

While wellbore DTS measurements are available in geothermal projects, attempts to use wellbore temperature in ML-based solutions of geothermal inverse problems are scarce. Yet, wellbore temperature data are known to contain rich information about fractures, specifically those intersecting the wellbore. Hence, temperature series are a good data-source to train a ML algorithm for near-wellbore fracture characterization. We [2] used DTS profiles at different stages, i.e., injection, warmback and the static stage to carry out a fracture-distribution inversion facilitated by a ML-based surrogate. This neural-network surrogate, LSTM-FCN, is a fusion of a long short-term memory network (LSTM) and a fully convolutional network (FCN). A unique feature of our approach is its ability to capture simultaneously the long-term dependencies and local characteristics of temperature signals, and to detect multiple fractures in a complex fractured reservoir system (Fig. 3).

We [3] deployed our LSTM-FCN surrogate not only to identify fracture locations intersecting the wellbore but also to quantify the contribution of flow into fractures during injection. By capturing both the long-term dependencies and the local characteristics of the downhole temperature series, the LSTM-FCN model learns the fracture-temperature mapping relation and identifies the fracture flowrate distribution (Fig. 4). A unique feature of our work was to compare the performance of the machine learning method and the particle swarm optimization (PSO) method on field data, and to demonstrate the advantages of machine learning for accurately capturing the fracture-affected abnormal temperature signals. Another unique feature was to evaluate the effectiveness of multistage

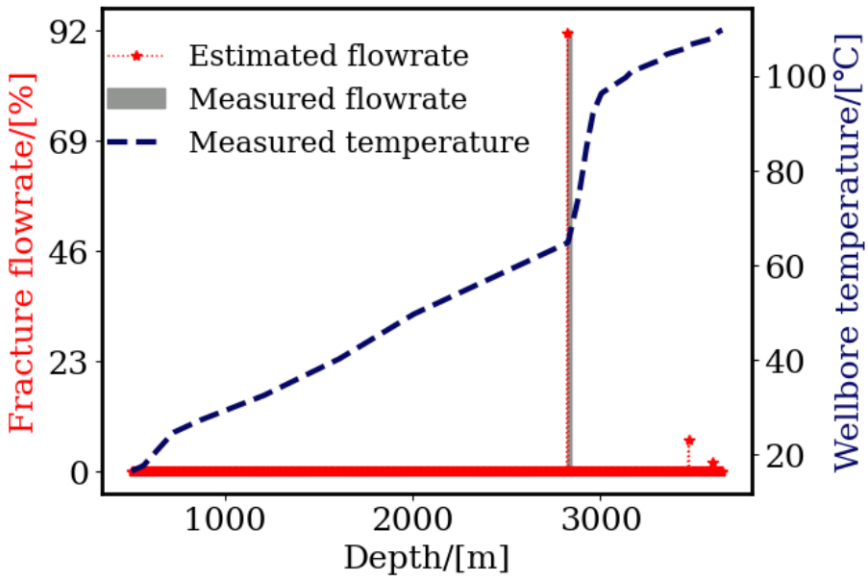

FIGURE 4. The comparison of measured and machine learning predicted fracture flowrate distribution for a real injection case.

temperature information fusion on fracture flowrate quantification by combing injection and warmback temperature as input features of the machine learning models.

REFERENCES

[1] H. S. Viswanathan, J. Ajo-Franklin, J. Birkholzer, J. W. Carey, Y. Guglielmi, J. D. Hyman, S. Karra, L. Pyrak-Nolte, H. Rajaram, G. Srinivasan, and D. M. Tartakovsky. From fluid flow to coupled processes in fractured rock: recent advances and new frontiers. *Reviews of Geophysics*, 60(1):e2021RG000744, 2022.

[2] X. Yang, R. N. Horne, and D. M. Tartakovsky. Fracture characterization via AI-assisted analysis of temperature logs. *Journal of Geophysical Research: Machine Learning and Computation*, 1:e2024JH000263, 2024.

[3] X. Yang, R. N. Horne, and D. M. Tartakovsky. Machine-learned inference of fracture flowrate from temperature logs. *Journal of Machine Learning for Modeling and Computing*, 5(3):31–45, 2024.

[4] Z. Zhou, D. Roubinet, and D. M. Tartakovsky. Thermal experiments for fractured rock characterization: theoretical analysis and inverse modeling. *Water Resources Research*, 57(12):e2021WR030608, 2021.